

# **University of Alberta**

Developing Design Guidelines for Improved Gecko Inspired Dry Adhesive

Performance

by

**Benjamin Simon Bschaden**

A thesis submitted to the Faculty of Graduate Studies and Research  
in partial fulfillment of the requirements for the degree of

Master of Science

Department of Mechanical Engineering

© Benjamin Simon Bschaden  
SPRING 2014  
Edmonton, Alberta

## **ABSTRACT**

This work provides a guideline for gecko inspired dry adhesive design and simulation. Mechanical property testing for several polymers commonly used in gecko adhesives (Kraton G1657 thermoplastic elastomer, ST-1060, and ST-1087 polyurethane elastomers) allowed hyperelastic and viscoelastic material models to be fitted. These parameters were implemented in a finite element simulation of a single adhesive fiber. The simulation was further improved over previously published models by developing a frictional cap interface boundary condition.

The simulation was verified by contrasting the results obtained by testing isolated fibers. Adhesion results from a single fiber tests system developed demonstrated that all materials exhibit the Mullins effect, with significant softening after one elongation. Future designs requiring durability are therefore recommended to have lower aspect ratios, limiting the maximum strain in the fiber. Based on experimental observations, a summary is provided to select appropriate boundary conditions based on the specifications of the adhesive.

## **ACKNOWLEDGMENTS**

I would like to thank my supervisor, Dr. Dan Sameoto for his unprecedented guidance and training from which I have learned so much and without which, my work would not have been possible. I also want to acknowledge Dr. Ted Hubbard from Dalhousie University for inspiring me to do graduate work in microfabrication, ultimately leading me to the life I have now.

Thank you also to the Staff at the University of Alberta Nanofab for their advice, assistance, and training. I would also like to acknowledge contributions from my lab mates with a special thanks to Brendan Ferguson.

Finally, I would like to thank my family for their love and for always being there for me, my friends for support during difficult times and for making this experience so enjoyable, and to my girlfriend Anita Bianchini for her limitless support, motivation, and love. My successes would not have been possible without all of your help.

## TABLE OF CONTENTS

1	INTRODUCTION.....	1
1.1	Gecko Inspired Dry Adhesives Materials .....	1
1.2	Gecko Adhesion: Advantages and Applications.....	6
1.3	Polymers in Dry Adhesive Research.....	7
1.4	Dry Adhesive Simulations .....	8
1.5	Single Fiber Adhesion Testing.....	10
1.6	Motivation and Outline of Project.....	13
2	ELASTOMER MATERIAL CHARACTERIZATION AND MODELING	16
2.1	Introduction .....	16
2.2	Instron Uniaxial Test Method .....	17
2.3	Test Sample Casting.....	18
2.3.1	Thermoplastic Test Samples .....	19
2.3.2	Thermosets .....	24
2.4	Hyperelasticity .....	25
2.4.1	Mooney Rivlin Model.....	25
2.4.2	Uniaxial Elongation Tests.....	31
2.4.3	Model Fit.....	34
2.5	Plasticity.....	40
2.6	Viscoelasticity .....	50
2.6.1	Background .....	50
2.6.2	Results.....	55
3	FIBER SIMULATION .....	58

3.1	Introduction .....	58
3.2	Model Setup .....	60
3.3	Mesh Convergence Study.....	63
3.4	Fixed BC .....	66
3.5	Roller BC.....	67
3.6	Frictional BC .....	68
3.7	Viscoelastic .....	74
4	SINGLE FIBER FABRICATION.....	76
4.1	Introduction .....	76
4.2	Mask Design.....	77
4.3	Clean-room Master Mold Fabrication.....	81
4.3.1	Substrates Used.....	82
4.3.2	Spin Coating.....	82
4.3.3	UV Photomask Exposure.....	83
4.3.4	Deep UV Exposure .....	85
4.3.5	Development .....	86
4.3.6	Fiber Proximity Effect Results.....	87
4.3.7	Mold Fabrication Results .....	89
4.4	Replication Molding Procedures .....	91
4.4.1	Negative Mold Fabrication .....	93
4.4.2	Thermoset Fiber replication .....	94
4.4.3	Thermoplastic Fiber replication .....	95
5	ADHESION TESTING .....	100
5.1	Introduction .....	100

5.2	Single Fiber Test System.....	101
5.2.1	Linear Stage Mount Bracket Design.....	102
5.2.2	Microscope and Camera Assembly .....	103
5.2.3	Adhesion Surface .....	104
5.2.4	Load Cell-Fiber-Probe Assembly .....	107
5.2.5	Single Fiber Test System Data Analysis.....	109
5.2.6	Operating the Single Fiber Test System .....	112
5.3	Adhesion Results.....	113
5.3.1	Normal Loading.....	116
5.3.2	Relaxation Tests.....	125
5.3.3	Shear .....	127
5.3.4	Frictional Interface Analysis.....	130
6	CONCLUSIONS .....	141
6.1	Summary .....	141
6.2	Future Work .....	144
7	BIBLIOGRAPHY .....	147
8	APPENDICES .....	157
8.1	Appendix A: Electron Beam Lithography Fabrication .....	157
8.2	Appendix B: Matlab Code used for Non-Linear Data Fits .....	163
8.3	Appendix C: COMSOL Simulation Reports.....	169
8.4	Appendix D: Single Fiber Test Mount Bracket Drawing Package .....	190

## LIST OF TABLES

Table 2-1: Materials tested, properties from data sheets [58-60] .....	19
Table 2-2: Mooney Rivlin fit parameters (bulk modulus, $k = 1e8$ Pa for all cases), Kraton G1657 and ST-1087 use a 5 term Mooney Rivlin fit while ST-1060 fits well with a 2 term model. Negative values required for fit but may cause instabilities for some loading conditions. ....	40
Table 2-3: Summary of Kraton G1657, ST-1060, and ST-1060 material properties tested for viscoelastic models. ....	57
Table 4-1: Fiber size list for single fiber photomask. ....	79
Table 4-2: Summary of SU-8 spin recipes for substrates prepared. ....	83
Table 4-3: Deep UV exposure recipe for PMMA substrates SFM1, SFM2, and SFM3. Note, exposure areas 1, 2 and 3 in Figure 4.1 illustrate areas of the mold with different exposure doses as listed below.....	85
Table 4-4: PMMA exposure depth measured with stylus profilometer.....	87
Table 4-5: Minimum surviving feature size on PMMA master molds, determined by optical microscopy. Note, feature size listed represents top cap diameter; actual neck dimensions where failure occurs was much smaller. ....	91
Table 4-6: Negative mold material property: comparison between TC-5030 and Sylgard 184 [86,87] .....	93
Table 4-7: Qualitative measure of replication success for thermoplastic materials tested (properties taken from data sheets [58,88-94]).....	96
Table 5-1: Contact surface measured roughness determined with a Zygo optical profilometer with $\sim 15$ $\mu\text{m}$ line averages. ....	106
Table 5-2: Modified Mooney Rivlin constants used to account for polymer chain alignment and biaxial loading. Negative values required for fit but may cause instabilities for some loading conditions. ....	118
Table 5-3: Single fiber adhesion results, fiber array peel strength, and fitted friction factor (Kraton G1657 fiber sheared 150 $\mu\text{m}$ , ST-1060 sheared 90 $\mu\text{m}$ for these measurements). ....	137

## LIST OF FIGURES

Figure 1.1: SEM images of hierarchical adhesion mechanism: (A) one setae branch, (B) Array of nanoscale spatula tips on the end of the setae branch, (C) tokay gecko climbing a glass surface, (D) Array of setae, (E) Toe peeling creating a controlled detachment. Printed from [6] with permission. ....	3
Figure 1.2: Examples of dry adhesive pillar designs in literature: a) high aspect ratio angled microfibers adhesive arrays. Reprinted with permission from [11] Copyright 2007 American Chemical Society, b) hierarchical fibers with overhanging features on both micro and nano length scales. Reprinted with permission from [12] Copyright 2009 American Chemical Society, c) low aspect ratio pillars with mushroom shaped top cap. Reprinted from [13] Copyright 2008 with permission from Elsevier, d) close up of individual fiber with large cap undercut. This figure was published in [14] Copyright 2013 Elsevier Masson SAS. All rights reserved. ....	5
Figure 1.3: Illustration of hemispherical adhesion testing (image shows angled posts but straight fibers will have the same effect). Reprinted with permission from [11] Copyright 2007 American Chemical Society. ....	12
Figure 2.1: Instron testing system and computer controlled software setup.....	18
Figure 2.2: Thermoplastic test sample preparation. ....	19
Figure 2.3: Melting thermoplastic pellets to form Instron bulk material test samples.....	20
Figure 2.4: Inconsistent material properties of Kraton G1657 (hot plate method). ....	21
Figure 2.5: Illustration of macro scale thermoplastic pellet melting and the non-uniform (not optically observable) structure compared with the ideal homogenous melted polymer sample. ....	22
Figure 2.6: Image of Kraton G1657 sticks for glue gun processing. ....	23
Figure 2.7: Kraton sample preparation: a) glue gun extrusion of Kraton on glass slide, b) cover Kraton with plastic sheet (cyclic olefin copolymer (COC) [61]), c)	

place metal sheet over sample and add weight for 10 seconds, d) cool Kraton sample enclosed in glass/COC sheet, e) final sample after cutting with scalpel. . 24

Figure 2.8: Polyurethane test sample casting procedure: a) vacuum degas prepolymer in container, b) pour prepolymer on Teflon sheet between the Teflon spacer, c) vacuum degas on Teflon mold, d) cover with Teflon sheet and metal plate, secure with a magnet on each side and paper clips along the edges. Cure for 24 hours, e) bake polymer sheets at 80°C for 16 hours..... 25

Figure 2.9: Experimental stress-strain diagram; average of 4 tests for 3 materials ..... 32

Figure 2.10: Experimental stress-strain diagrams individual trials and averages. Kraton G1657 and ST-1087 fit with MR-5 term (equation 21) and ST-1060 fit with MR-2 term (equation 18). The jagged line at higher elongations was the result of small slippage within the clamps..... 34

Figure 2.11: Mooney-Rivlin fit curves compared to experimental data. .... 36

Figure 2.12: FEA boundary conditions simulating uniaxial elongation Instron test. .... 37

Figure 2.13: FEA force vs. elongation results for ST-1060 rectangular test sample with varying bulk modulus k. Increasing k values show convergence to a solution, which also corresponds to the experimental results found. .... 38

Figure 2.14: Stress-strain behavior for test materials and Mooney Rivlin parameter verification using COMSOL..... 39

Figure 2.15: Instron loading diagram for plasticity testing, repeated for 10 cycles, followed by a full elongation until fracture. .... 40

Figure 2.16: Cycled elongation test to 100% and 150% strain showing hysteresis and plastic deformation; showing cycles 1, 2, and 10. .... 44

Figure 2.17: Maximum tensile stress at 100% and 150% elongation vs. cycle number. .... 45

Figure 2.18: Evidence of Mullins effect showing pristine stress-strain curve overlaid with material data from cycled polymer (vertical lines at 1 and 1.5 strain

for clarity.....	47
Figure 2.19: Instron loading diagram for yield test, performed manually with each cycle increasing elongation by 2 mm increments until 100% elongation. ....	48
Figure 2.20: Percent yield vs. percent resulting elongation in each tested material. Each curve represents average and standard deviation of three trials. ....	49
Figure 2.21: Three-branch Maxwell model used to simulate linear viscoelasticity of the polymers. Stiffness modeled by $k$ and damping with $c$ ( $k_e$ represents steady state material stiffness). ....	51
Figure 2.22: Single branch of the Maxwell model. ....	51
Figure 2.23: Relaxation tests at 100% on the left and 150% elongation on the right with 3 time constant curve fit for the three materials examined.....	56
Figure 3.1: 24 $\mu\text{m}$ diameter ST-1060 fibers attached to silicon die in SEM showing cap shrinkage during elongation (Fibers fabricated and SEM image taken by Brendan Ferguson). Reprinted with permission from [19]. Copyright (2013) Ferguson.....	59
Figure 3.2: Solidworks models of four main fibers chosen for simulation. Dimensions determined from scanning electron microscope images of fabricated fibers: a) 100 $\mu\text{m}$ diameter fiber, b) 160 $\mu\text{m}$ diameter fiber, c) 200 $\mu\text{m}$ diameter fiber, d) 120 $\mu\text{m}$ diameter vertical walled post, .....	61
Figure 3.3: FEA boundary conditions and geometry assembly.....	62
Figure 3.4: FEA model mesh convergence study (100 $\mu\text{m}$ diameter Kraton G1657 fiber) with a fixed cap BC comparing solution time with the maximum top cap von Mises stresses. Element sizes ranging from 0.01 $\mu\text{m}$ – 20 $\mu\text{m}$ (shown in logarithmic scale).....	63
Figure 3.5: FEA mesh convergence study (100 $\mu\text{m}$ diameter Kraton G1657 fiber) with a fixed cap BC showing axial reaction forces converging at 0.8 $\mu\text{m}$ element size. Element sizes ranging from 0.01 $\mu\text{m}$ – 20 $\mu\text{m}$ (shown in logarithmic scale). .....	64
Figure 3.6: FEA results (von Mises stresses) for mesh convergence study showing	

drastically different top cap stress distribution for the two extreme mesh sizes (20  $\mu\text{m}$  and 0.01  $\mu\text{m}$ ). Images for 100  $\mu\text{m}$  Kraton G1657 fiber with fixed cap BC. .. 65

Figure 3.7: Fixed BC simulation (100  $\mu\text{m}$  Kraton G1657 fiber). Central cross section (left) shows von Mises stresses (with outline of un-deformed fiber), graph (right) illustrates von Mises and axial stresses of top cap taken from the top surface of the fiber. .... 66

Figure 3.8: Roller BC simulation (100  $\mu\text{m}$  Kraton G1657 fiber). Central cross section (left) shows von Mises stresses (with outline of un-deformed fiber), graph (right) illustrates von Mises and axial stresses of top cap taken from the top surface of the fiber. .... 68

Figure 3.9: Illustration of frictional boundary condition implemented in a COMSOL FEA simulation. .... 70

Figure 3.10: Frictional boundary condition FEA results with straight cylinder fiber showing control of shrinkage with coefficient of friction,  $\mu$ ..... 71

Figure 3.11: Axial force vs. fiber elongation for fixed vs. roller cap boundary conditions FEA simulations (100  $\mu\text{m}$  diameter ST-1060 fiber). .... 72

Figure 3.12: Roller BC cap shrinkage vs. elongation for 100  $\mu\text{m}$  diameter ST-1060 fiber. .... 73

Figure 3.13: Total axial forces of the top cap interface vs. fiber elongation for fixed and roller cap simulations (100  $\mu\text{m}$  diameter ST-1060 fiber). .... 73

Figure 4.1: Photomask design layout illustration: array test section, 4 identical single fiber test sections to be exposed to different DUV doses (represented by different color of shading), and 3x3 fiber proximity test section in label 4 (see Figure 4.3). Each section of single fibers (numbered 1-3 and 5-19) have 3 features spaced 5 mm apart. Note fiber size and spacing not to scale..... 78

Figure 4.2: Photomask exposure proximity effect: a) illustration of top view fiber array spacing, b) SEM image of an example of square shaped neck fiber caused by proximity effect. Reprinted with permission from [19]. Copyright (2013) Ferguson..... 79

Figure 4.3: Fiber proximity effect study section of single fiber mask design. .... 81

Figure 4.4: Optical images of SFM1 master: a) shows circular cross sectional neck with 200  $\mu\text{m}$  spacing for a 200  $\mu\text{m}$  diameter fiber, b) shows a slightly square cross section developing for a 200  $\mu\text{m}$  diameter fiber with 20  $\mu\text{m}$  spacing, c) shows an extremely square shaped neck for 80  $\mu\text{m}$  diameter fiber with 20  $\mu\text{m}$  spacing (a was focused on the fiber cap while b and c are focused on the fiber neck to clarify effect, both image b and c will still show non-circular shape when focused on top cap), d) round cross section of 40  $\mu\text{m}$  spacing. .... 88

Figure 4.5: Optical microscope images (all are 100  $\mu\text{m}$  fibers) on PMMA master molds, a) SFM1, exposure area 1 single fiber showing close to ideal undercut and cap overhang, b) SFM1 exposure area 1 fiber array with 20  $\mu\text{m}$  spacing showing slightly less undercut and a non-circular neck cross section due to proximity effect, c) SFM2, exposure area 1 single fiber showing an extremely narrow neck, resulting in an extremely delicate fiber which would not survive replication molding, d) SFM3, exposure area 4 single fiber showing almost no undercut or cap overhang, resulting in an almost straight cylinder fiber which would give poor adhesion results. .... 90

Figure 4.6: Thermoplastic fiber casting process illustration, a) thermoplastic heated on hotplate with pressure on mold, b) negative mold/thermoplastic was allowed to cool, c) de-mold from silicone rubber then de-mold from glass for final thermoplastic micro structures. Starting with a polymer sample thickest in the center greatly reduces the trapped gasses in the mold and permits excellent reproduction without the need for applied vacuum. .... 92

Figure 4.7: Illustration of polyurethane single fiber test sample preparation. Sample was cut while contained within the mold and rigid silicone sheet to prevent fiber contamination. .... 95

Figure 4.8: Array of square micro posts, cast from Dryflex thermoplastic elastomer showing poor replication fidelity with very rough top surfaces. .... 96

Figure 4.9: gold coated polystyrene close up of a replica of *Agropyron repens*

(grass); a) micro thorns thorn showing nanoscale fidelity b) array of three thorns. .....	97
Figure 4.10: SEM images of Kraton replications of five different fibers, chosen as a wide range of geometric shapes. All fibers were gold coated to allow viewing without charging effects. 100µm, 120 µm cylinder, µm, 160 µm, and 200 µm diameter fibers (description in bold above) were tested in chapter 5. Scale bars represent 20 µm. ....	99
Figure 5.1: Single fiber test system design layout illustration.....	101
Figure 5.2: Solidworks assembly drawing of linear stage mount bracket. ....	102
Figure 5.3: Linear stage mount bracket, final implemented design.....	103
Figure 5.4: Single fiber test system: microscope three axis position control. ....	104
Figure 5.5: Close up of single fiber test system adhesion surface. ....	105
Figure 5.6: a) Zygo optical profilometer measurement of Kraton G1657 micro molded dry adhesive pillar cast against TC-5030 silicone, imaged after adhesion testing was performed. Center bulge (~300 nm height) likely due to plastic deformation from pillar elongations. Short distance line scans show Ra roughness of ~4 nm, b) SEM side view of fiber. ....	106
Figure 5.7: Single fiber test system; load cell to linear stage and probe to load cell connection. ....	107
Figure 5.8: Single fiber test probe and fiber assembly illustration. ....	108
Figure 5.9: Load cell cantilever stiffness test. x-axis represents elapsed time and, as linear stage was displaced at 1 µm/s, also equal to load cell deflection (direction of motion changes at peak).....	111
Figure 5.10: Complete single fiber test system.....	113
Figure 5.11: Single fiber (100 µm Kraton G1657 on polystyrene adhesion surface) preload test. ....	114
Figure 5.12: Time at preload vs. adhesion force results (for 100 µm Kraton G1657 on polystyrene adhesion surface).....	116
Figure 5.13: 100 µm diameter Kraton G1657 single fiber adhesion (run 1-5)	

compared to two FEA model results with fixed cap boundary condition.....	117
Figure 5.14: Kraton G1657 160 $\mu\text{m}$ diameter fiber single fiber adhesion (run 1-3) compared to FEA model result with fixed cap boundary condition. ....	118
Figure 5.15: Kraton G1657, 120 $\mu\text{m}$ diameter straight cylinder post fiber single fiber adhesion (run 1-3) compared to FEA model result with fixed cap boundary condition. ....	118
Figure 5.16: ST-1060, 100 $\mu\text{m}$ diameter fiber single fiber adhesion (run 1-3) compared to FEA model result with fixed cap boundary condition. ....	119
Figure 5.17: ST-1060, 160 $\mu\text{m}$ diameter fiber diameter fiber single fiber adhesion (run 1-3) compared to FEA model result with fixed cap boundary condition....	119
Figure 5.18: ST-1087, 100 $\mu\text{m}$ diameter single fiber adhesion (run 1-3) compared to FEA model result with fixed cap boundary condition.....	120
Figure 5.19: ST-1087, 160 $\mu\text{m}$ diameter fiber diameter fiber single fiber adhesion (run 1-3) compared to FEA model result with fixed cap boundary condition....	120
Figure 5.20: ST-1087, 200 $\mu\text{m}$ diameter fiber diameter fiber single fiber adhesion (run 1-3) compared to FEA model result with fixed cap boundary condition....	121
Figure 5.21: Relaxation tests for Kraton G1657 160 $\mu\text{m}$ fiber, experimental vs. FEA.....	126
Figure 5.22: Normalized force from relaxation tests, comparing single fiber adhesion tests to Instron bulk material tests. ....	127
Figure 5.23: Shear tests method illustration: (1) represents the original undeformed fiber, (2) shows the axial preload stage (1 mN), (3) shows the pure shear deformation, and (4) gives the final axial elongation until adhesion was lost (this was the stage from which load cell data is given in the next figures.....	128
Figure 5.24: Kraton G1657 100 $\mu\text{m}$ fiber showing axial load cell forces from a 460 $\mu\text{m}$ sheared fiber and pure axial pull back. ....	129
Figure 5.25: Kraton G1657 160 $\mu\text{m}$ fiber showing axial load cell forces from a 90 $\mu\text{m}$ sheared fiber and pure axial pull back. ....	129
Figure 5.26: Axial elongation results for Kraton G1657, 160 $\mu\text{m}$ fiber with three	

different adhesion surfaces. ....	131
Figure 5.27: Axial elongation results for ST-1060, 160 $\mu\text{m}$ fiber with three different adhesion surfaces. ....	131
Figure 5.28: Axial elongation results for ST-1087, 160 $\mu\text{m}$ fiber with three different adhesion surfaces. ....	132
Figure 5.29: Fiber cap shrinkage tests for Kraton G1657, 100 $\mu\text{m}$ diameter fiber on glass adhesion substrate. ....	133
Figure 5.30: Fiber cap shrinkage tests for Kraton G1657, 160 $\mu\text{m}$ diameter fiber on glass adhesion substrate. ....	133
Figure 5.31: Images a), b) and c) are of a 160 $\mu\text{m}$ diameter Kraton G1657 fiber on glass with zero tensile load, maximum normal load, and maximum shear displacement before failure respectively. ....	134
Figure 5.32: Kraton G1657, 100 $\mu\text{m}$ diameter fiber (experimental vs. FEA). Test consists of: preload with 1 mN pressure ( $\sim 30 \mu\text{m}$ ), shear 90 $\mu\text{m}$ , followed by a pure normal elongation until loss of adhesion. ....	135
Figure 5.33: Friction coefficient calculation: a) 100 $\mu\text{m}$ Kraton G1657 fiber: dotted line is first contact and image is the slide fiber after 150 $\mu\text{m}$ shear. b) FEA of fiber sheared 150 $\mu\text{m}$ and extended 86 $\mu\text{m}$ (30° pull angle). ....	136
Figure 5.34: Fiber array peel test method using fish scale. ....	137
Figure 5.35: Gecko adhesive top cap boundary selection flow chart. ....	139
Figure 8.1: Optical images of silicone die after EBL exposure and final development; a) 1 $\mu\text{m}$ diameter post array with dose variations showing over exposure or over development in the text, b) line and post array with sizes ranging from 600 nm to 2.5 $\mu\text{m}$ , c) post array with sizes ranging from 2 $\mu\text{m}$ to 500 nm with only largest features able to develop PMGI all the way through, d) 1, 2, and 3 $\mu\text{m}$ posts showing signs of some undercut from the dark perimeter of the circles. Scale bars represent 5 $\mu\text{m}$ . ....	159
Figure 8.2: Optical microscope images of PDMS cast from EBL patterned silicon die, a) line features with 400 nm – 1.5 $\mu\text{m}$ widths, bright blue areas show	

overhanging cap, b) circular post features with 800 nm – 4 μm diameters. String like debris are torn off PDMS caps which did not survive de-molding..... 160

Figure 8.3: SEM images of gold coated PDMS structures cast from EBL patterned die, a) full image of EBL mask, b) top view of 800 nm – 3 μm wide features showing bright perimeters where cap survived de-molding, c) 6 μm diameter fiber with slightly overhanging cap, d) 4 μm diameter fiber with overhang, e) 2 μm diameter fibers with rounded overhang, likely folded during gold deposition, f) array of various size fibers showing much shorter smaller features suggesting PMGI did not fully develop. .... 161

## List of Nomenclature

<i>Au</i>	Gold
<i>BC</i>	Boundary condition
$c_1, c_2\dots$	Maxwell model damping
$C_i$	Mooney Rivlin strain energy density function
<i>CMC</i>	Canadian Microelectronics Corporation
<i>COC</i>	Cyclic olefin copolymer
<i>Cr</i>	Chrome
<i>DUV</i>	Deep ultra violet light
<i>EBL</i>	Electron beam lithography
<i>FEA</i>	Finite element analysis
$I_i$	Strain invariants of the right Cauchy-Green deformation tensor
<i>IPA</i>	Isopropyl alcohol
<i>J</i>	Volume ratio
<i>k</i>	Bulk modulus
$k_1, k_2\dots$	Maxwell model stiffness
<i>MEMS</i>	Micro electro mechanical systems
<i>MIBK</i>	Methyl isobutyl ketone
<i>MR</i>	Mooney Rivlin model
<i>PDMS</i>	Polydimethylsiloxane

<i>PMGI</i>	Polymethylglutarimide
<i>PMMA</i>	polymethylmethacrylate
<i>PS</i>	Polystyrene
<i>PSA</i>	Pressure sensitive adhesive
<i>REM</i>	Micro replication molding
<i>SEBS</i>	Styrene-ethylene/butylene-styrene
<i>SEM</i>	Scanning electron microscope
<i>UV</i>	Ultra violet light
$\sigma_{ii}$	Cauchy stress

# 1 INTRODUCTION

Gecko inspired adhesives are an emerging application of microfabrication technologies. As bioinspired adhesives have only been developed in the early twenty-first century, most work is still mostly in the research phase. However, a few groups around the world have recently begun to commercialize the technology [1,2]. This chapter introduces the basic principles by which these biomimetic adhesives function and lists possible applications which have been examined in literature. Literature shows that while a wide range of designs with strong adhesion have been developed, to take this technology to the next step and make it a commercial product, more information on durability and design optimization is required. To help achieve these goals, this work provides a summary describing material property testing and simulations developed along with an outline of the topics included in this project.

## 1.1 Gecko Inspired Dry Adhesives Materials

Early in the last decade it was discovered that the adhesion capabilities of geckos, as well as those of some insects, are mainly due to van der Waals intermolecular forces [3]. Alternative theories that adhesion principle is based on capillary forces were disproved by examining different surface energy and different polarized materials [3]. Van der Waals forces, at least an order of magnitude weaker than molecular bonds, include dipole-dipole (Keesom) forces;

dipole-induced dipole (Debye) forces; and instantaneous dipole-induced dipole (London dispersion) forces [4].

Van der Waals attraction forces are considered “surface” forces as they act over extremely small distances (negligible after a few tens of nanometers separation distance). The attraction potential,  $U_{vdW}$ , between two molecules is proportional to the inverse sixth power of the separation distance  $r$  as shown in equation 1.

$$U_{vdW-molecules} = \frac{-C}{r^6} \quad (1)$$

Where  $C$  is a constant which depends on the dipole moment properties of the material. The attraction between two macroscale flat plates can be found by a double integration over two half space volumes, as described in equation 2.

$$U_{vdW-flat\ plates} = \int_{V_1} \int_{V_2} U_{vdW-molecules}(r) dV_1 dV_2 \quad (2)$$

The attraction force,  $F_{vdw}$ , between two flat plates is then found by differentiating with respect to the plate separation distance  $d$  giving the adhesion force applicable to gecko adhesive structures in equation 3 [4].

$$F_{vdw} = \frac{A}{6\pi d^3} \quad (3)$$

Where  $A$  is the material Hamaker constant, generally in the range of  $10^{-19}$  to  $20^{-20}$  Joules for most surfaces [4].

As the van der Waals attraction force vanishes rapidly with separation distance, meaningful adhesion for relatively stiff materials such as those of the gecko foot hair can only be achieved by ‘*contact splitting*,’ the principle of splitting contact into finer sub-contacts to increase surface conformity (commonly used in natural adhesion systems) [5]. Geckos use a complex hierarchical combination of micro (setae hair) and nanostructures (flat tipped spatula branches) on their foot pads (see Figure 1.1) to allow these smaller features to make intimate contact with the adhesion surface in order to maximize the van der Waals adhesion force.

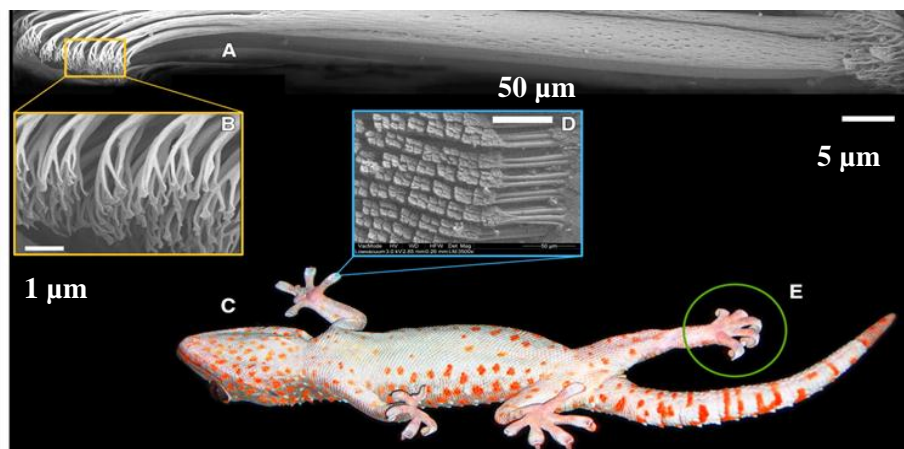


**Figure 1.1: SEM images of hierarchical adhesion mechanism: (A) one setae branch, (B) Array of nanoscale spatula tips on the end of the setae branch, (C) tokay gecko climbing a glass surface, (D) Array of setae, (E) Toe peeling creating a controlled detachment. Printed from [6] with permission.**

With an understanding of the principles allowing geckos to achieve strong reversible adhesion, researchers have developed synthetic versions of the contact splitting features which can be replicated in polymeric materials, giving similar adhesion results [7-9]. While van der Waals forces are the dominant factor in these bioinspired dry adhesives, recent work has shown that depending on the adhesive material and contact surface used, significant electrostatic forces can also occur [10]. Figure 1.2 illustrates several examples of single and double layer hierarchy polymer micro and nano posts developed as dry adhesive materials.

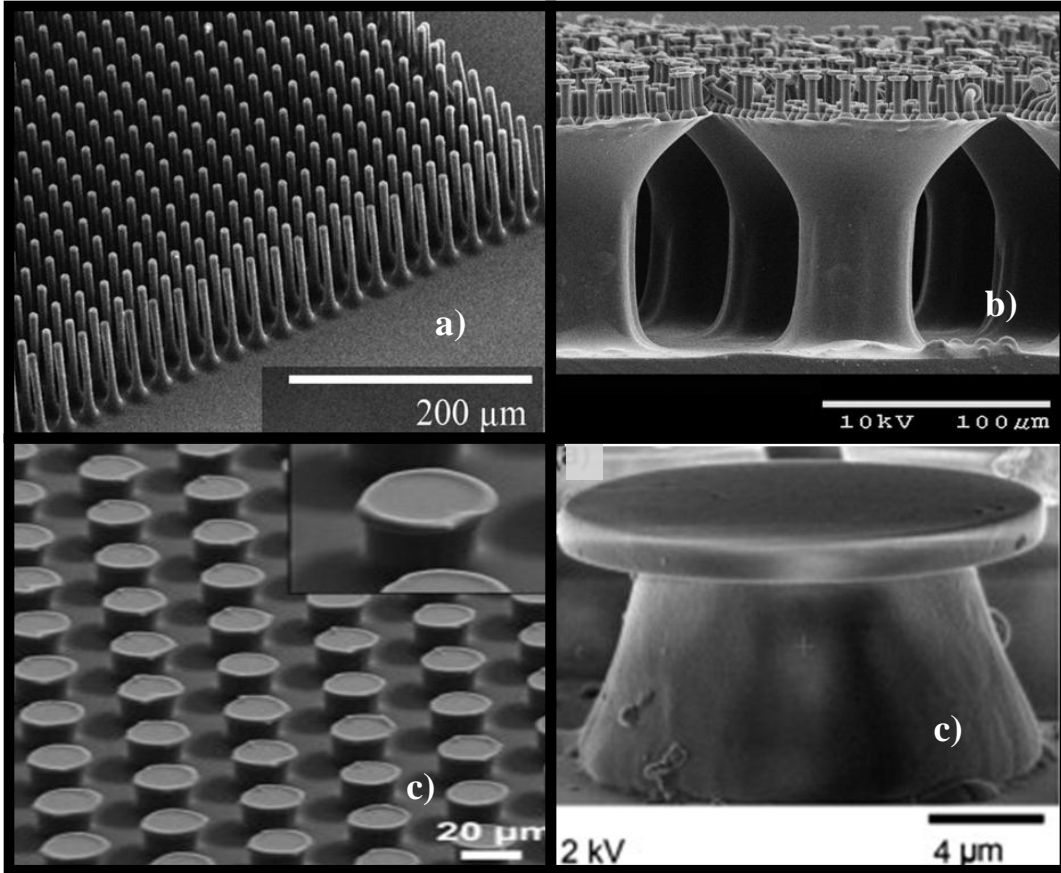


**Figure 1.2: Examples of dry adhesive pillar designs in literature: a) high aspect ratio angled microfibers adhesive arrays. Reprinted with permission from [11] Copyright 2007 American Chemical Society, b) hierarchical fibers with overhanging features on both micro and nano length scales. Reprinted with permission from [12] Copyright 2009 American Chemical Society, c) low aspect ratio pillars with mushroom shaped top cap. Reprinted from [13] Copyright 2008 with permission from Elsevier, d) close up of individual fiber with large cap undercut. This figure was published in [14] Copyright 2013 Elsevier Masson SAS. All rights reserved.**

## 1.2 Gecko Adhesion: Advantages and Applications

Gecko inspired dry adhesives have many advantages over pressure sensitive adhesives (PSAs) due to their unique properties. Dry adhesives can achieve higher adhesion capacity than PSAs [15] allowing for a wide range of possible applications. The adhesives can also be made double sided and directional [16]. These materials are inherently non-tacky, easily controlled detachment, durable, and potentially self-cleaning [17]. Dry adhesives also have the ability to work in vacuum and underwater [18].

The tremendous advantages dry adhesives offer, as compared to PSAs, have inspired multiple potential applications which could benefit from implementing these materials. One example of interest in our lab is the manipulation of micro electro mechanical (MEMS) components for pick-and-place assembly [19]. The non-transferring, controllable adhesion capable with this technique could replace manual tweezers operations and functions in the most suitable environment for synthetic dry adhesives: clean and extremely smooth surfaces. A variation of pick-and-place assembly proposes using a single post as a stamp to transfer individual components for micro device assembly [20]. Other groups have used the adhesives as propulsion mechanisms for wall climbing robots [9]. Robotic uses for adhesives are also of interest for space applications [14] as the adhesive can operate in a vacuum. The controllability of adhesion has been utilized by others to create attachment pads for micro air vehicles (MAVs) [21].

Gecko adhesives have also been proposed for use in the health care industry [22]. The toxicity of ordinary PSA tissue adhesives can cause undesirable irritation to the skin. Existing wound closure techniques also give poor adhesion on wet surfaces. Recent work is targeting this application and modifying dry adhesive properties to allow improved adhesion on rough, soft surfaces [22]. Other groups are developing medical skin patches to be integrated with existing diagnostic devices to monitor body signals [23].

### 1.3 Polymers in Dry Adhesive Research

Gecko inspired adhesives, generally fabricated with polymer replica molding techniques [24], allow the flexibility to use a wide variety of materials with limited process modifications. Selecting the most appropriate structural material for the designed application is critical as an enormous range of polymer properties are available. Due to its extensive use in microfluidics [25] and proven micro replication capabilities [26,27], polydimethylsiloxane (PDMS) has been adapted by multiple groups as a dry adhesive material [14,28-30]. Improved durability can be achieved by using polyurethane elastomers with materials such as ST-1060 [7] and ST-1087 [31]. Elastomers are capable of extremely high elongations without significant plastic deformations, making them an ideal choice for synthetic dry adhesives as harder materials tend to be plastically deformed after repeated use. Electrically conducting composites, made by adding nanoparticles such as carbon black, have been used with both PDMS [32] and ST-1060 [19] allowing active adhesion with an applied voltage as well as preventing

static charging for adhesive used in delicate micro component assembly. Using composite materials as adhesives opens more possibilities, and other groups have used a magnetic field with a magnetoelastomer to change the adhesion force by an order of magnitude [33].

Recently the use of thermoplastic elastomers in microfabrication has seen many improvements [24,34-39]. Thermoplastics have the advantage of significantly reduced manufacturing cycle times and material costs when compared to polyurethanes and silicones. Employing these materials to gecko adhesives provides an important step in commercialization the technology [40]. As thermoplastics are relatively new in the field of microfabrication, limited material properties are available in literature. Awareness of mechanical properties when selecting materials is important for dry adhesive fabrication, as documented by a group reporting adhesion loss due to increased viscoelasticity in an epoxy based liquid resin (DER 331) [41].

#### 1.4 Dry Adhesive Simulations

To achieve a better understanding of the gecko adhesion principle, design improved adhesive fiber shapes, and select appropriate structural materials, accurate simulations are essential. Finite element analysis (FEA) simulations for the gecko's spatula using a contact mechanics formulation provides a model to investigate the interactions with various surface asperities [42], important for optimizing future synthetic adhesives used on rough surfaces.

Using the understanding of the adhesion phenomena developed, models for synthetic dry adhesives have made important findings for design optimization. An analytical model based on the crack propagating energy barrier provides an important correlation between the cap overhang (small undercut on the top portion of the fiber) and adhesion strength [43]. This simulation identified three main failure modes for gecko inspired adhesives: *Mode 1* – adhesion loss from the pillar edge by crack propagation due to stress concentrations at the perimeter (common for straight pillar), *Mode 2* - crack propagation induced by nucleation from interfacial defects (common in overhanging cap fibers), and *Mode 3* – idealized instantaneous adhesion loss through the fiber cap due to attaining the theoretical van der Waals adhesion limit (generally never realized experimentally as some defects always exist, forcing *Mode 2* failure) [43]. As *Mode 1* failure occurs at the lowest pressures, stress concentrations at the fiber edge should be prevented. Simulations (confirmed with experimental data) have given a general consensus that overhanging cap fibers produce better adhesion than straight pillars [13,20]. Using the analytical model developed, finite element simulations of fabricated fiber geometries were used to optimize fiber cap overhang dimensions [44]. This model used idealized free roller cap (no constraints in the transverse direction while fully constrained in the axial direction) and fixed cap (fully constrained nodes) interface boundary conditions.

Another important parameter discovered through modeling is the effect of backing layer stiffness on adhesion. Analytical simulation determined that

adhesion forces decrease as backing layer thickness increase due to stress concentrations from the lower compliance of the backing layer [45]. Other work has also realized the need to account for backing layer stiffness in series with fibrillar compliance when modeling the effect of long range forces, causing individual posts to spontaneously extend to come in contact with an adhesion surface [46]. From these results, it is shown that it is important to include the backing layer in the simulation of dry adhesive fibers.

Accurate modeling of polymeric materials requires a complete simulation of mechanical properties and the most accurate boundary conditions possible. While the effect of viscoelasticity on adhesion has been documented [41], it is not widely used in dry adhesive simulations. The gecko setae model [42] includes time dependent effects but only limited synthetic adhesive models include viscoelasticity [47]. Although PDMS has been studied extensively for non-linearity [48], most published dry adhesives models also use a linear elastic material model, neglecting strong hyperelasticity in polymer materials. Published dry adhesive models also only use fixed or roller boundary conditions, overlooking important frictional adhesion mechanisms [49].

## 1.5 Single Fiber Adhesion Testing

Any simulation will require experimental testing to validate the results. As the appropriate boundary conditions are unclear for these materials, examination of the adhesion phenomena is also required to develop more accurate models. The

most common method for testing synthetic dry adhesive samples is a hemispherical indenter test [11,50]. In this technique a hemispherical indenter (typically glass or sapphire) of several millimeters in diameter is brought into contact with the adhesive fiber array with a known preload. The indenter is then withdrawn while measuring the adhesion force using a load cell. Hemispherical indenters are used as it reduces the alignment precision required for flat contact surfaces. Using this method, however, has intrinsic limitations, making it difficult to determine accurate response of a fiber. Figure 1.3 shows an illustration of a glass sphere contacting an array of pillars, demonstrating how central fibers contact the glass surface first, causing buckling while outer fibers will still be in tension [11,50]. This method causes an adhesion contact area dependent on the preload as more fibers at the perimeter get in contact as the sphere is indented further into the adhesive array. Finally, due to the curvature of the glass, the adhesion interface cannot be imaged easily as light passing through the sphere will be refracted and distort the image.

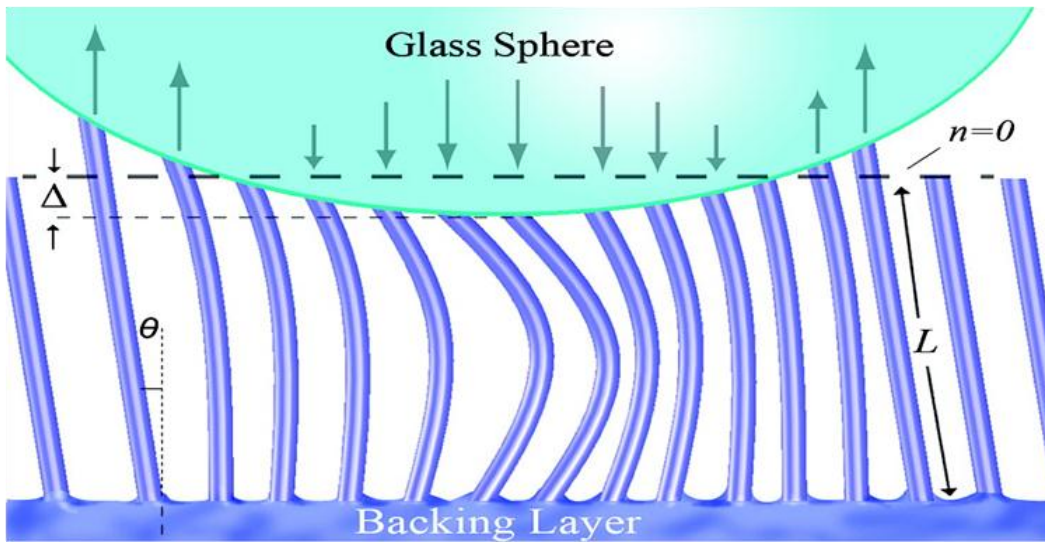


**Figure 1.3: Illustration of hemispherical adhesion testing (image shows angled posts but straight fibers will have the same effect). Reprinted with permission from [11] Copyright 2007 American Chemical Society.**

To be able to achieve more accurate results, which can be used to compare with simulations, a single fiber flat-surface adhesion test is required [51-53]. Using transparent contact surfaces allows this method to also image the contact interface. Single fiber tests systems are much more vulnerable to misalignments as a flat-flat contact is required. However, this angle dependency has been shown to be mostly negated (for up to  $2^\circ$  tilt angle) by using mushroom shaped (overhanging cap) fibers, also giving better adhesion results. Vertical walled (no overhang) fibers demonstrate ~50 percent adhesion loss with a  $2^\circ$  tilt misalignments while mushroom shaped fibers show constant performance [54]. This can be explained by the already vulnerable (with stress concentration) cap edges given extra peel loading from the tilt misalignment. It has been attempted to

image the moment of adhesion failure to study the crack propagation phenomena. However, even with 180,000 frames per second high speed imaging, the failure could still not be resolved [52]. However, adhesion interface imaging has shown that the fiber cap can shrink up to 25 percent due to Poisson's ratio contraction forces while remaining in contact with a surface [52]. While this effect is important to consider in modeling the boundary condition, it has been previously found that cap area reduction (determined to be independent of pull off speed) has no effect on the normal adhesion pressure [51].

## 1.6 Motivation and Outline of Project

The objective of this thesis is to provide design guidelines for bio-inspired dry adhesives geometries and material selection. An improved understanding of material properties, their effect on gecko adhesion, and the ability to model adhesives more accurately could be vital factors in improving adhesive performance and durability required to commercialize a product. This work also outlines methods for dry adhesive fabrication using thermoplastics which has the potential to greatly reduce production time and costs of these materials.

General fabrication guidelines were created by in depth material property testing and developing an improved finite element simulation to account for the complexity of the materials used. Mechanical material properties of three polymers were tested: Kraton G1657 styrene-ethylene/butylenes-styrene (SEBS), ST-1060, and ST-1087 polyurethane elastomers. These materials were chosen due

to their previous use in our lab and their ability to replicate microstructures precisely. The polymers investigated can be employed in many other fields of microfabrication, especially in microfluidics as a replacement for PDMS, and provides the first in depth characterization of non-linearity and viscoelasticity for these materials. From bulk material properties determined, a finite element simulation was created using COMSOL. This model integrates both hyperelasticity and viscoelastic (in separate models) and investigates three possible boundary conditions (fixed, roller, and frictional cap interface). Due to the extremely high elongations dry adhesive fibers can achieve (up to 500%), convergence of non-linear material models in COMSOL can become difficult. To verify the simulation and examine the adhesion interface, single fiber adhesives were fabricated using methods previously developed in our lab, but with much larger feature sizes ranging from 60  $\mu\text{m}$  to 200  $\mu\text{m}$  diameter. These larger fibers were required to be able to detect the adhesion signal without significant noise. Lessons learned can be appropriately applied to scaled down fiber sizes when model accuracy is good. A single fiber test system was developed allowing for direct comparison of force vs. elongation results from a fabricated single fiber with the simulation. The testing system also allowed real-time imaging of the fiber during adhesion trials to investigate the cap-surface interface. The simulation developed in this work is the first published to examine hyperelastic modeling of gecko inspired adhesives and to implement a frictional adhesion interface boundary condition.

The contents of this thesis are organized as follows:

- In Chapter 2 a bulk material analysis is presented for three polymers. Experimental uniaxial tests are used to fit hyperelastic (Mooney Rivlin strain energy density function) and viscoelastic (Maxwell) models which can be implemented in commercial finite element analysis software such as COMSOL. Along with these material constants, the plasticity of the polymers is examined through cyclic loading experiments.
- In Chapter 3 the finite element simulation of a single dry adhesive fiber is developed. This section examines how to implement the hyperelastic and viscoelastic models in COMSOL. A description of the boundary conditions used (fixed, roller, and frictional) is also given along with the implications for each choice.
- In Chapter 4 the fabrication steps for the single fiber tests samples used in this work are described. A photomask, designed for this project is presented and clean room process parameters are provided. At the end of the chapter, four fiber shapes are described which were used for experimental adhesion testing and compared with simulations in this work.
- In Chapter 5 a single fiber test system is developed. This section provides an outline of how this setup was assembled and how to operate it for future work. The four fibers fabricated in Chapter 4 were tested using this system and compared to simulation results from the model developed in Chapter 3.

## 2 ELASTOMER MATERIAL CHARACTERIZATION AND MODELING

### 2.1 Introduction

This chapter investigates mechanical material properties of three elastomers chosen for this work. Through experimental testing of bulk polymers, parameters of material models chosen to describe the characteristics of the polymers were determined. The hyperelasticity (using Mooney Rivlin models), plasticity, and viscoelasticity (using a Maxwell model) were examined. These parameters were required to produce accurate finite element simulations and understand how material behavior affects dry adhesives. Previously published simulations, outlined in chapter 1, have assumed a linear elastic material model, which is an invalid assumption from previous testing in our lab which showed extremely large elongations (several hundred percent) of fibers. All tests performed in this section were completed on an Instron uniaxial test system using bulk material samples<sup>1</sup>.

Three materials were chosen as a focus for this work: Kraton G1657 styrene-ethylene/butylene-styrene (SEBS) thermoplastic elastomer, ST-1060 and ST-1087 polyurethane elastomers. These materials were chosen based on replication fidelity, appropriate stiffness ranges, and previous use in the research

---

<sup>1</sup> Sections of this chapter have been submitted to the Journal of Micromechanics and Microengineering [55]

group [7]. This chapter outlines the tests performed, provides a background on the material models used, and shows material data fits which can be implemented in finite element analysis (FEA) software. Some of these polymers also show excellent potential for use in microfluidic applications [34-37,56] to replace commonly used polydimethylsiloxane (PDMS).

## 2.2 Instron Uniaxial Test Method

With the large elongations elastomers are capable of surviving without failure, non-linear stress-strain data is generally observed with these rubbery materials. To determine the material properties of the chosen polymers, multiple tests were performed using an Instron single column tabletop system, model number 5943 with 2710-113 clamps and a 1 KN load cell, see Figure 2.1. A pure uniaxial test was sufficient for this work because the dry adhesive fibers are predominantly loaded axially. As described in ASTM D882-12 (Standard Test Method for Tensile Properties of Thin Plastic Sheeting) [57], plastic samples of thickness 1.0 mm and less do not require the use of a dumbbell shape sample to localize the stresses in the neck as is generally used for Instron testing. This was advantageous due to the simplicity of cutting rectangular shaped samples. As the elongation for all the materials was high, a relatively small gauge length (~30 mm) was chosen. Test samples of four different materials were cut with a scalpel and ruler to 50 mm x 10 mm x 1 mm sizes. All tests were performed at room temperature (~22°C).

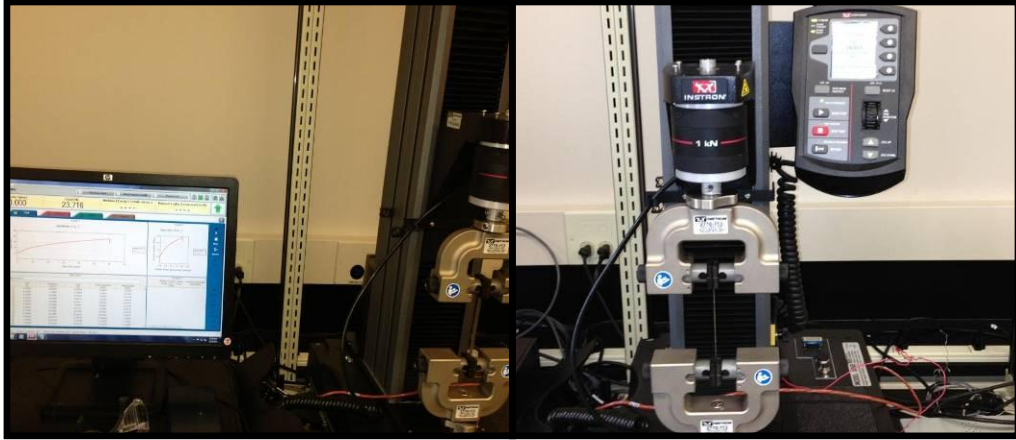


**Figure 2.1: Instron testing system and computer controlled software setup.**

### 2.3 Test Sample Casting

Three polymers useful for micro molding applications were examined in this work. General properties provided by the supplier are summarized in Table 2-1. Kraton Performance Polymers, Inc. supplies a wide variety of thermoplastic elastomers useful for micro molding applications. The G1657 version was chosen due to its good replication fidelity caused by a high melt flow index. G1657 is a linear triblock copolymer with polystyrene providing rigid links in the polymer chains [58] which due to its chemical structure may be easily blended with polymers like polypropylene and polystyrene. ST-1060 [59] and ST-1087 [60] are thermoset polyurethane elastomers supplied by BJB Enterprises. Both these materials come in a two-part liquid form, which when mixed has approximately a 25 minute working time during which the casting and degassing should be completed. Both polyurethanes show excellent replication fidelity with no observable mold damage after tens of cycles.

**Table 2-1: Materials tested, properties from data sheets [58-60]**

<b>Material</b>	<b>Kraton G1657</b>	<b>ST-1060</b>	<b>ST-1087</b>
<i>Hardness (Shore A)</i>	47	60	85
<i>Supplied as:</i>	Dusted pellets	2 part liquid	2 part liquid
<i>Color</i>	Transparent	Amber	Amber
<i>Viscosity (cP) @ 25°C</i>	NA	4750	2700
<i>Flow index (gms/10 min)</i>	22	NA	NA
<i>Elastic modulus (MPa)</i>	2.4 at 300%	2.9	9.8

**2.3.1 Thermoplastic Test Samples**

Two methods for molding Kraton, supplied by the manufacturer as dusted pellets were examined. The first method attempted for manufacturing solid sheets of Kraton was by placing material pellets on a Teflon sheet heated on a hotplate. For uniform samples, it was important to arrange the pellets in a way with the least possible air gaps surrounding pellets while having no pellets suspended or resting on top of other of each other. See Figure 2.2.



**Figure 2.2: Thermoplastic test sample preparation.**

A small 1 mm Teflon spacer was added to ensure uniform thickness. The thermoplastic pellets are covered with another Teflon sheet, followed by thin metal plate to provide a rigid surface, and finally a 5 kg weight all on a hotplate set to at 200 °C to allow the polymer to melt sufficiently. It was found that for reasonable casting times, the weight alone was not enough; it was required to manually push the weight, giving an estimated total weight of ~15 kg. See Figure 2.3. Note, another thin metal plate was also used between the hotplate and the Teflon to prevent contamination of the hotplate.

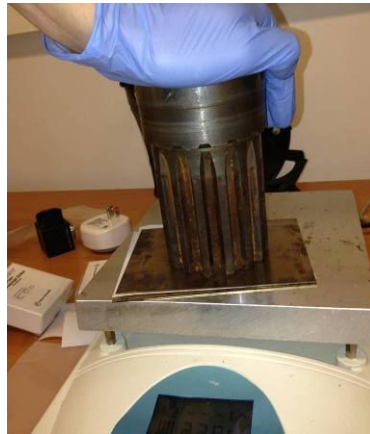


**Figure 2.3: Melting thermoplastic pellets to form Instron bulk material test samples.**

Finally, the samples were cut using a scalpel knife and a ruler to the correct size. While this produced visually homogenous samples, Instron tests showed large variations in the material properties. Figure 2.4 shows the stress-strain curve for 5 consecutive tests of Kraton G1657, showing poor reliability.

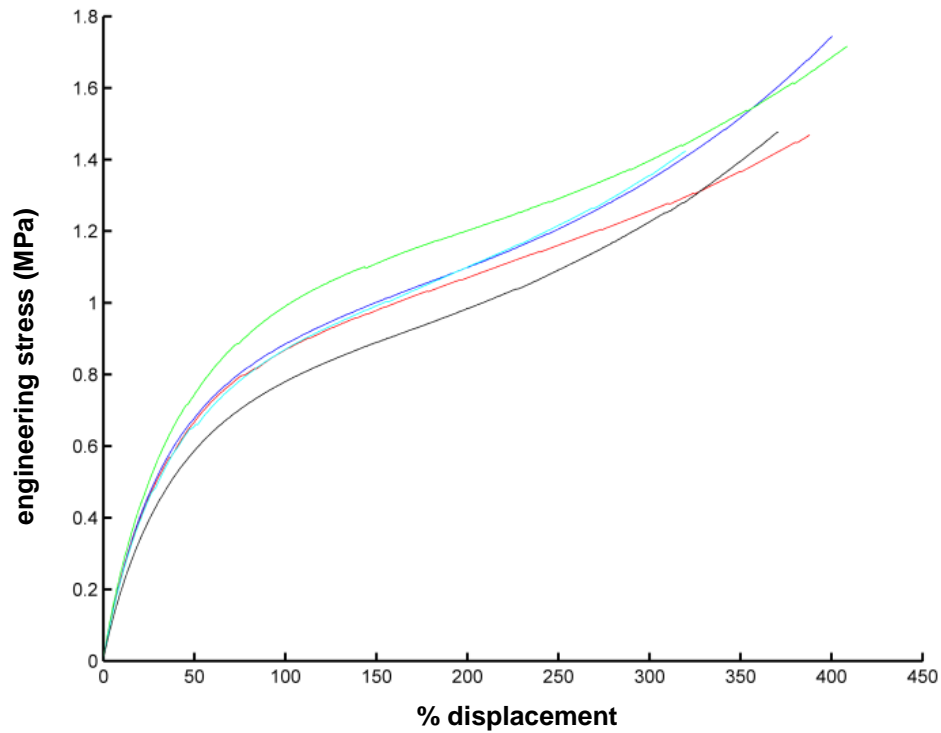


**Figure 2.4: Inconsistent material properties of Kraton G1657 (hot plate method).**

These inconsistent results suggest that the hot plate method did not create a completely homogenous polymer sample, but rather maintained the internal boundaries from the original pellets from which it was cast, as described in Figure 2.5.

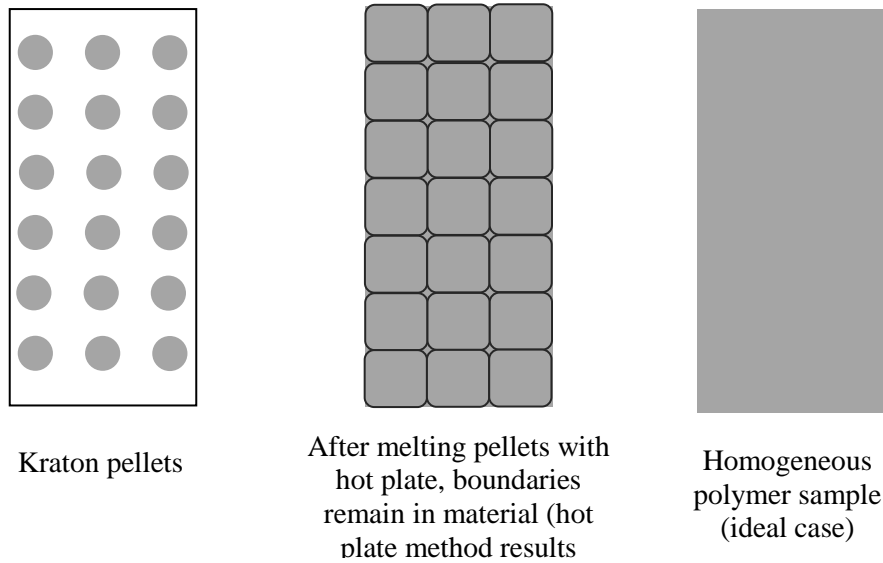


**Figure 2.5: Illustration of macro scale thermoplastic pellet melting and the non-uniform (not optically observable) structure compared with the ideal homogenous melted polymer sample.**

To solve this problem, the polymer needed to be further processed without increasing the temperature, which could damage the polymer chains. This was accomplished by using a commercially available hot glue gun (Stanley Pro Dual Melt Glue Gun), with an operating temperature of 193°C. The thermoplastic was first pre-processed to make sticks, similar to the glue sticks for which the device was built. These polymer sticks were made by pre-forming a piece of aluminum foil to the glue sticks, filling with thermoplastic pellets, and tightly wrapping to keep in place. The polymer was then slightly melted in the aluminum foil on a hot plate at 180°C until the pellets were bound together. Figure 2.6 shows the completed polymer sticks.



**Figure 2.6: Image of Kraton G1657 sticks for glue gun processing.**

The Kraton sticks were then fed into the glue gun and extruded directly onto a glass slide on a hot plate at 200°C, as shown in Figure 2.7 a). To give a smooth surface of the Kraton sample, a silicone sheet was placed onto the extruded polymer, followed by a thin metal sheet, and a 5 kg weight, see Figure 2.7 b), c). The sample was then removed from the hot plate and left to cool. Smooth Kraton has low adhesion to glass and silicone, allowing it to be easily removed. This sample was then cut to 1 mm x 10 mm x 50 mm size using a scalpel, giving the final strip to be tested with the Instron, Figure 2.7 e). This process was advantageous as the maximum processing temperature required was 200°C and only requires several tens of seconds to re-flow. This reduced risk of heat damage to the polymer structure as well as provided a much quicker manufacturing method.

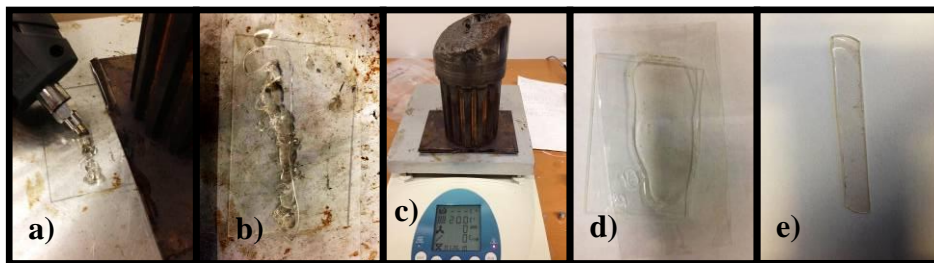


**Figure 2.7: Kraton sample preparation: a) glue gun extrusion of Kraton on glass slide, b) cover Kraton with plastic sheet (cyclic olefin copolymer (COC) [61]), c) place metal sheet over sample and add weight for 10 seconds, d) cool Kraton sample enclosed in glass/COC sheet, e) final sample after cutting with scalpel.**

### 2.3.2 Thermosets

Two thermoset polyurethane elastomers were examined, ST-1060 and ST-1087 supplied by BJB Enterprises. These polymers were prepared within a thin metal plate, a Teflon sheet (on each side), and a 1 mm Teflon spacer. The prepolymer was mixed by weight ratio according to supplier recommendations [59,60] and degassed for 10 minutes to remove most of the air bubbles. After carefully pouring the prepolymer into the spacer it was again degassed for 15 minutes. Covered with Teflon/metal the material was then squeezed into the mold with magnets on the two metal sheets and paper clips along the edges. See Figure 2.8 for detailed images of the sample preparation process. The curing schedule used for ST-1060 and ST-1087 was 24 hours at room temperature and 16 hours at 80°C.

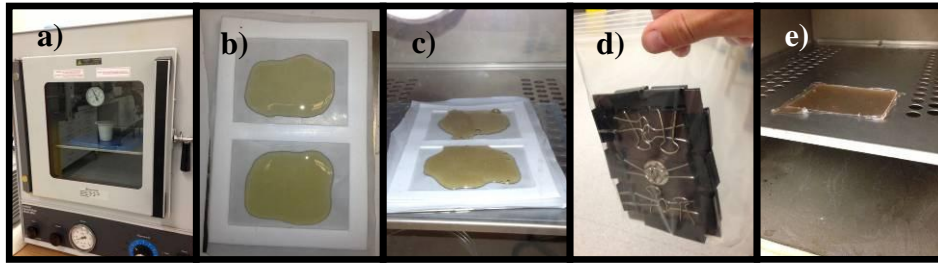


**Figure 2.8: Polyurethane test sample casting procedure: a) vacuum degas prepolymer in container, b) pour prepolymer on Teflon sheet between the Teflon spacer, c) vacuum degas on Teflon mold, d) cover with Teflon sheet and metal plate, secure with a magnet on each side and paper clips along the edges. Cure for 24 hours, e) bake polymer sheets at 80°C for 16 hours.**

## 2.4 Hyperelasticity

### 2.4.1 Mooney Rivlin Model

As polymers exhibit non-linear material properties at large elongations, it was necessary to account for hyperelasticity in creating micro fiber models. To develop a numerical model of the material behavior determined from Instron tests, it was assumed the polymers were incompressible, isotropic, and non-linear elastic. As the length scales of the structures (tens of microns) examined are significantly larger than intermolecular spacing, we assumed continuum mechanics formulations can be used. To describe the deformation properties of the materials, a scalar valued strain energy density function was used. To avoid numerical instabilities, the simplest and lowest order model which gives a good data fit for each material was chosen.

The single inflection point stress-strain curve of ST-1060, see Figure 2.9, allows a simple two-variable Mooney-Rivlin hyperelastic model ( $MR_2$ ), shown in equation 4, to provide an excellent fit. This model is a commonly used hyperelastic fit [62] and has been previously used for PDMS [63]. The experimental data collected from the Instron was used to fit to this strain energy density function, defined in terms of the principal invariants of the right Cauchy-Green deformation tensor [64-66].

$$W_{MR-2} = C_1(I_1 - 3) + C_2(I_2 - 3) + \frac{1}{2}k(J - 1)^2 \quad (4)$$

Where  $W_{MR-2}$  is the general two term Mooney-Rivlin strain energy density function,  $I_1$  and  $I_2$  are the first and second strain invariants (derived from the characteristic equation when finding eigenvalues of the deformation tensor),  $C_1$ ,  $C_2$  are the parameters to be determined,  $k$  is the material bulk modulus and  $J$  is the volume ratio. This model gives good convergence in FEA and can accurately fit simple non-linear curves.

To calculate the  $C_1$  and  $C_2$  fit parameters, the corresponding stress from the strain energy density function needs to be calculated. Assuming the polymer is incompressible makes the volume ratio  $J = 1$ , eliminating the last term in equation 5. The following derivation is reproduced from [64]. The stress is then defined as:

$$\sigma_{ii} = -p + \lambda_i \frac{\partial W}{\partial \lambda_i} \quad (5)$$

Where  $\sigma_{ii}$  is the Cauchy stress,  $p$  is a Lagrange multiplier related to the constraint of incompressibility [62] and  $\lambda_i$  are the stretch ratios, defined as:

$$\lambda = \frac{l}{l_o} = \varepsilon_{eng} + 1 \quad (6)$$

To eliminate the pressure term in equation 5, we take the Cauchy stress difference given in equation 7:

$$\sigma_{11} - \sigma_{33} = \lambda_1 \frac{\partial W}{\partial \lambda_1} - \lambda_3 \frac{\partial W}{\partial \lambda_3} \quad (7)$$

This gives:

$$\begin{aligned} \sigma_{11} - \sigma_{33} = & 2C_1(\lambda_1^2 - \lambda_3^2) + 2C_2 \lambda_1^2 (\lambda_2^2 + \lambda_3^2) \\ & - 2C_2 \lambda_3^2 (\lambda_1^2 + \lambda_2^2) \end{aligned} \quad (8)$$

Using the incompressibility criterion:

$$\lambda_1 \lambda_2 \lambda_3 = 1 \quad (9)$$

And the assumption of simple tension giving:

$$\sigma_{33 \text{ simple tension}} = 0 \quad (10)$$

We can simplify equation 7 to:

$$\sigma_{11} = 2C_1(\lambda_1^2 - \lambda_3^2) + 2C_2 \left( \frac{1}{\lambda_3^2} - \frac{1}{\lambda_1^2} \right) \quad (11)$$

Again using the incompressibility assumption we can simplify the problem to a single stretch ratio using:

$$\lambda_1 = \lambda \quad (12)$$

$$\lambda_2 = \lambda_3 = \frac{1}{\sqrt{\lambda}} \quad (13)$$

From which we can simplify the strain invariants (coefficients of the right Cauchy Green deformation tensor characteristic equation) as:

$$I_1 = \lambda_1^2 + \lambda_2^2 + \lambda_3^2 = \lambda^2 + \frac{2}{\lambda} \quad (14)$$

$$I_2 = \lambda_1^2 \lambda_2^2 + \lambda_2^2 \lambda_3^2 + \lambda_3^2 \lambda_1^2 = 2\lambda + \frac{1}{\lambda^2} \quad (15)$$

Now we can write the uniaxial tension Cauchy stress as a function of the stretch ratio as:

$$\sigma_{11} = 2C_1 \left( \lambda^2 - \frac{1}{\lambda} \right) + 2C_2 \left( \lambda - \frac{1}{\lambda^2} \right) \quad (16)$$

Because the experimental data recorded from the Instron does not measure the instantaneous sample cross section, the data needs to be fit to the engineering stress, given as:

$$\sigma_{eng} = \frac{\sigma_{11}}{\lambda} = 2C_1 \left( \lambda - \frac{1}{\lambda^2} \right) + 2C_2 \left( 1 - \frac{1}{\lambda^3} \right) \quad (17)$$

Commonly written as:

$$\sigma_{eng} = \left(2C_1 - \frac{2C_2}{\lambda}\right) \left(\lambda - \frac{1}{\lambda^2}\right) \quad (18)$$

While equation 18 can fit ST-1060 extremely well, it cannot produce the sharp stiffening curve of ST-1087 or the double inflection point curve of Kraton.

Multiple models can produce a softening/stiffening curve, including the Yeoh 3<sup>rd</sup> order model, Gent chain elongation models, Ogden model, and higher order Mooney-Rivlin models [64]. Both the Ogden and Mooney-Rivlin 5 parameter (MR<sub>5</sub>) gave good data fits but the MR<sub>5</sub> produced a more numerically stable solution in FEA.

The MR<sub>5</sub> model is similar to the MR<sub>2</sub>, with the addition of higher order terms:

$$\begin{aligned} W_{MR5} = & C_1(I_1 - 3) + C_2(I_2 - 3) + C_3(I_1 - 3)^2 \\ & + C_4(I_2 - 3)^2 + C_5(I_1 - 3)(I_2 - 3) \\ & + \frac{1}{2}k(J - 1)^2 \end{aligned} \quad (19)$$

Again, as with the MR<sub>2</sub> model, we assume incompressibility to eliminate the  $\frac{1}{2}k(J - 1)^2$  compressibility term. Equations 5 through 18 already solve the first two terms of this model, so only the final three terms need to be determined.

Repeating steps in Equation 6 to 10, Equation 11 now becomes:

$$\begin{aligned}
\sigma_{11} = & 2C_1(\lambda_1^2 - \lambda_3^2) + 2C_2\left(\frac{1}{\lambda_3^2} - \frac{1}{\lambda_1^2}\right) \\
& + 4C_3(I_1 - 3)(\lambda_1^2 - \lambda_3^2) \\
& + 4C_4(I_2 - 3)\left(\frac{1}{\lambda_3^2} - \frac{1}{\lambda_1^2}\right) \\
& + 2C_5 \left[ (I_2 - 3)(\lambda_1^2 - \lambda_3^2) \right. \\
& \left. + (I_2 - 3)\left(\frac{1}{\lambda_3^2} - \frac{1}{\lambda_1^2}\right) \right]
\end{aligned} \tag{20}$$

Using the incompressible form the strain invariants in equation 14 and 15 and dividing by  $\lambda$  to convert to engineering stress we get:

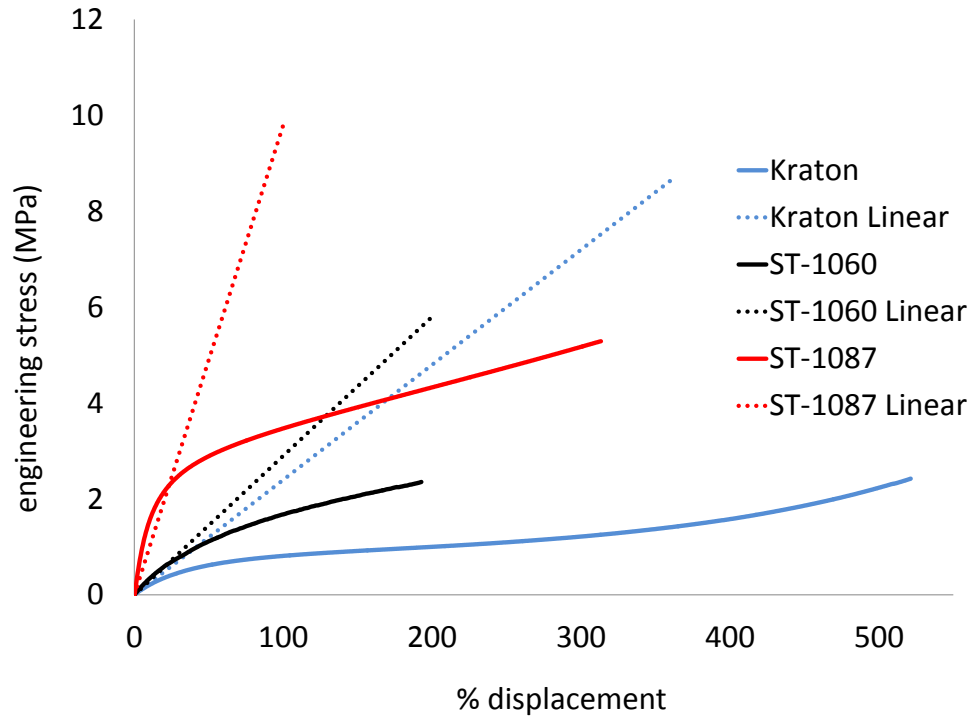
$$\begin{aligned}
\sigma_{eng} = & 2C_1\left(\lambda - \frac{1}{\lambda^2}\right) + 2C_2\left(1 - \frac{1}{\lambda^3}\right) \\
& + 4C_3\left(\lambda^2 + \frac{2}{\lambda} - 3\right)\left(\lambda - \frac{1}{\lambda^2}\right) \\
& + 4C_4\left(2\lambda + \frac{1}{\lambda^2} - 3\right)\left(1 - \frac{1}{\lambda^3}\right) \\
& + 2C_5 \left[ \left(2\lambda + \frac{1}{\lambda^2} - 3\right)\left(\lambda - \frac{1}{\lambda^2}\right) \right. \\
& \left. + \left(\lambda^2 + \frac{2}{\lambda} - 3\right)\left(1 - \frac{1}{\lambda^3}\right) \right]
\end{aligned} \tag{21}$$

Equation 18 and 21 were then fit to experimental data (see next section) using MATLAB with the built in non-linear solver *lsqcurvefit* with the convergence criteria set at  $1e^{-8}$ . As the solution obtained is not unique, stresses should be

plotted well beyond the expected maximum experimental stress to ensure the model behaves appropriately within elongation ranges to be used. Initial conditions were chosen as the linear elastic Young's modulus for each material (2.4 MPa for Kraton, 2.9 MPa for ST-1060, and 9.8 MPa for ST-1087 [58-60]).

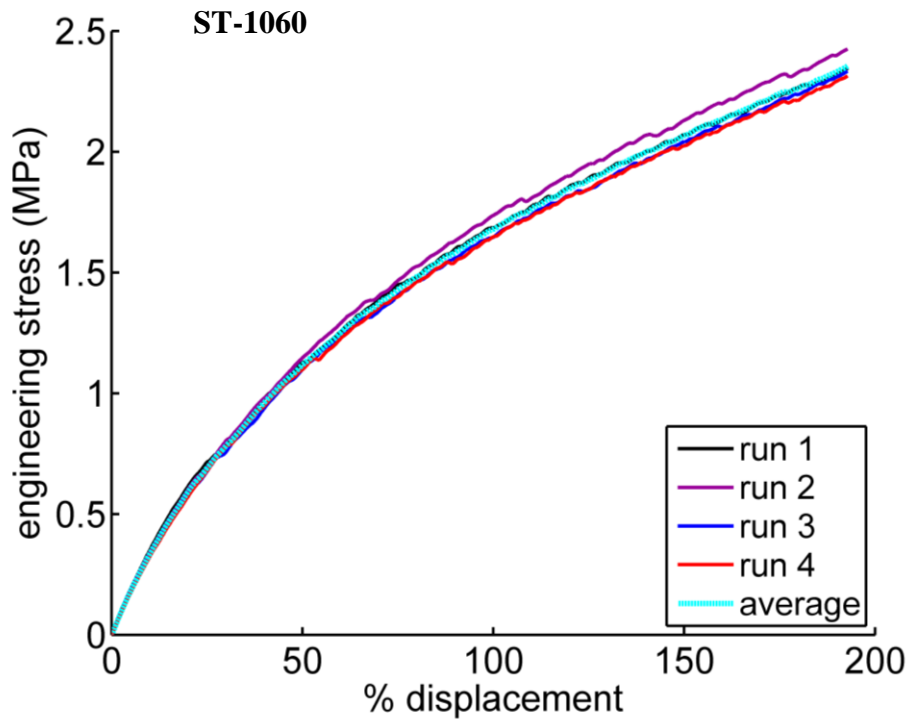
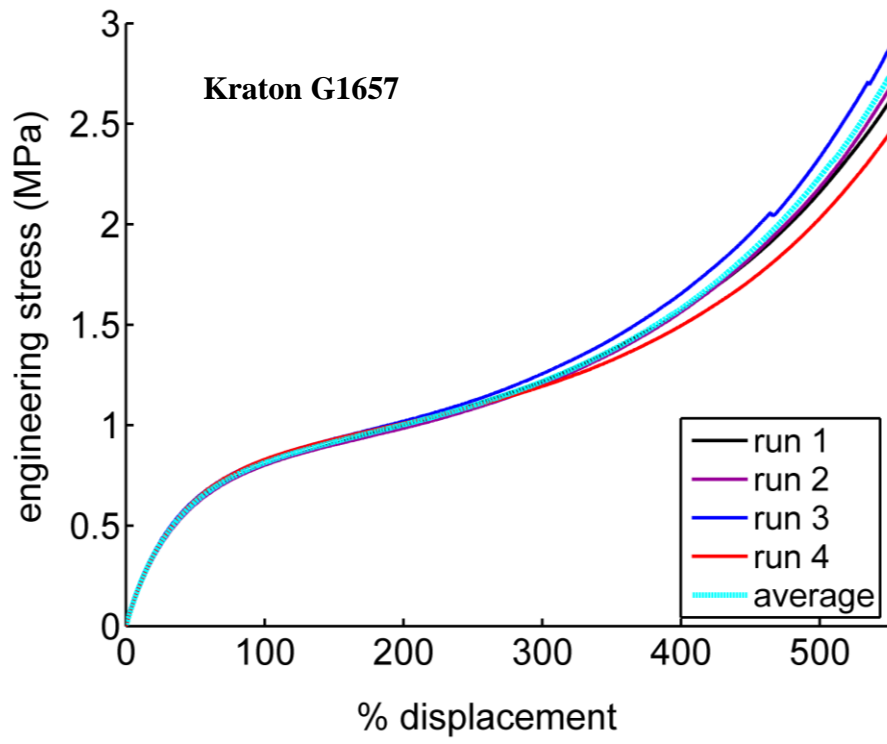
#### 2.4.2 *Uniaxial Elongation Tests*

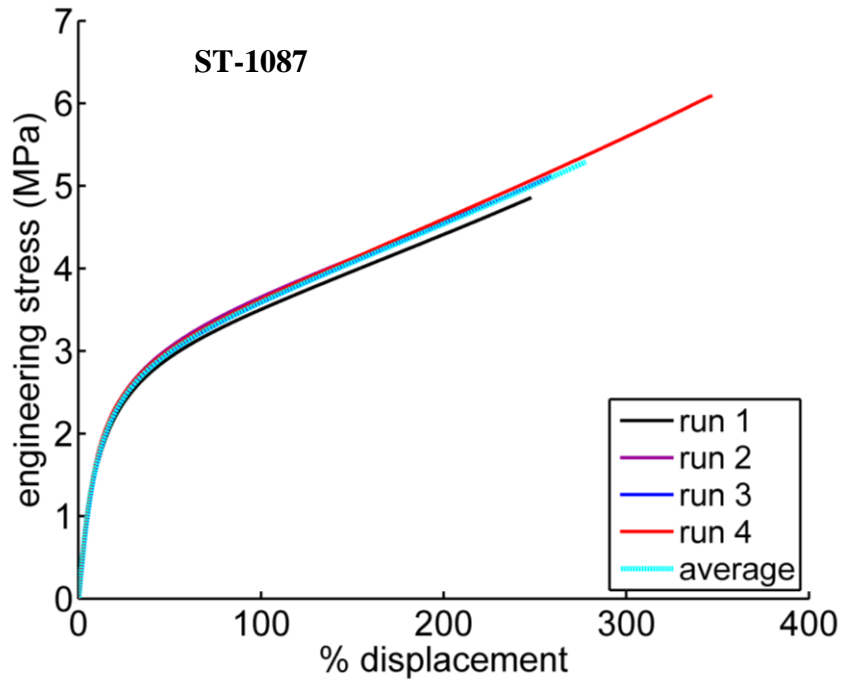
Using the Instron test setup described in Figure 2.1, the stress-strain data for each material was determined from a simple tensile elongation until fracture test while recording load measurements. The test was performed at a relatively slow elongation, 50 mm/min, to isolate non-linear elastic effects from time-dependent properties. Each test was repeated four times to create a statistical average and standard deviation. Figure 2.9 shows the averaged stress-strain data for the four materials examined, compared with commonly used linear elastic modulus assumptions [58-60]. As each sample was tested until fracture, the length of data available was different for all three materials. Note, the expected elongation at break for ST-1060 was 590% [59]. The early failure at 200% observed in Figure 2.9 may be due to small air bubbles in the sample or slight nicks along the edges from cutting. All polymers tested demonstrate a significant nonlinear stress-strain response even at low elongations, illustrating the need for a more complex material model than a simple linear elastic Young's modulus.



**Figure 2.9: Experimental stress-strain diagram; average of 4 tests for 3 materials**

Figure 2.10 shows the individual trials for each material giving good repeatability.

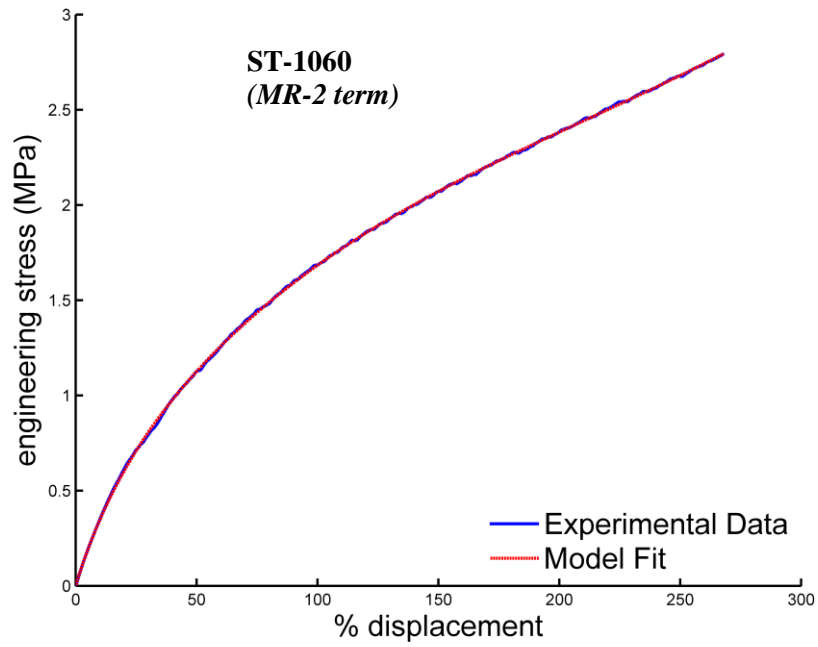
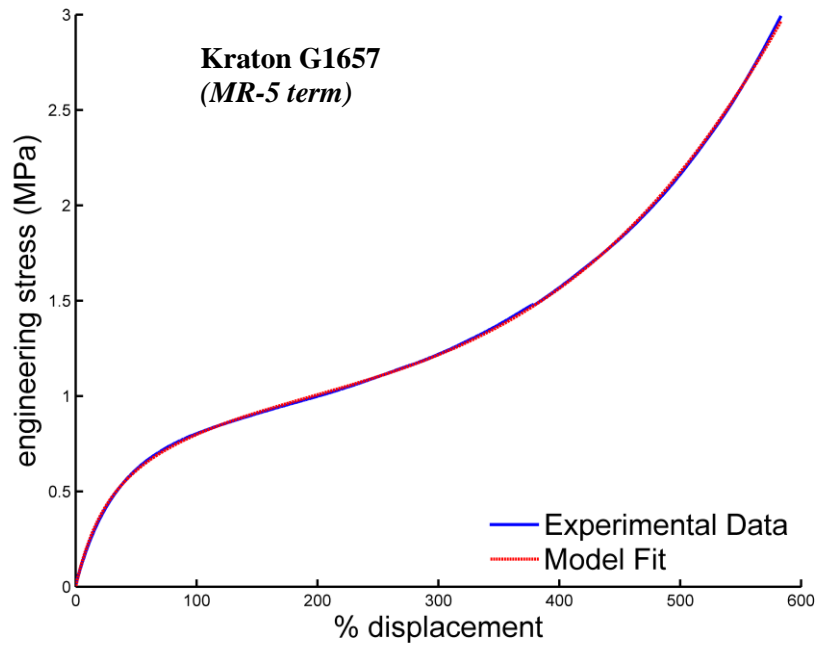




**Figure 2.10: Experimental stress-strain diagrams individual trials and averages. Kraton G1657 and ST-1087 fit with MR-5 term (equation 21) and ST-1060 fit with MR-2 term (equation 18). The jagged line at higher elongations was the result of small slippage within the clamps.**

### 2.4.3 *Model Fit*

A non-linear solver algorithm, developed with MATLAB (see Appendix B) was used to fit the stress-strain data to the Mooney Rivlin material models developed in the previous section. For the higher order model used, convergence was extremely dependent on initial conditions and some multiplicity of solutions can be found which may cause issues for certain loading conditions [62]. The model fit, plotted from the stress calculated in equation 18 and 21 are compared to the experimental stress-strain average in Figure 2.11.



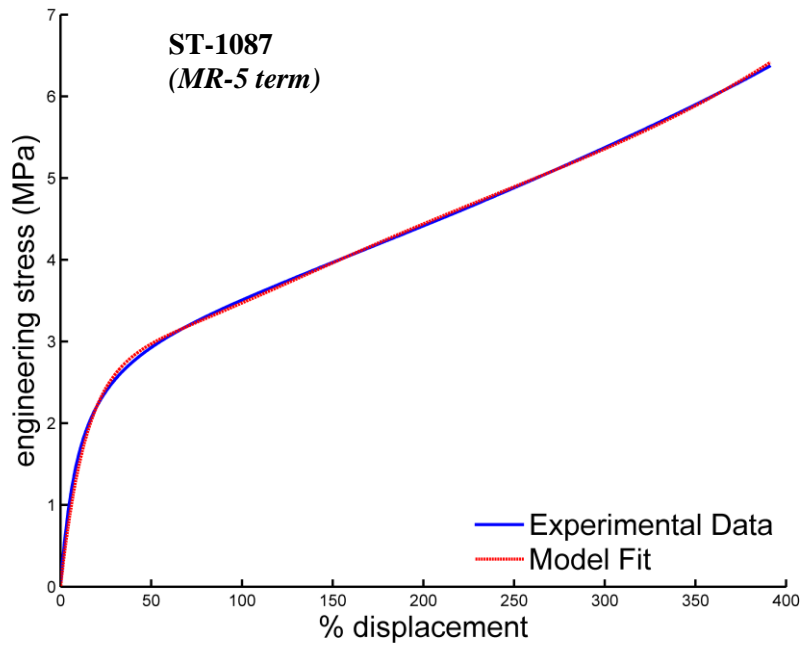


**Figure 2.11: Mooney-Rivlin fit curves compared to experimental data.**

To further verify the accuracy of the Mooney Rivlin parameter fits determined, an FEA simulation of the Instron uniaxial test was performed using the fitted Mooney Rivlin parameters as a material model. A two dimension model was implemented in COMSOL Multiphysics 4.3 using the boundary conditions described in Figure 2.12.

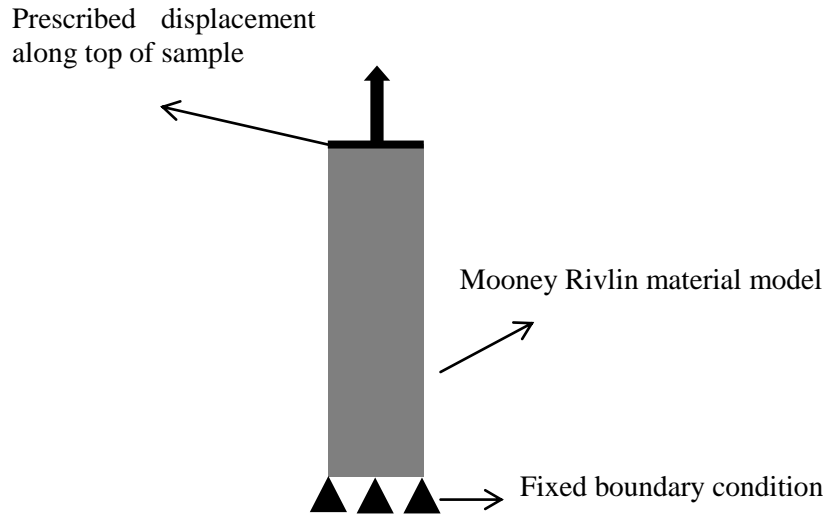


**Figure 2.12: FEA boundary conditions simulating uniaxial elongation Instron test.**

While analytically the compressibility term in equation 1,  $\left[\frac{1}{2}k(J - 1)^2\right]$  can be eliminated as  $J = 1$  for an incompressible material, COMSOL does not allow the distinction between incompressible and compressible materials explicitly. Instead, the bulk modulus,  $k$ , needs to be sufficiently large to approximate an incompressible material. As extremely large values of  $k$  can lead to numerical instabilities, the lowest value of  $k$  which converges to a solution (and in this case to the experimental results) was chosen, see Figure 2.13.

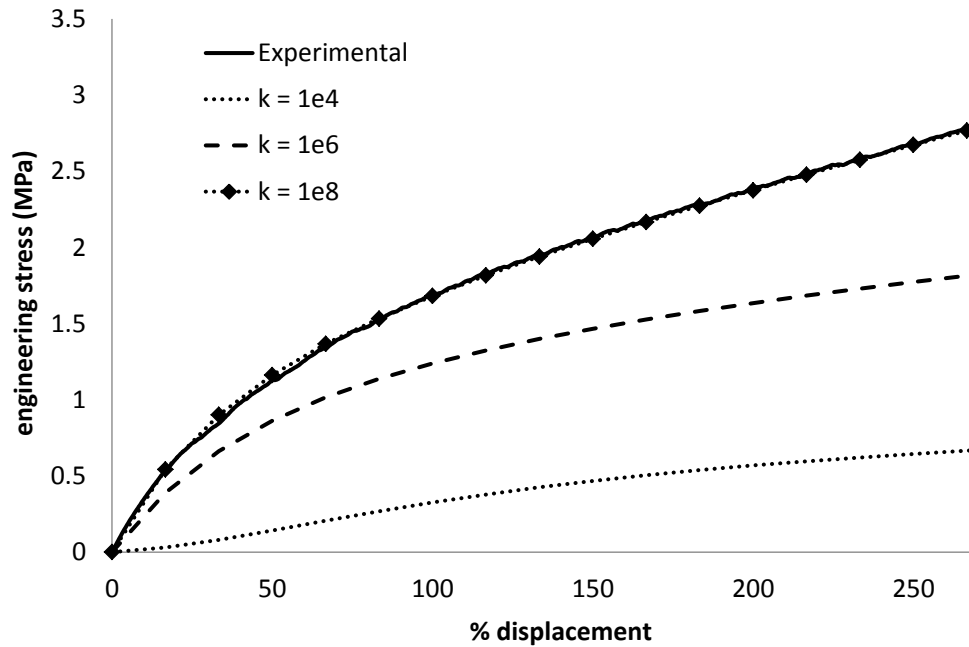


**Figure 2.13: FEA force vs. elongation results for ST-1060 rectangular test sample with varying bulk modulus  $k$ . Increasing  $k$  values show convergence to a solution, which also corresponds to the experimental results found.**

Using fit parameters given in Table 2-2, all materials show good agreement with experimental Instron results for the range of elongations the polymer can be used before fracture, Figure 2.14. This provides an improved simulation method from linear elastic data provided by the supplier. All three polymers show a different response, with Kraton demonstrating a distinct softening at ~100% elongation and stiffening at ~400% elongation. ST-1087 has a much more distinct change in stiffness at ~40% elongation while ST-1060 has a much more gradual change in modulus with elongation.

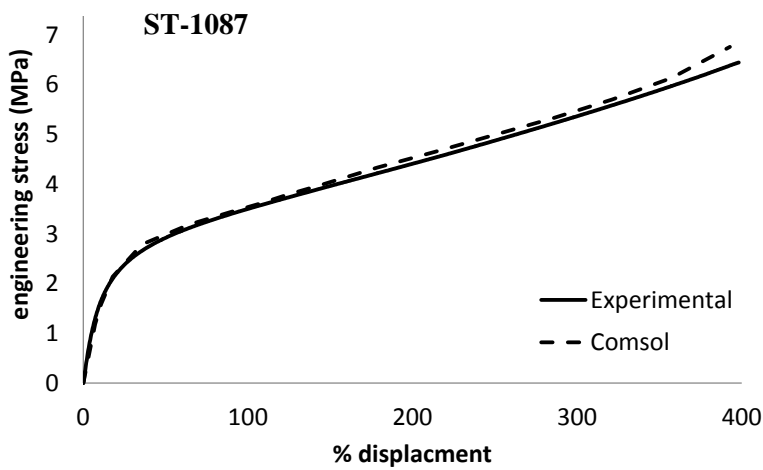
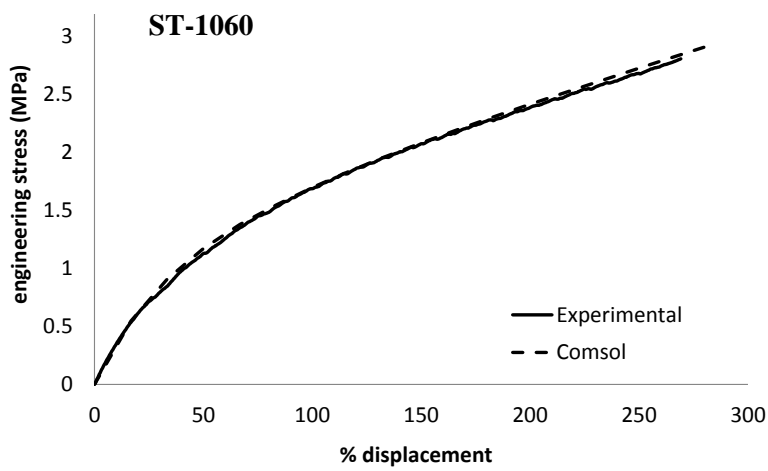
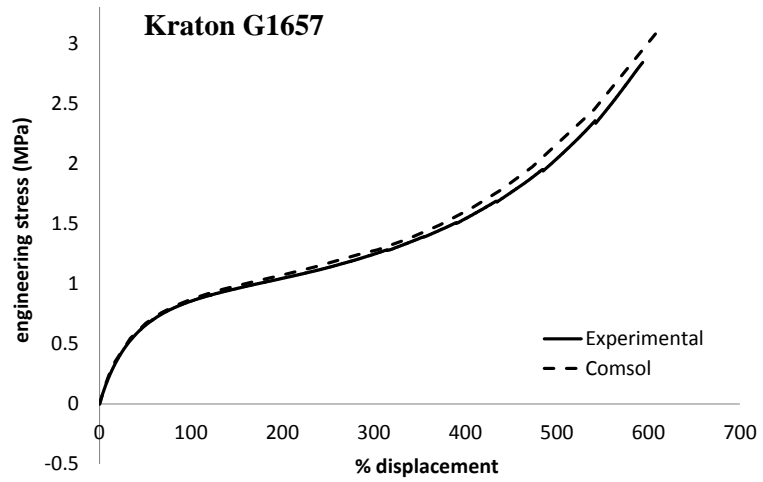


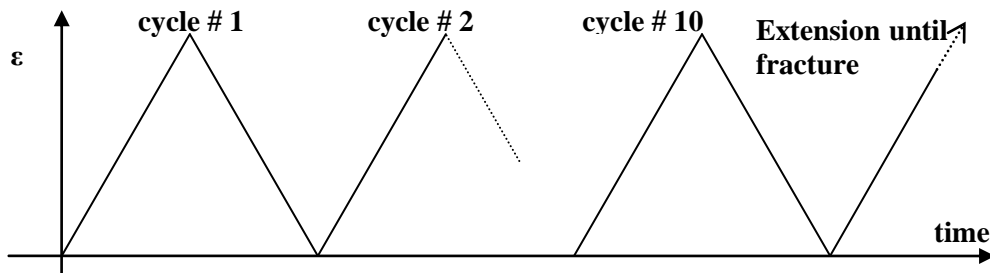
**Figure 2.14: Stress-strain behavior for test materials and Mooney Rivlin parameter verification using COMSOL.**

**Table 2-2: Mooney Rivlin fit parameters (bulk modulus,  $k = 1e8$  Pa for all cases), Kraton G1657 and ST-1087 use a 5 term Mooney Rivlin fit while ST-1060 fits well with a 2 term model. Negative values required for fit but may cause instabilities for some loading conditions.**

Material	$C_1$ (kPa)	$C_2$ (kPa)	$C_3$ (kPa)	$C_4$ (kPa)	$C_5$ (kPa)
<i>Kraton G1657</i>	-69.5	532	3.49	58.8	-17.5
<i>ST-1060</i>	282	393	0	0	0
<i>ST-1087</i>	-5960	9420	24.2	2040	-183

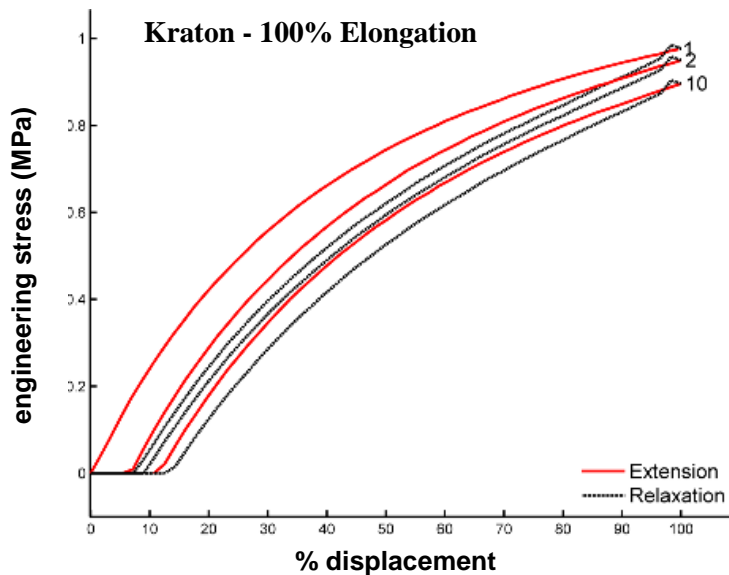
## 2.5 Plasticity

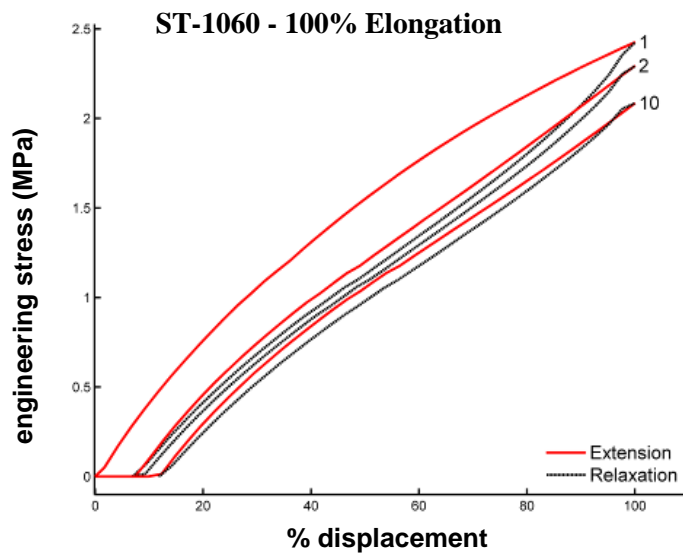
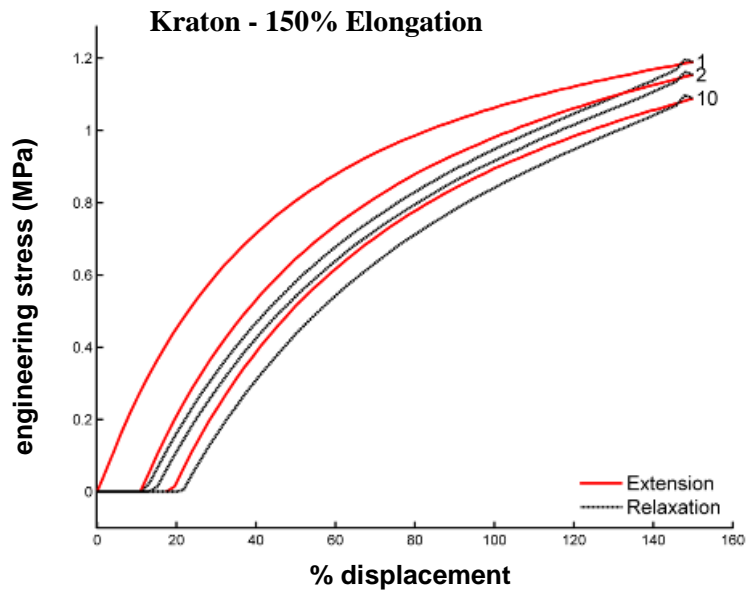
The previous section only examined non-linear elastic properties of the polymers. If the material will be loaded to significant elongations repetitively, plasticity will also need to be considered. To determine the extent of damage undergone by each polymer, a repetitive loading cycle, illustrated in Figure 2.15, was conducted for 10 cycles, followed by a full elongation until fracture. The test was conducted based on ASTM standard D7791-12 12 (Standard Test Method for Uniaxial Fatigue Properties of Plastics) [67], with each elongation cycle at 100% and 150% of the gauge length using 50 mm/min strain rates to minimize viscoelastic effects.

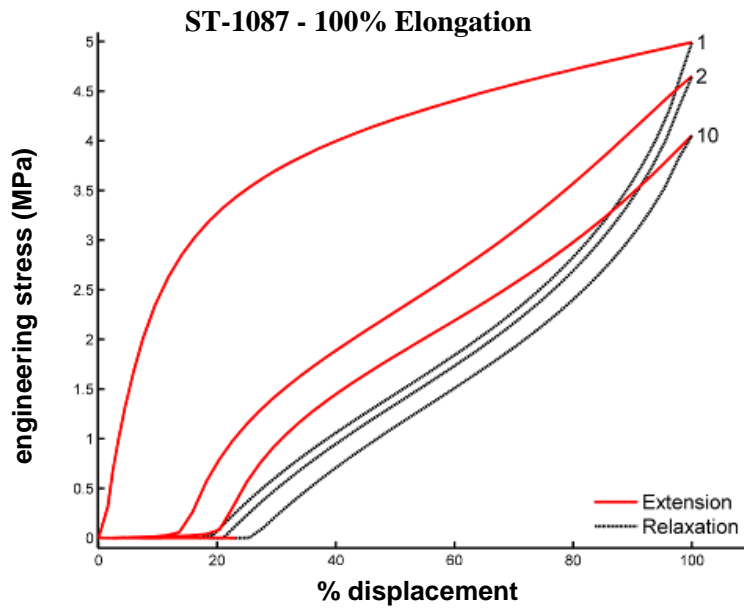
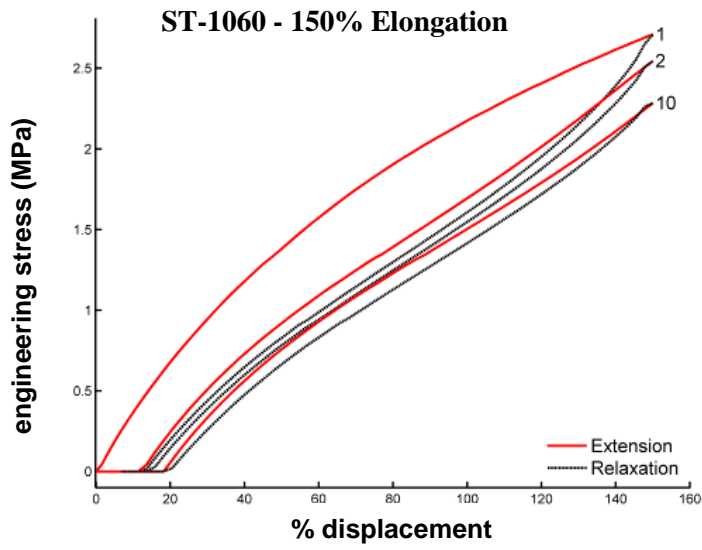


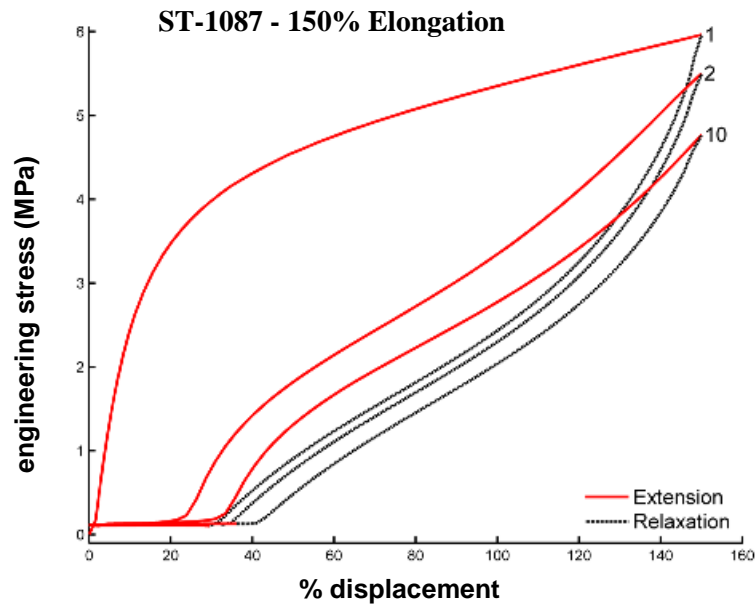
**Figure 2.15: Instron loading diagram for plasticity testing, repeated for 10 cycles, followed by a full elongation until fracture.**

Results from the plasticity tests are given in Figure 2.16. All samples show a softening effect after each cycle due to breaking bonds in the polymer chains. This softening was most dramatic for the first cycle and decreases for consecutive extensions. Hysteresis was also evident as the extension curve always lies above the relaxation curve. This effect was due to heat generation during extension, causing more energy for elongation than relaxation [68] As these materials elongate several hundred percent without fracture, it was important to be aware of the changes to the stress-strain curve which may occur after the first cycle of use. ST-1087 shows the largest softening from the pristine material to a cycled material, which could make this polymer less useful in some applications. Kraton and ST-1060 gave similar plasticity effects which is advantageous for durable dry adhesives used in cyclic loading. The softening effect was similar for both elongation values tested but was more pronounced for the higher (150%) elongation for all materials.



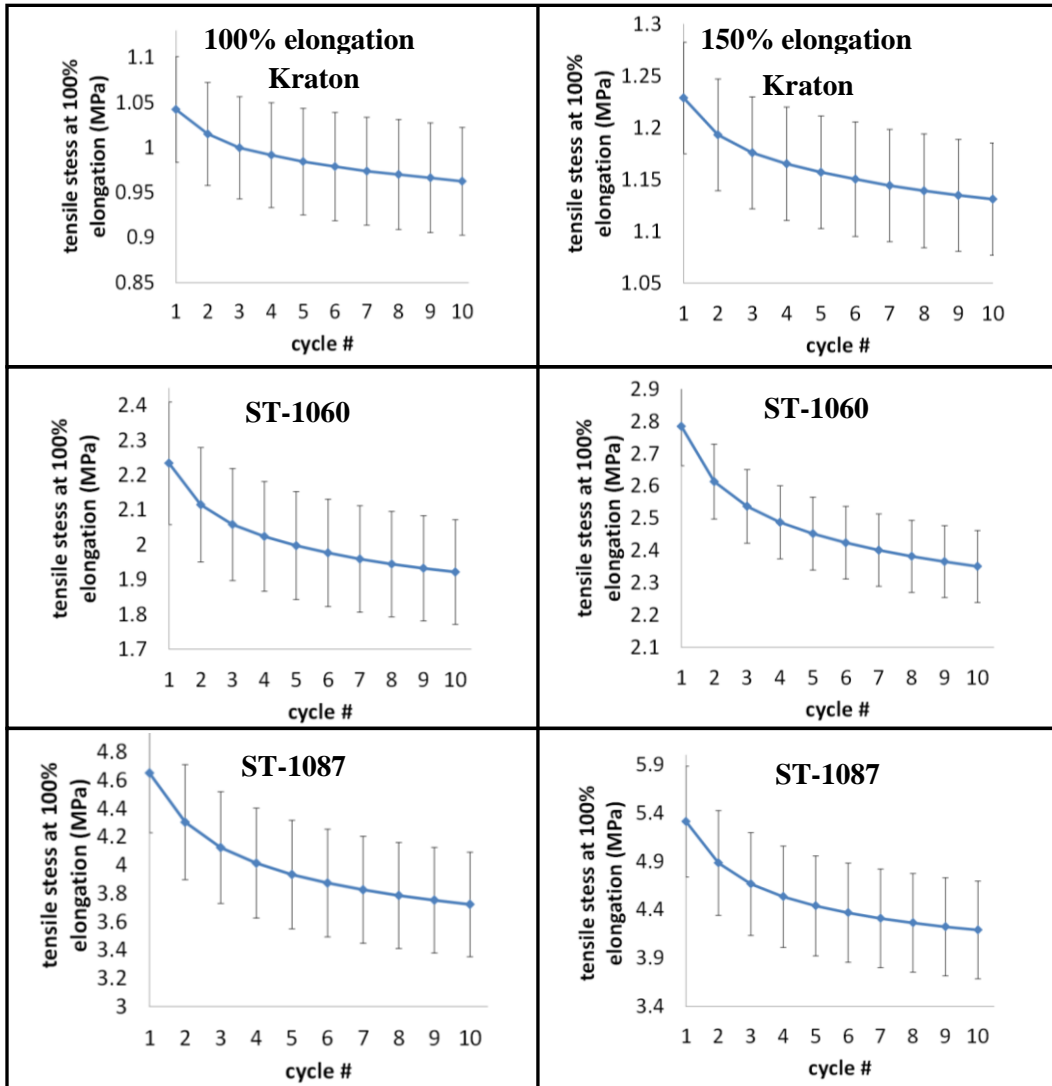






**Figure 2.16: Cycled elongation test to 100% and 150% strain showing hysteresis and plastic deformation; showing cycles 1, 2, and 10.**

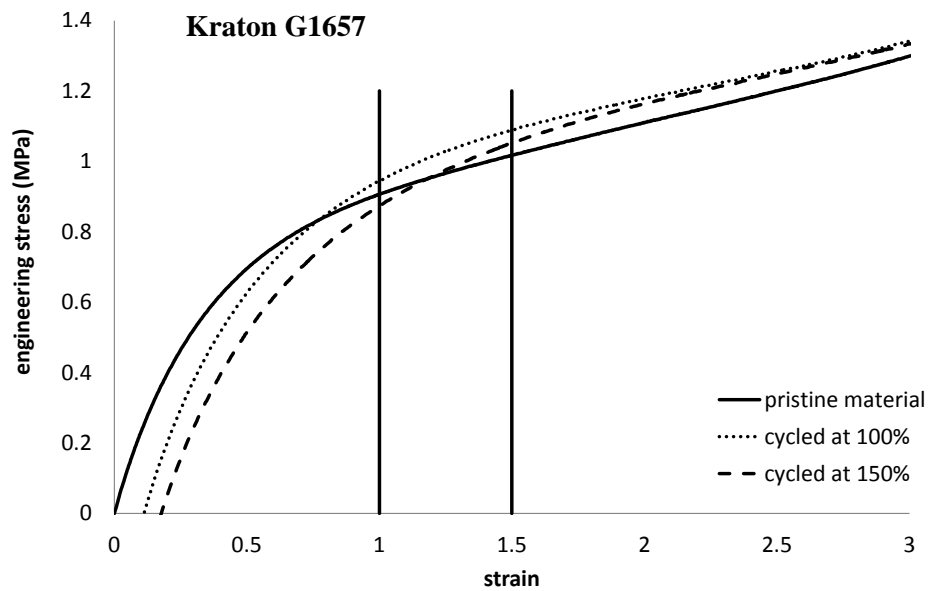
The material yield resulting from the consecutive 100% and 150% sample elongation is illustrated in Figure 2.17 by plotting the decrease in stress value at each cycle. Note the axis scale is zoomed into the area of interest, making the seemingly large error bars more significant. All three materials demonstrate a softening effect which becomes almost negligible after ten cycles. These results also show more yield in the polyurethanes after one cycle then for the Kraton.



**Figure 2.17: Maximum tensile stress at 100% and 150% elongation vs. cycle number.**

The effect of pre-cycling the material to 100% and 150% was further examined by comparing to the pristine sample stress-strain with cycled curves, see Figure 2.18. Polymers tested demonstrated the general trend of the Mullins effect (softening in the pre-strained elongation range while converging back to the pristine material behaviour when reaching new maximum elongations for the

sample [69]). Some inconsistencies exist in the data due to variability in the sample. However, in the pre-strained elongation range, each polymer shows progressively softer results for higher elongation pre-cycling. This effect was important to consider as it impacts the accuracy of the finite element simulation based on the pristine material behaviour. To make the model more accurate, the softened curves could be re-fit to the Mooney-Rivlin equation, however, the elongation of the dry adhesive fiber would have to be known.



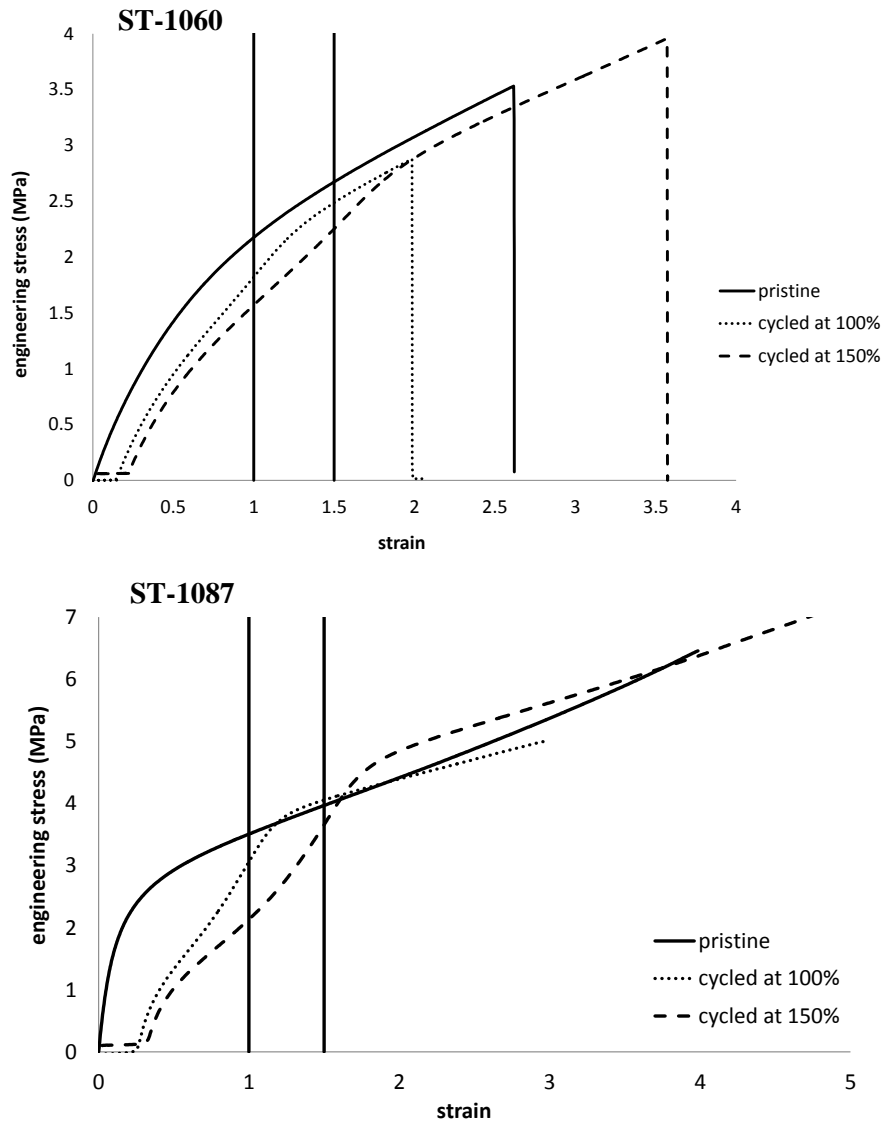


**Figure 2.18: Evidence of Mullins effect showing pristine stress-strain curve overlaid with material data from cycled polymer (vertical lines at 1 and 1.5 strain for clarity).**

Yield properties were further tested by manually extending the Instron with a fine control dial by 2 mm increments and relaxing until zero tensile force was measured; occurring at the original gauge length plus yield damage.

Elongations were performed at ~20 mm/min and the stress was allowed to stabilize for 30 seconds for each trial, described in Figure 2.19.

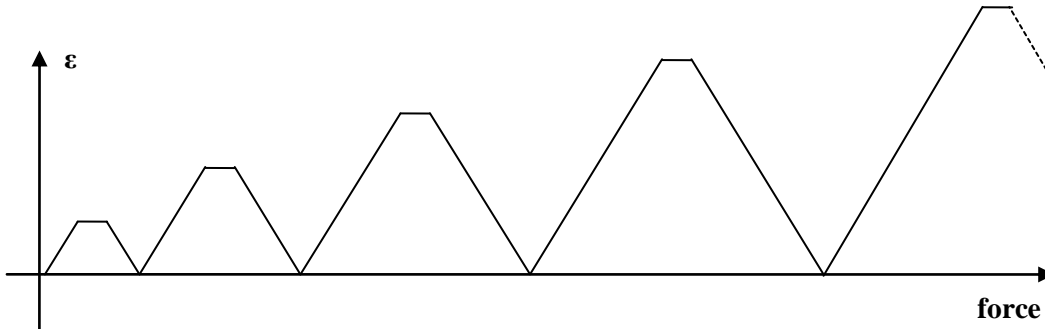


**Figure 2.19: Instron loading diagram for yield test, performed manually with each cycle increasing elongation by 2 mm increments until 100% elongation.**

Figure 2.20 shows the percent yield that can be expected for elongations up to 100%. These properties are important to consider when designing tolerances for devices. All materials show relatively linear increase in yield damage for the elongations tested. ST-1087 demonstrated the highest yield at ~18% damage with 100 percent elongation. Kraton G1657 and ST-1060 show ~ 12% damage at 100 percent strain. Each material was tested three times to give an average and standard deviation. The standard deviation of ST-1060 steadily increases at higher elongations, giving less consistent prediction than for the other materials.

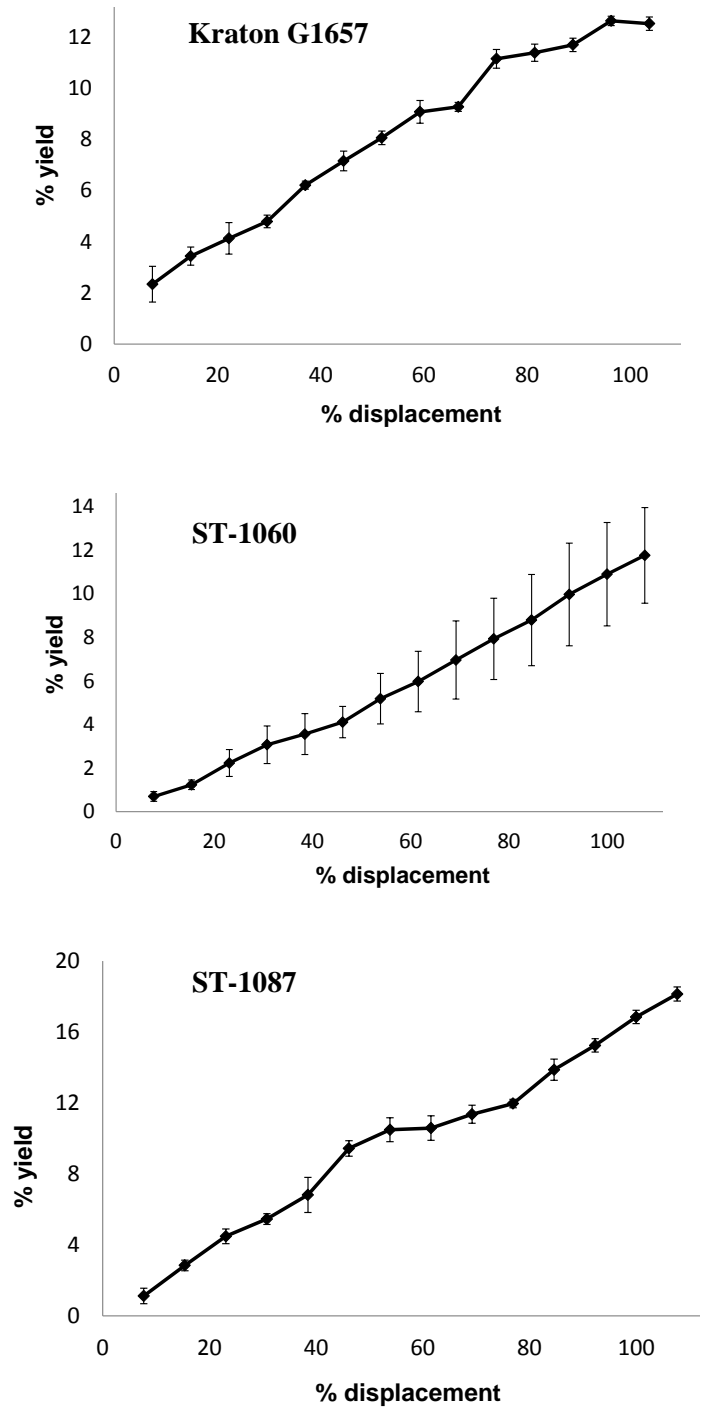


**Figure 2.20: Percent yield vs. percent resulting elongation in each tested material. Each curve represents average and standard deviation of three trials.**

## 2.6 Viscoelasticity

### 2.6.1 Background

While ideal elastomers would exhibit purely elastic behavior, rubber materials generally show some degree of viscoelasticity [70]. Although the impact of the material viscoelasticity will depend on the end use of the adhesive and the cycle time of detachment, understanding the material properties allows a more complete analysis for fiber design.

Modeling purely elastic viscous materials has been well described in literature. A combined non-linear viscous constitutive behavior model is however much more difficult to achieve and produces less robust results [71]. To allow implementation in standard FEA packages, the non-linear and viscous effects are modeled separately in this work. Using viscoelastic data from experimental data at approximately equal elongations in COMSOL allows for a relatively good comparison with experimental tests using a linear Young's modulus estimate. This gives guidelines for the viscoelasticity of the material and at which pull off speeds this effect should be considered.

A generalized Maxwell model, previously shown to provide good fit with PDMS [72,73], was used to fit three time constants describing the material behavior. Three time constants were used as this was the minimum number of parameters to accurately model the experimental data. All materials showed some viscous flow which occurs when the material was held at a high strain for an

extended time [70]. This effect was not included in the time constant calculation. The Maxwell model simulates the viscoelastic effect by the combination of a spring and dashpot in series, see Figure 2.21. Multiple branches of spring/dashpots can be added to improve the fit, each representing a time constant and corresponding stiffness.

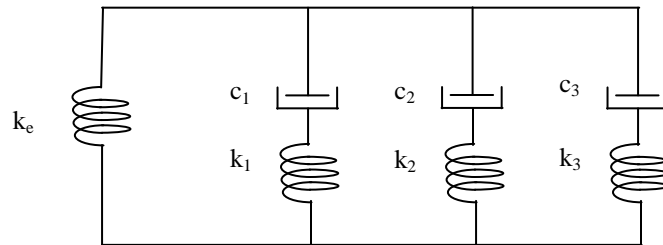


**Figure 2.21: Three-branch Maxwell model used to simulate linear viscoelasticity of the polymers. Stiffness modeled by  $k$  and damping with  $c$  ( $k_e$  represents steady state material stiffness).**

To simplify the model in Figure 2.21, a single branch consisting of a spring and damper was first considered. The damping portion of the model is ‘ $c$ ’ and the stiffness of the material is defined as ‘ $k$ ’.

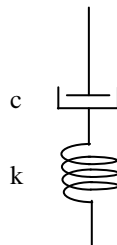


**Figure 2.22: Single branch of the Maxwell model.**

In Figure 2.22, taking the spring,  $k$ , and damper  $c$ , in series by summing the displacement in each component gives the Maxwell differential equation [70] for the combined response in equation 22.

$$\dot{\varepsilon} = \frac{1}{k}\dot{\sigma} + \frac{1}{c}\sigma \quad (22)$$

Where  $\dot{\varepsilon}$  is the material strain rate,  $\dot{\sigma}$  is the stress rate. By separating  $\dot{\sigma}$  and integrating we can solve for the stress response as a function of time as described in the following (part of this derivation is reproduced from [70]):

$$\frac{d\varepsilon}{dt} = \frac{1}{k}\frac{d\sigma}{dt} + \frac{1}{c}\sigma \quad (23)$$

As a stress relaxation experiment will be performed, followed by the initial impulse loading, the strain rate will be zero, giving:

$$0 = \frac{1}{k}\frac{d\sigma}{dt} + \frac{1}{c}\sigma \quad (24)$$

Separating  $d\sigma$  and  $dt$  gives:

$$\frac{d\sigma}{\sigma} = -\frac{k}{c}dt \quad (25)$$

Defining the time constant of the system as:

$$\tau = \frac{c}{k} \quad (26)$$

We can write equation 25 as:

$$\frac{d\sigma}{\sigma} = -\frac{1}{\tau} dt \quad (27)$$

Integrating both sides gives:

$$\int_{\sigma_0}^{\sigma} \frac{d\sigma}{\sigma} = -\frac{1}{\tau} \int_0^t dt \quad (28)$$

Where  $\sigma_0$  is the initial stress, right after the impulse loading; giving the result:

$$\ln(\sigma) - \ln(\sigma_0) = -\frac{t}{\tau} \quad (29)$$

Rearranging and raising to the exponential power gives:

$$\exp[\ln(\sigma)] = \exp\left[\ln(\sigma_0) - \frac{t}{\tau}\right] \quad (30)$$

Which when evaluated gives stress response as a function of time:

$$\sigma(t) = \sigma_0 \exp(-t/\tau) \quad (31)$$

Equation 31 can then be generalized to multiple branches of the Maxwell model by adding the response in series. For the model described in Figure 2.21, we get:

$$\begin{aligned}\sigma(t) = & \sigma_{elastic} + \sigma_1 \exp(-t/\tau_1) + \sigma_2 \exp(-t/\tau_2) \\ & + \sigma_3 \exp(-t/\tau_3)\end{aligned}\quad (32)$$

Where  $\sigma_i$  represent the portion of the total stress which is decreasing at the corresponding time constant. As COMSOL requires an input of shear modulus, we can re-write equation 32 in terms of stiffness and strain using the simple Hooke's law:

$$\sigma = E\varepsilon \quad (33)$$

Giving:

$$\begin{aligned}\sigma(t) = & E_{elastic}\varepsilon_{test} + E_1\varepsilon_{test} \exp(-t/\tau_1) \\ & + E_2\varepsilon_{test} \exp(-t/\tau_2) + E_3\varepsilon_{test} \exp(-t/\tau_3)\end{aligned}\quad (34)$$

Where  $\varepsilon_{test}$  is the strain at which the constant strain test was performed. A Matlab non-linear least squares fit algorithm, see Appendix B, was used to fit  $E_{elastic}$ ,  $E_1$ ,  $E_2$ ,  $E_3$ ,  $\tau_1$ ,  $\tau_2$ ,  $\tau_3$  to experimental stress relaxation data with equation 34.

The model inputs for COMSOL's Maxwell equation input require '*Shear Modulus*' and '*Relaxation Time*.' The relaxation time corresponds directly to the time constant  $\tau_i$  determined. The shear modulus can be found by assuming linear elastic behavior or a small strain approximation giving:

$$G = \frac{E}{2(1 + \nu)} \quad (35)$$

Where  $\nu$  is the Poisson's ratio, equal to  $\sim 0.5$  for most rubber materials [74], allowing us to directly approximate the shear modulus as a function of the fitted elastic modulus as:

$$G = \frac{E}{3} \quad (36)$$

Results in this work are given for elastic modulus and relaxation time.

### 2.6.2 Results

To determine the constants from the Maxwell model, stress relaxation test was performed with the Instron setup described in Figure 2.1 according to ASTM Standard D2990-09 (Standard Test Method for Tensile, Compressive, and Flexural Creep and Creep-Rupture of Plastics) [75]. The polymer sample was extended 100 and 150 percent of its gauge length at 2500 mm/min (maximum elongation rate for the Instron) and held for 5 minutes while recording the decrease in the load cell measurement. Using a Matlab non-linear solver algorithm, the three time constants,  $\tau_i$ , and corresponding shear modulus,  $E_i$ , were calculated; see Figure 2.3 for a full summary of viscoelastic properties.

As shown in Figure 2.23, the experimental results fit well with the overlaid model fits. These parameters can be implemented in a FEA package. Comparing the time constants and corresponding stiffness can also help determine if a specific application will be subject to significant viscoelastic effects.

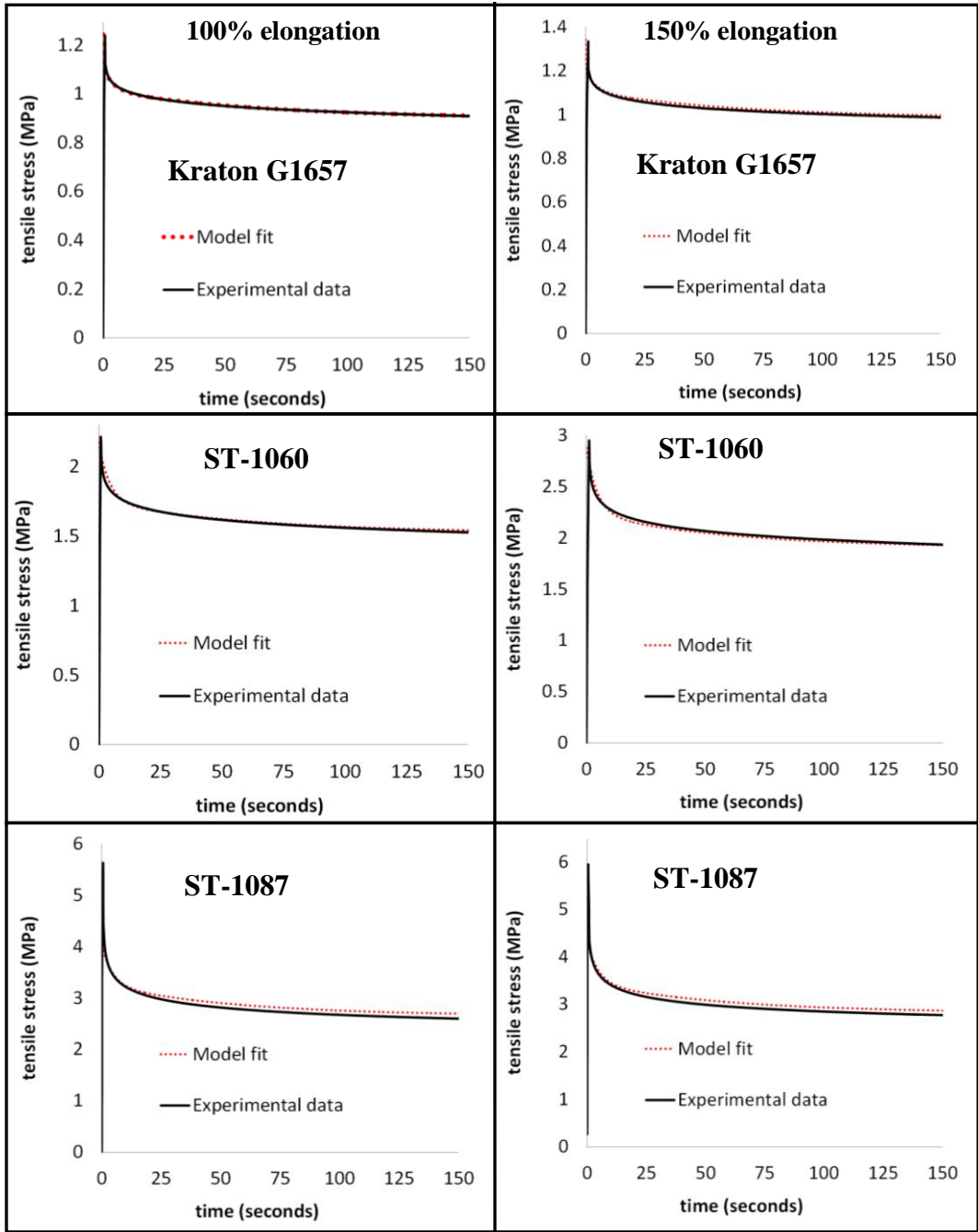


**Figure 2.23: Relaxation tests at 100% on the left and 150% elongation on the right with 3 time constant curve fit for the three materials examined.**

The Generalized Maxwell viscoelastic data fits are provided in Table 2-3. As highly non-linear hyperelastic model fits often produced multiplicity of results (different combinations of parameters which can all fit the experimental data), the average of four experimental data sets was used to fit Mooney Rivlin constants.

**Table 2-3: Summary of Kraton G1657, ST-1060, and ST-1060 material properties tested for viscoelastic models.**

Test Method	Parameter	Kraton G1657	ST-1060	ST-1087
<b>Relaxation (100%)</b>	$\tau_1(sec)$	$0.02 \pm 0.04$	$0.36 \pm 0.01$	$0.17 \pm 0.01$
	$\tau_2(sec)$	$4.1 \pm 0.13$	$5.5 \pm 0.05$	$4.5 \pm 0.04$
	$\tau_3(sec)$	$64.2 \pm 1.5$	$64.2 \pm 1.4$	$57.3 \pm 0.32$
	$E_1(MPa)$	$0.14 \pm 0.01$	$0.25 \pm 0.02$	$1.5 \pm 0.06$
	$E_2(MPa)$	$0.10 \pm 0.01$	$0.19 \pm 0.01$	$0.78 \pm 0.03$
	$E_3(MPa)$	$0.12 \pm 0.005$	$0.23 \pm 0.02$	$0.60 \pm 0.04$
	$E_o(MPa)$	$0.95 \pm 0.05$	$1.6 \pm 0.16$	$2.7 \pm 0.16$
<b>Relaxation (150%)</b>	$\tau_1(sec)$	$0.067 \pm 0.003$	$0.39 \pm 0.03$	$0.21 \pm 0.01$
	$\tau_2(sec)$	$4.5 \pm 0.13$	$5.5 \pm 0.25$	$4.7 \pm 0.07$
	$\tau_3(sec)$	$65.3 \pm 0.83$	$63.2 \pm 0.28$	$57.7 \pm 0.1$
	$E_1(MPa)$	$0.09 \pm 0.007$	$0.24 \pm 0.02$	$1.0 \pm 0.04$
	$E_2(MPa)$	$0.06 \pm 0.004$	$0.18 \pm 0.02$	$0.57 \pm 0.02$
	$E_3(MPa)$	$0.08 \pm 0.006$	$0.22 \pm 0.03$	$0.42 \pm 0.01$
	$E_o(MPa)$	$0.63 \pm 0.04$	$1.2 \pm 0.1$	$1.9 \pm 0.09$

Having a good understanding of the bulk polymer mechanical behavior allows for more accurate simulations and provides design guidelines important for future adhesive iterations. Important findings from this chapter were the significant non-linearity which was fitted accurately to a Mooney Rivlin material model and the large plastic deformations in all polymers. To prevent fibers from yielding in the first cycle, designs should be made to limit the maximum elongation, thus making a more durable adhesive. These findings are incorporated in a finite element simulation of dry adhesive fibers in the next chapter.

## 3 FIBER SIMULATION

### 3.1 Introduction

To optimize future dry adhesive pillar designs and provide guidelines for target geometries when manufacturing, a simulation which extends beyond linear elastic is critical. Adhesives in this work show significant elongation (several hundred percent), which, from material testing in chapter 2, is known to be well into the non-linear range. While currently only fixed and roller boundary condition models are available in literature, this work investigated the effect of fiber stresses which result from the different models and introduce a new frictional interface simulation. These adhesives are known to demonstrate frictional cap shrinkage, while maintaining adhesion and supporting shear, suggesting a frictional interface may be required (Figure 3.1). The material testing also demonstrated that the polymers commonly used for dry adhesives can be subject to significant time dependent stress-strain responses. This chapter incorporates the Mooney Rivlin hyperelastic and Maxwell model viscoelastic fits developed in chapter 2 for single fiber finite element simulation<sup>2</sup>. A report for each model, summarizing all properties and the model setup printed with COMSOL is included in Appendix C.

---

<sup>2</sup> An adaption of portions from this chapter were presented at the 2012 Hilton Head Solid-State Sensors, Actuators, and Microsystems Workshop in Hilton Head South Carolina [76] and the 2013 Adhesion Society Conference in Daytona Beach Florida [77].

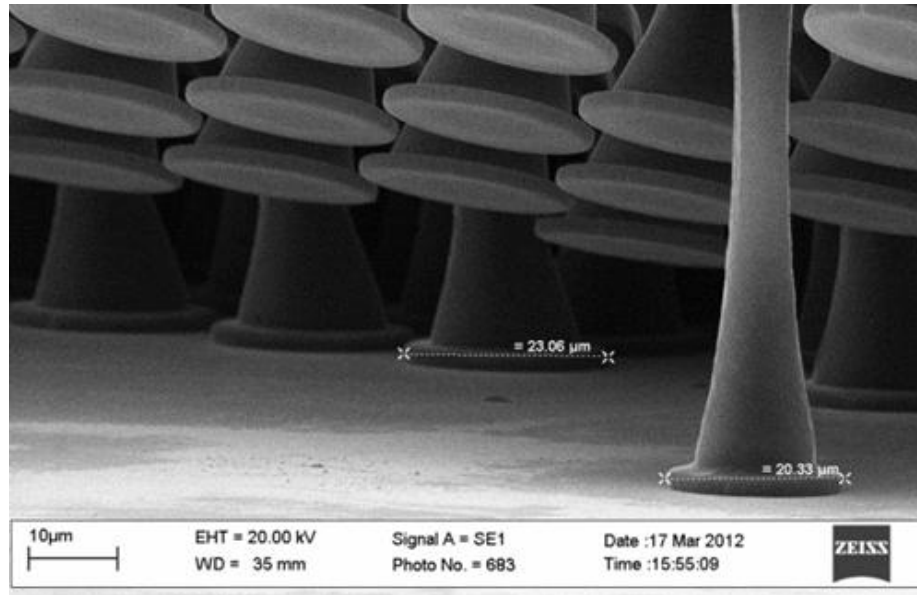


**Figure 3.1: 24  $\mu\text{m}$  diameter ST-1060 fibers attached to silicon die in SEM showing cap shrinkage during elongation (Fibers fabricated and SEM image taken by Brendan Ferguson). Reprinted with permission from [19]. Copyright (2013) Ferguson.**

The finite element model was created using COMSOL 4.3b (4.3.2.189). To implement the Mooney Rivlin function in COMOSL, the “*User Defined*” stain energy density function needs to be used as it was determined there is an error in the COMSOL code for the built in function. Three different boundary conditions (BCs) were examined to determine the modeling technique of the adhesion interface between the fiber cap and the adhesion substrate which will most accurately simulate the adhesion phenomenon. The fixed cap BC used a fixed constraint on all nodes of the top surface of the fiber cap. A roller BC used a roller constraint on the top surfaces of the cap, allowing unconstrained cap shrinkage while restricting any displacement in the axial direction. A novel third BC, not

previously explored in literature, uses a frictional constraint allowing constrained shrinkage of the fiber cap depending on the friction coefficient used.

The model developed can be used as a valuable design tool for dry adhesives. Among some possible applications, the simulation can determine the maximum elongation in fiber geometry, allowing designs to be altered to limit the yield which will occur in the polymer after use and the stress distribution along the top cap, ultimately affecting the adhesion force. In addition, the simulation can be used to optimize other aspects of dry adhesives of interest for future work in our lab such as anisotropic fibers (utilizing defects in the top surface to initiate high stress concentration in on peel direction) [78].

### 3.2 Model Setup

Geometries were imported into COMSOL from Solidworks models of fibers (see Figure 3.2) fabricated in this work (chapter 4). To save computational time, all pure axial simulations were modeled with at 2-dimensional axis symmetric simplification. Shear forces were simulated using a full 3-dimensional model.

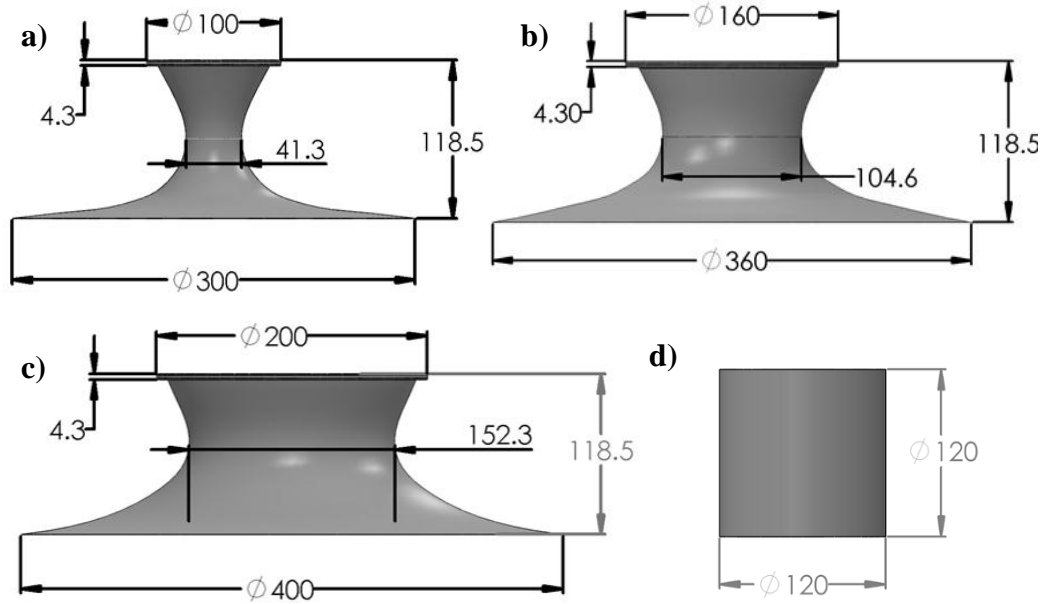


**Figure 3.2: Solidworks models of four main fibers chosen for simulation. Dimensions determined from scanning electron microscope images of fabricated fibers: a) 100  $\mu\text{m}$  diameter fiber, b) 160  $\mu\text{m}$  diameter fiber, c) 200  $\mu\text{m}$  diameter fiber, d) 120  $\mu\text{m}$  diameter vertical walled post,**

After importing fiber geometries into COMSOL (.dxf file for 2-D fibers and .x\_t file 3-D fibers), a solid block was added to the base to model the fiber backing material. These elements were joined into one feature to have the same material properties and no relative displacements. A pressure or displacement was applied at the base of the backing material while three different boundary conditions are chosen for the fiber cap (fixed, roller, or frictional). The roller cap boundary condition requires an extra roller constraint on the edges of the fiber base for numerical stability. This condition does represent the physical system as the base would be infinitely large as compared to the fiber size, therefore no

twisting could occur. The side roller and cap boundary condition does however not allow for any shear simulations. The set up for geometry and boundary conditions used is illustrated in Figure 3.3.

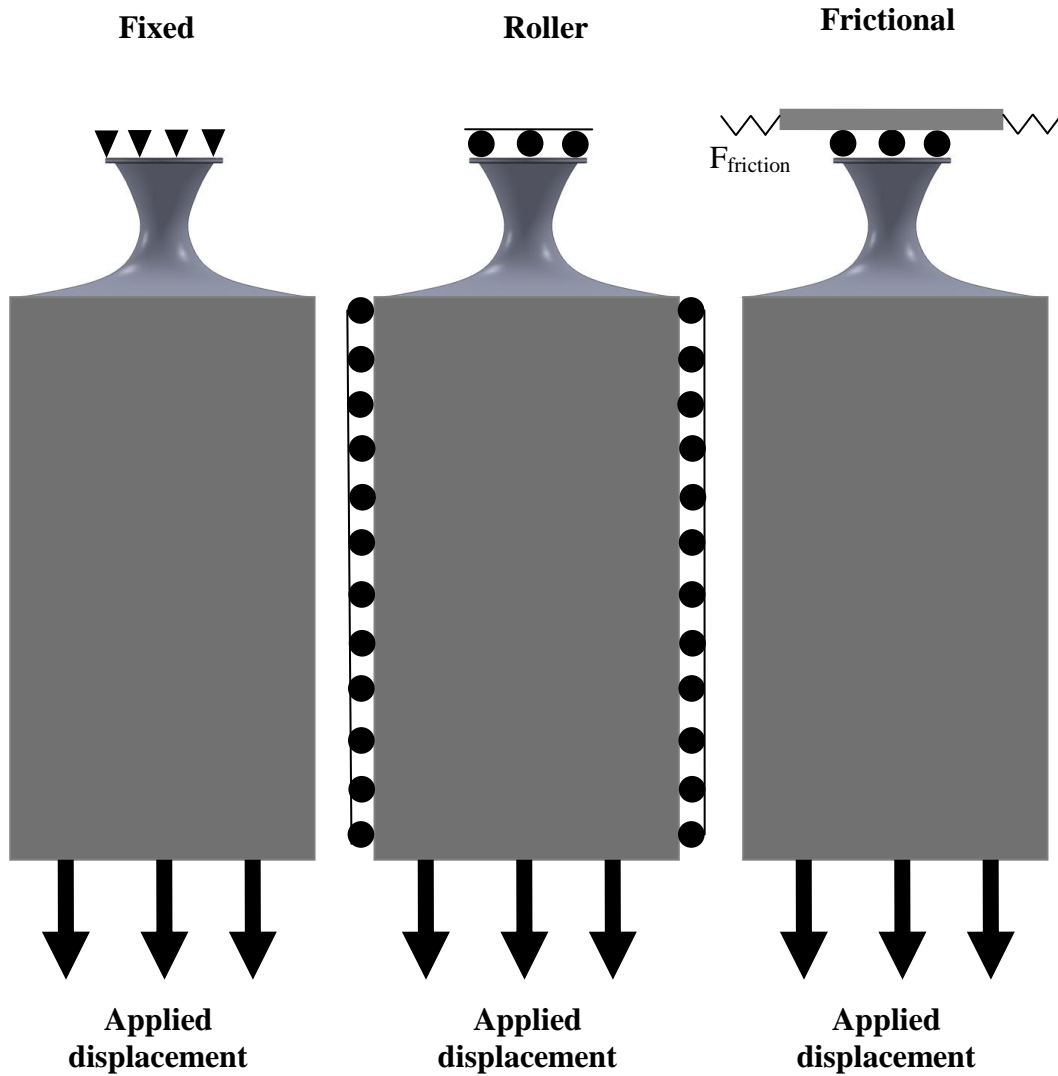
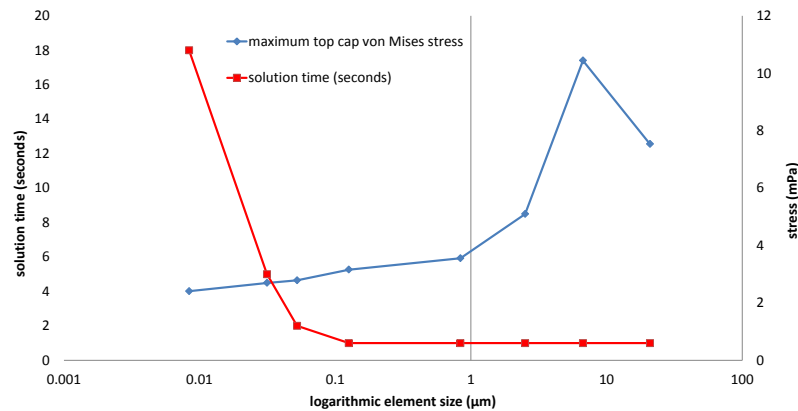


Figure 3.3: FEA boundary conditions and geometry assembly.

### 3.3 Mesh Convergence Study

Two dimensional axis symmetric models were meshed using a physics controlled mesh function in COMSOL with free triangular elements. Three dimensional simulations for shear analysis were meshed using free tetrahedral elements. A mesh convergence study was performed to determine the appropriate element size; giving converged solutions while minimizing solution time Figure 3.4 shows the results for the 2-D convergence study for a 100 $\mu\text{m}$  diameter fiber (Kraton G1657 material) extended axial 500  $\mu\text{m}$ ; a common maximum displacement for this fiber. The maximum von Mises stresses observed on the top cap of the fiber shows a relatively convergence solution at an element size of  $\sim 0.01$  but was still slightly decreasing.



**Figure 3.4: FEA model mesh convergence study (100  $\mu\text{m}$  diameter Kraton G1657 fiber) with a fixed cap BC comparing solution time with the maximum top cap von Mises stresses. Element sizes ranging from 0.01  $\mu\text{m}$  – 20  $\mu\text{m}$  (shown in logarithmic scale).**

As this work will be more concerned with the total normal reaction forces which result from an applied elongation (which can be compared directly to experimental fiber measurements) then the forces at each element, the element size was less crucial. The results (see Figure 3.5) show the total axial reaction force from the applied elongation converges at an element size of  $0.8 \mu\text{m}$ . This can be expected as the reaction force represents an average (integration) over the cross section of the fiber.

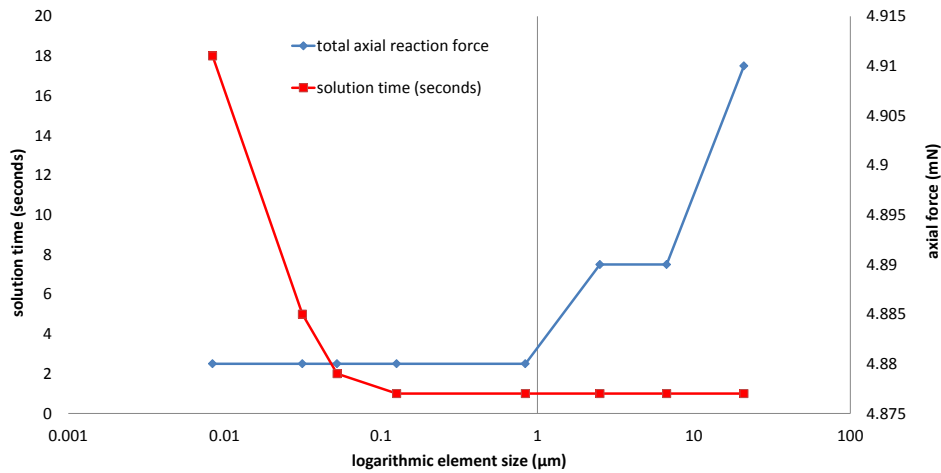


**Figure 3.5: FEA mesh convergence study (100  $\mu\text{m}$  diameter Kraton G1657 fiber) with a fixed cap BC showing axial reaction forces converging at  $0.8 \mu\text{m}$  element size. Element sizes ranging from  $0.01 \mu\text{m}$  –  $20 \mu\text{m}$  (shown in logarithmic scale).**

To further analyze the effect of mesh size, the fiber side view (2-D axis symmetric model with revolution for 3-D view) and top cap view for the largest and smallest element sizes are compared in Figure 3.6. These results show the large element size also has distinctly different top cap stresses.

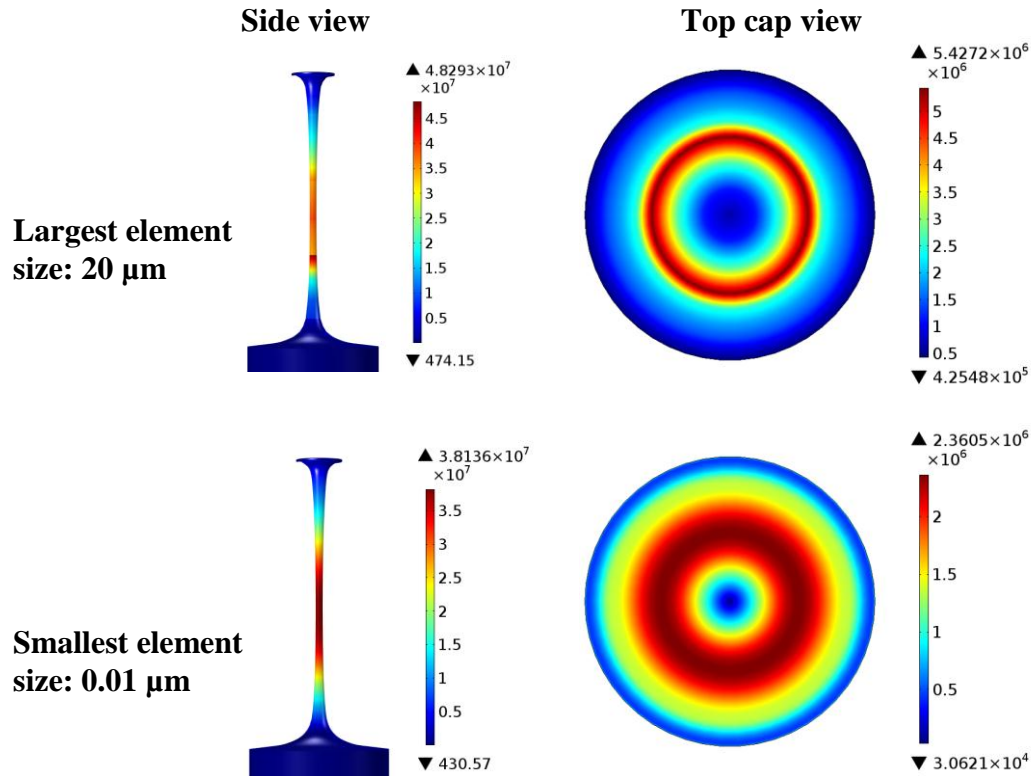


**Figure 3.6: FEA results (von Mises stresses) for mesh convergence study showing drastically different top cap stress distribution for the two extreme mesh sizes (20  $\mu\text{m}$  and 0.01  $\mu\text{m}$ ). Images for 100  $\mu\text{m}$  Kraton G1657 fiber with fixed cap BC.**

As this work focuses on fiber reaction forces resulting from applied displacements (showing convergence at larger element sizes), a mesh size of 0.1  $\mu\text{m}$  was chosen. This element size provides fast solution times, a relatively converged top cap stress distribution (Figure 3.4), and accurate fiber reaction force result (Figure 3.5).

### 3.4 Fixed BC

The first boundary condition examined is the simplest to model: the fixed BC. For this case, all nodes on the top surface are constrained from displacing. This model is computationally simple providing fast solution times and can simulate axial and shear loading. Figure 3.7 shows the resulting stresses for a 100  $\mu\text{m}$  Kraton G1657 fiber with a fixed BC after elongating 150  $\mu\text{m}$ . Fiber cap stress curves demonstrate the stress concentration at the cap perimeter which develops for fixed cap cases that can cause a weaker Mode 1 failure (detachment from pillar edge and propagation through center of fiber).

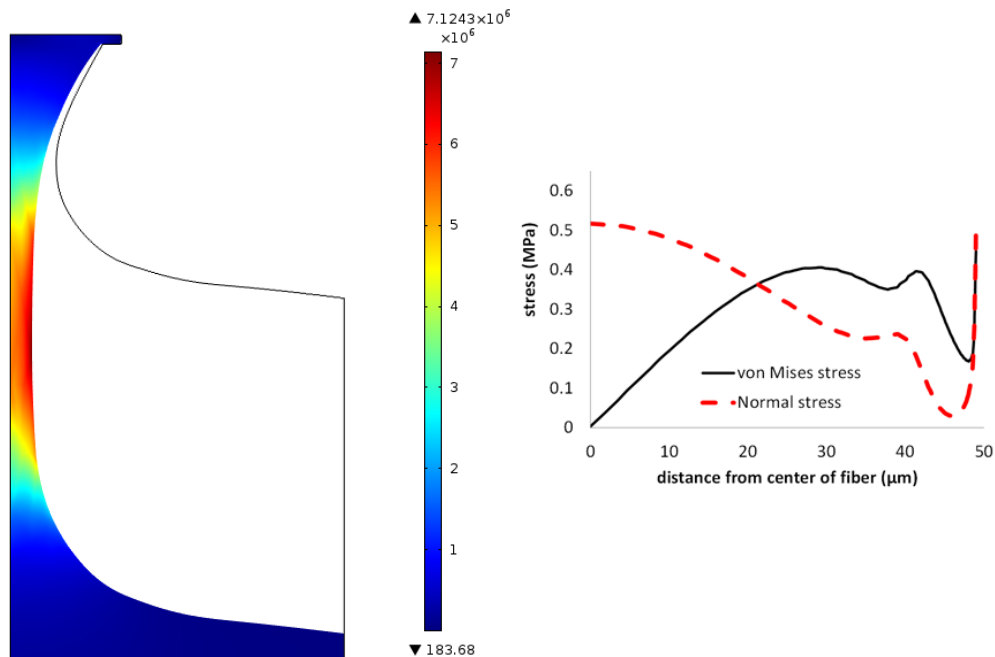


**Figure 3.7: Fixed BC simulation (100  $\mu\text{m}$  Kraton G1657 fiber). Central cross section (left) shows von Mises stresses (with outline of un-deformed fiber), graph (right) illustrates von Mises and axial stresses of top cap taken from the top surface of the fiber.**

### 3.5 Roller BC

While the fixed BC model creates an easy solution, results from this work showed that fibers can undergo significant cap shrinkage due to Poisson's ratio while maintaining adhesion. Figure 3.1 demonstrates the ability for the cap to shrink under load by imaging a fiber in SEM while attached to a silicon die. The fiber originally had a 24 $\mu\text{m}$  diameter cap. Due to the extension; the cap has shrunk to  $\sim 20 \mu\text{m}$ . For this early test, it was unsure if the shrinkage occurred over an long period of time (fibers had been attached for over a day) or if it was a significant effect that could occur in faster loading cycles. Modeling this fiber with a roller boundary condition gave almost identical cap shrinkage to what was experimentally measured [77].

Figure 3.8 shows the 100  $\mu\text{m}$  diameter Kraton fabricated in this work simulated with the roller boundary condition. The side view again demonstrates the cap shrinkage while the top cap stress distribution plot illustrates higher stresses at the fiber center and close to zero stresses at the fiber edge. This situation creates a potentially stronger adhering fiber as the cap edge is most vulnerable to peeling, causing failure due to cavitation near the fiber center at higher adhesion forces [43].

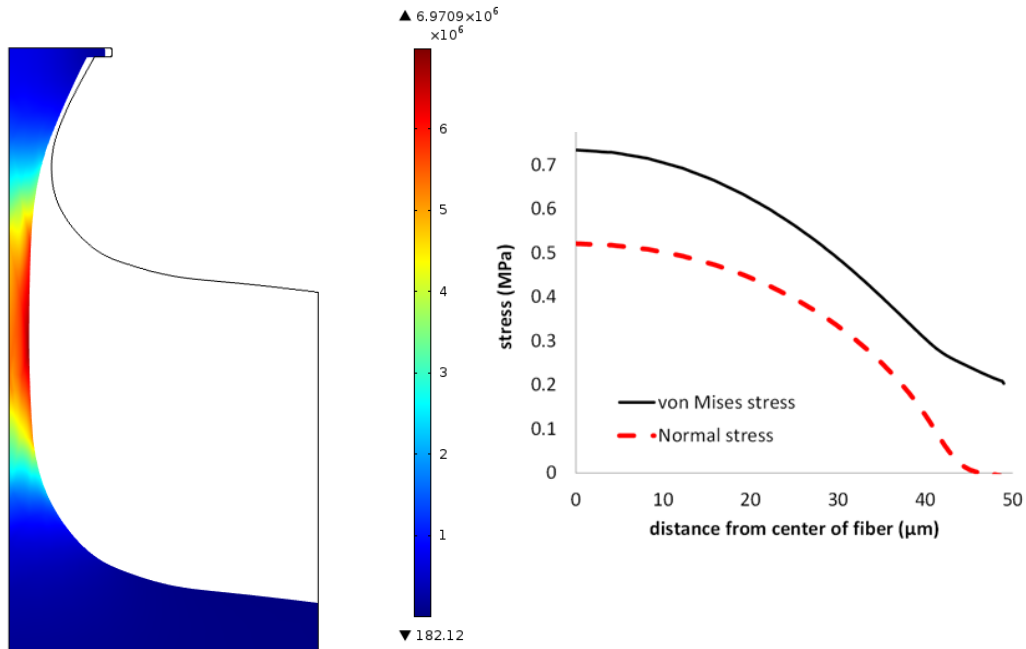


**Figure 3.8: Roller BC simulation (100  $\mu\text{m}$  Kraton G1657 fiber). Central cross section (left) shows von Mises stresses (with outline of un-deformed fiber), graph (right) illustrates von Mises and axial stresses of top cap taken from the top surface of the fiber.**

This BC produces more accurate results in some cases with good simulation convergence but cannot model shear loading.

### 3.6 Frictional BC

Both fixed and roller BCs are approximations to the actual adhesion mechanism. While a roller boundary condition may give good approximations, it is less realistic as the fiber must be able to support shear and all materials will demonstrate some friction. Implementing a BC which accounts for friction is

however computationally very demanding and requires a more complex model setup.

To achieve a frictional cap interface condition, the simulation needed to model a friction in the case of a net tensile load (due to fiber elongation). To be able to use a Coulomb friction equation, a modified friction force was defined using a method similar to technique described Zaghoul et al. [79] to determine the friction in an atomic force microscope (AFM) tip (equation 37).

$$F_f = (F_{vdW} - F_{normal})\mu \quad (37)$$

Where  $F_f$  is the frictional force preventing the fiber from shrinking,  $F_{vdW}$  is the van der Waals adhesion force,  $F_{normal}$  is the load that produces fiber elongation, and  $\mu$  is a static coefficient of friction to be determined experientially for specific surfaces (see chapter 5). While a Coulomb static friction relationship would generally be,  $F_f \leq \mu F_{normal}$ , this equation assumes the force is such that the fiber is just before sliding occurs and therefore assumed to be at the maximum friction case.

Figure 3.9 illustrates the COMSOL implementation of this equation requiring the extra complexity of a contact model to simulate the interface. To create the net compressive force required to model friction, a contact force was applied at the interface, equal to the van der Waals attraction force (estimated as the total adhesion force). To achieve converging results, a roller boundary condition at the fiber cap was required in addition to the friction condition to

prevent nodes from the fiber passing into the substrate. Due to the complexity of this model, convergence was only achieved with straight cylinder fibers. More complex shapes with overhanging caps would always cause diverging solutions. While parameters for this condition were extracted from the material (see chapter 5), convergence was not achieved with those values.

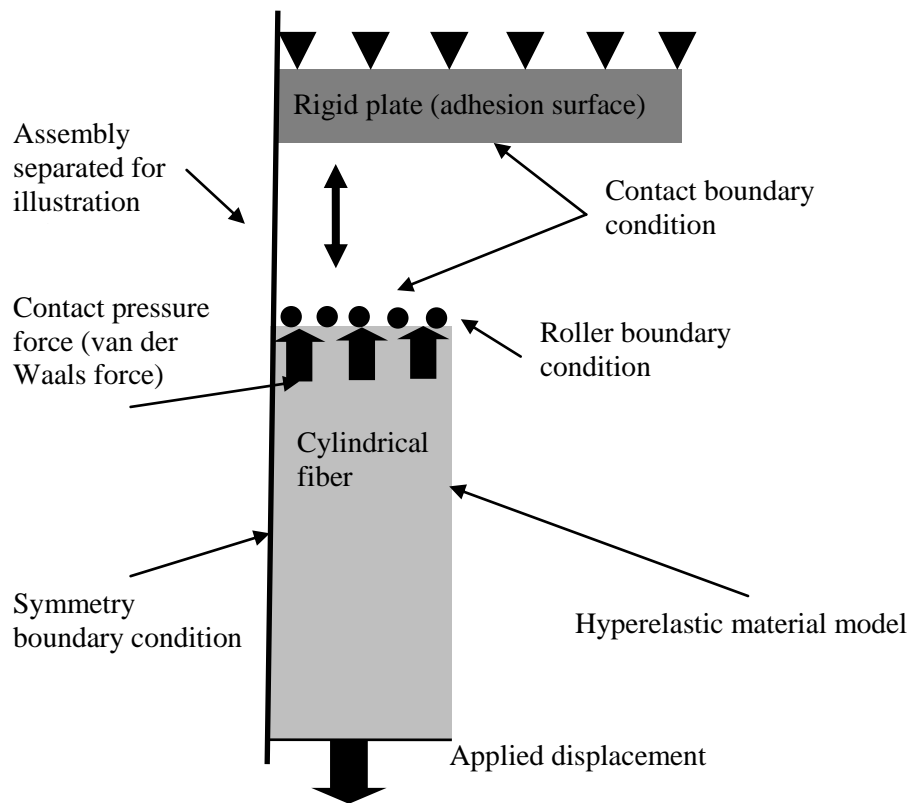


**Figure 3.9: Illustration of frictional boundary condition implemented in a COMSOL FEA simulation.**

The frictional BC was implemented for a straight cylinder fiber with the friction force in equation 37 used to model the contact interface. The simulation was extremely sensitive to the  $F_{vdW}$  and  $\mu$  parameters, with only a small

combination of values giving converged results. Figure 3.10 shows the FEA results for this frictional BC with the color map corresponding to radial deformation. Varying parameters between  $\mu = 0$  and  $\mu = 8$  with  $F_{vdw} = 100$  kPa allows full control between free roller and fixed conditions.  $F_{vdw}$  stresses higher than 100 kPa (for the 100  $\mu\text{m}$  diameter cylindrical fiber) did not produce converging results with this model. These values of van der Waals adhesion are significantly lower than our measured adhesion pressures. To achieve a fully functioning frictional BC simulation, a custom written FEA code will most likely be required for future work.

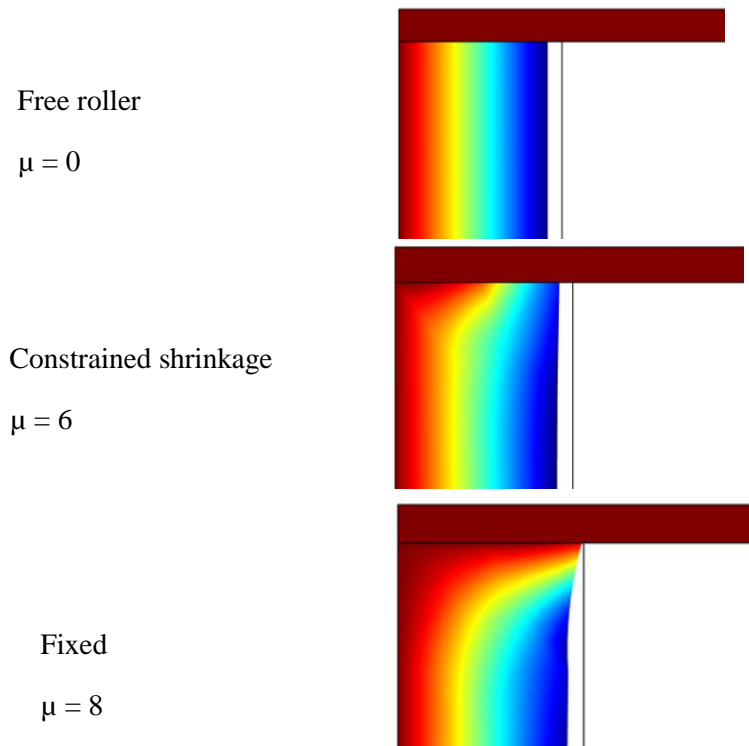


**Figure 3.10: Frictional boundary condition FEA results with straight cylinder fiber showing control of shrinkage with coefficient of friction,  $\mu$ .**

To determine if extra difficulty in modeling a fiber with the frictional BC is necessary, the results from fixed cap and roller cap BCs are compared. Figure 3.11 demonstrates that when looking only at the pure normal component of total reaction forces, the fixed and roller boundary condition FEA results give identical values.

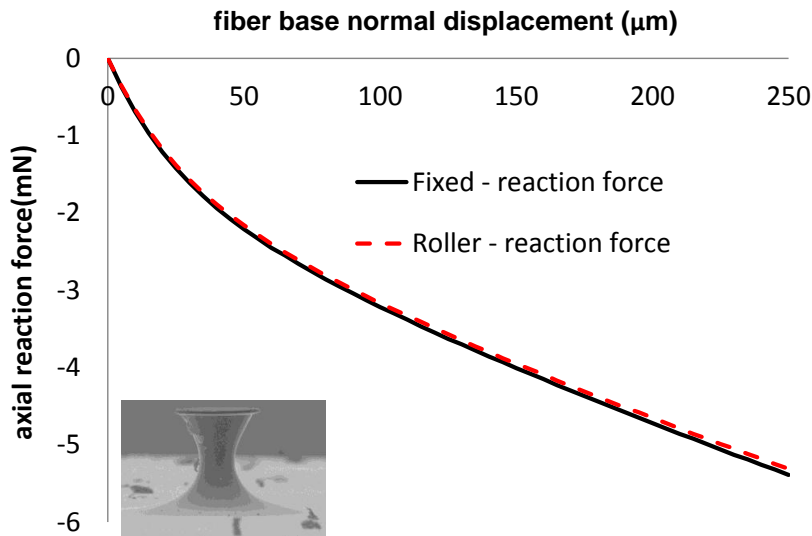


**Figure 3.11: Axial force vs. fiber elongation for fixed vs. roller cap boundary conditions FEA simulations (100 μm diameter ST-1060 fiber).**

In the case of the roller cap BC however, the cap was allowed to shrink significantly causing higher stresses in the adhesion interface boundary. This was caused by equivalent forces, developed from a fiber extension, acting over the smaller area of the interface contact (see Figure 3.12 for cap shrinkage vs. elongation of a fiber).

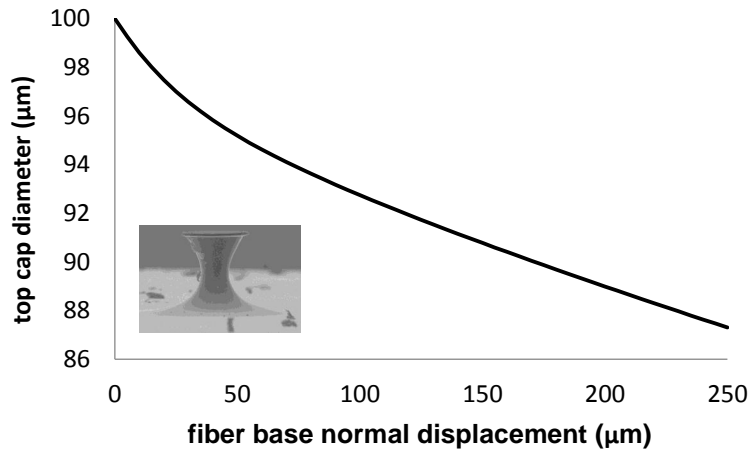


**Figure 3.12: Roller BC cap shrinkage vs. elongation for 100 μm diameter ST-1060 fiber.**

As adhesion failure will result from stresses at the contact interface exceeding the van der Waals attraction limit, the higher stresses developed from a roller interface (see Figure 3.13) suggest a weaker adhering fiber.

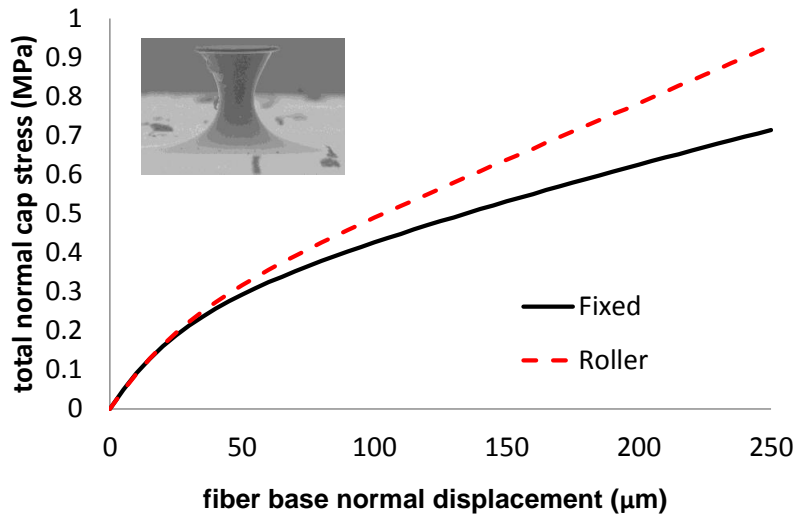


**Figure 3.13: Total axial forces of the top cap interface vs. fiber elongation for fixed and roller cap simulations (100 μm diameter ST-1060 fiber).**

### 3.7 Viscoelastic

As discussed in chapter 2, hyperelasticity and viscoelasticity are modeled separately in this work due to complexity in fitting data to a combined non-linear time dependent model and being able to implement the model to a commercially available FEA package. Using the *Linear Viscoelastic* material model in the Solid Mechanics module in COMSOL allows the user to input the shear modulus and relaxation time for each branch in the Generalized Maxwell model determined in chapter 2 to define the values for the first three time constants (determined from bulk material properties in Table 2-3). The elastic modulus ( $E_0$ ) determined in the Maxwell model was used in the Young's modulus section of the COMSOL model. To account for the material non-linearity, the viscoelastic properties chosen should be determined from tests performed at similar a strain as the model will be used for. As these materials are considered nearly incompressible, a Poisson's ratio of  $\nu = 0.49$  was used ( $\nu = 0.5$  can cause stability issues with numerical solutions [74]). Results for simulation are provided in chapter 5 compared with experimental adhesion tests.

Using either the linear viscoelastic or hyperelastic models developed in this chapter, the mechanical behavior of fibers under various loading conditions can be examined. This simulation can be used in the design phase along with material properties to develop fibers which have appropriate deformations, protecting from unwanted yield. It can also be used to design geometry of fibers to create top cap stresses with even distributions preventing concentrations and

deflecting stresses from the vulnerable cap edges. The different top cap stresses which will develop for the fixed or roller cap boundary condition are examined. Due to these differences, it is important to understand if the fiber being modeled will behave in a fixed, roller, or frictional manor to accurately predict the stresses in the fiber. This model provides significant improvements over available simulations in literature and provides a foundation for building future work to simulate an entire array of fibers to examine the peeling phenomena.

## 4 SINGLE FIBER FABRICATION

### 4.1 Introduction

This section includes fabrication steps required to make single fiber samples which could be tested in chapter 5 to experimentally verify the simulation presented in the chapter 3. For this testing, a new adhesive design with widely spaced fibers was required. Fabrication was completed using the University of Alberta NanoFab facilities and equipment available in the research group's lab.

The main objective in this section was to fabricate fibers consisting of diameters ranging from 60  $\mu\text{m}$  to 200 $\mu\text{m}$  (all with  $\sim 120$   $\mu\text{m}$  height), various undercut shapes, and cap overhang which could be cut out manually into a single fiber sample. For additional information useful in simulating and optimizing adhesive fibers, a section of the mask was made to study the proximity effect of fibers and determine the separation distance to achieve perfectly round fibers. As previous work in the lab has shown that roughly 1:1 aspect ratio fibers with an hour glass shaped undercut show the best adhesion, the 100  $\mu\text{m}$  diameter fibers were expected to be among the best performance for the heights used. Several arrays of 2 cm x 2 cm arrays of 100  $\mu\text{m}$  fibers were also fabricated at different fiber spacing to allow the investigation of spacing on adhesion. This chapter includes the mask design layout, clean room fabrication procedures, as well as

micro replication methods used to produce final adhesive fibers<sup>3</sup>. Attempts at nano-scale fiber fabrication using electron beam lithography were made early in this project and are discussed in Appendix A.

## 4.2 Mask Design

This project required single fibers of a wide range of sizes and geometries which can be tested individually. As single fibers will be used for adhesion testing, larger sizes (up to 200  $\mu\text{m}$  diameters) than previously used [81] were expected to be required to allow accurate measurements from the load cell (described in the next chapter). To maximize the number of geometries which could be fabricated from one mold, arrays of sizes were repeated four times, all of which would receive a different deep UV (DUV) exposure dose, thus creating different undercuts. Figure 4.1 illustrates the final mask design printed.

---

<sup>3</sup> Sections of this work were presented at the 24<sup>th</sup> Canadian Congress of Applied Mechanics in Saskatoon SK in June 2013 [80].

Array section parameters only		Array section	Single fiber test section			
Diameter (μm)	Spacing (μm)	Exposure area 1	Exposure area 2	Exposure area 3	Exposure area 4	
100	20		1 ■ ■ ■ ■	1 ■ ■ ■ ■	1 ■ ■ ■ ■	1 ■ ■ ■ ■
			2 ■ ■ ■ ■	2 ■ ■ ■ ■	2 ■ ■ ■ ■	2 ■ ■ ■ ■
			3 ■ ■ ■ ■	3 ■ ■ ■ ■	3 ■ ■ ■ ■	3 ■ ■ ■ ■
			4	4	4	4
		See Figure 4.3	See Figure 4.3	See Figure 4.3	See Figure 4.3	
100	40		5 ● ● ● ●	5 ● ● ● ●	5 ● ● ● ●	5 ● ● ● ●
			6 ● ● ● ●	6 ● ● ● ●	6 ● ● ● ●	6 ● ● ● ●
			7 ● ● ● ●	7 ● ● ● ●	7 ● ● ● ●	7 ● ● ● ●
			8 ● ● ● ●	8 ● ● ● ●	8 ● ● ● ●	8 ● ● ● ●
100	60		9 ● ● ● ●	9 ● ● ● ●	9 ● ● ● ●	9 ● ● ● ●
			10 ● ● ● ●	10 ● ● ● ●	10 ● ● ● ●	10 ● ● ● ●
			11 ● ● ● ●	11 ● ● ● ●	11 ● ● ● ●	11 ● ● ● ●
			12 ● ● ● ●	12 ● ● ● ●	12 ● ● ● ●	12 ● ● ● ●
100	80		13 ● ● ● ●	13 ● ● ● ●	13 ● ● ● ●	13 ● ● ● ●
			14 ● ● ● ●	14 ● ● ● ●	14 ● ● ● ●	14 ● ● ● ●
			15 ● ● ● ●	15 ● ● ● ●	15 ● ● ● ●	15 ● ● ● ●
			16 ● ● ● ●	16 ● ● ● ●	16 ● ● ● ●	16 ● ● ● ●
100	80		17 ● ● ● ●	17 ● ● ● ●	17 ● ● ● ●	17 ● ● ● ●
			18 ● ● ● ●	18 ● ● ● ●	18 ● ● ● ●	18 ● ● ● ●
			19 ■ ■ ■ ■	19 ■ ■ ■ ■	19 ■ ■ ■ ■	■ ■ ■ ■

**Figure 4.1: Photomask design layout illustration: array test section, 4 identical single fiber test sections to be exposed to different DUV doses (represented by different color of shading), and 3x3 fiber proximity test section in label 4 (see Figure 4.3). Each section of single fibers (numbered 1-3 and 5-19) have 3 features spaced 5 mm apart. Note fiber size and spacing not to scale.**

Each label in the single fiber tests section in the mask represents a different fiber size (circular and square as shown in Figure 4.1). Table 4-1 provides a summary of the fiber size which was made in each label.

**Table 4-1: Fiber size list for single fiber photomask.**

<i>Label</i>	<i>Fiber size (<math>\mu\text{m}</math>)</i>	<i>Label</i>	<i>Fiber size (<math>\mu\text{m}</math>)</i>
<b>1</b>	60	<b>11</b>	140
<b>2</b>	80	<b>12</b>	160
<b>3</b>	100	<b>13</b>	180
<b>4</b>	3x3 array	<b>14</b>	200
<b>5</b>	200	<b>15</b>	120
<b>6</b>	160	<b>16</b>	140
<b>7</b>	60	<b>17</b>	160
<b>8</b>	80	<b>18</b>	180
<b>9</b>	100	<b>19</b>	200
<b>10</b>	120		

The proximity effect of fibers causes square shaped posts to be formed when exposing to a circular mask pattern. This can be explained by varying distances within the square grid array as shown in Figure 4.2.

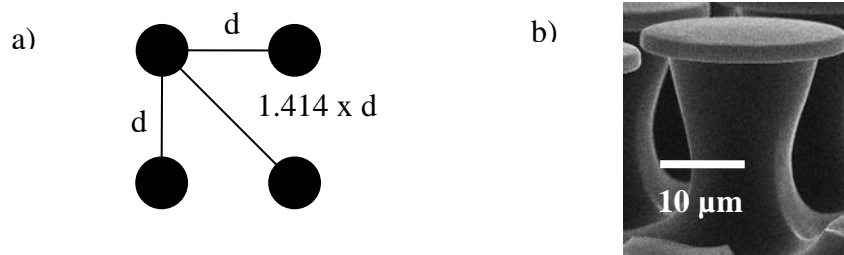


**Figure 4.2: Photomask exposure proximity effect: a) illustration of top view fiber array spacing, b) SEM image of an example of square shaped neck fiber caused by proximity effect. Reprinted with permission from [19]. Copyright (2013) Ferguson.**

As the side of a fiber facing the distance ‘d’ was closer than the diagonal (1.414 x d), the portion of the fiber neck facing the diagonal in the array will get exposed further, giving the square shaped neck as show in the example SEM

image in Figure 4.2. This effect will be non-existent for this work as 5 mm wide spaced fibers effectively behave as infinitely spaced fibers. It was however of interest for further fiber array optimization designs to determine at which separation distance proximity would cause non-circular fibers. To study this behavior, a section was added to the mask, located in label number 4 in Figure 4.1. The section consists of 3 x 3 fiber arrays, giving the center fiber the same proximity conditions as in a full fiber array in an adhesive sheet. By examining the center fiber in the array of different spacing and different fiber sizes, an estimate can be made of the fiber diameter/spacing combination which will cause the proximity effect. Figure 4.3 illustrates the mask design for this section.

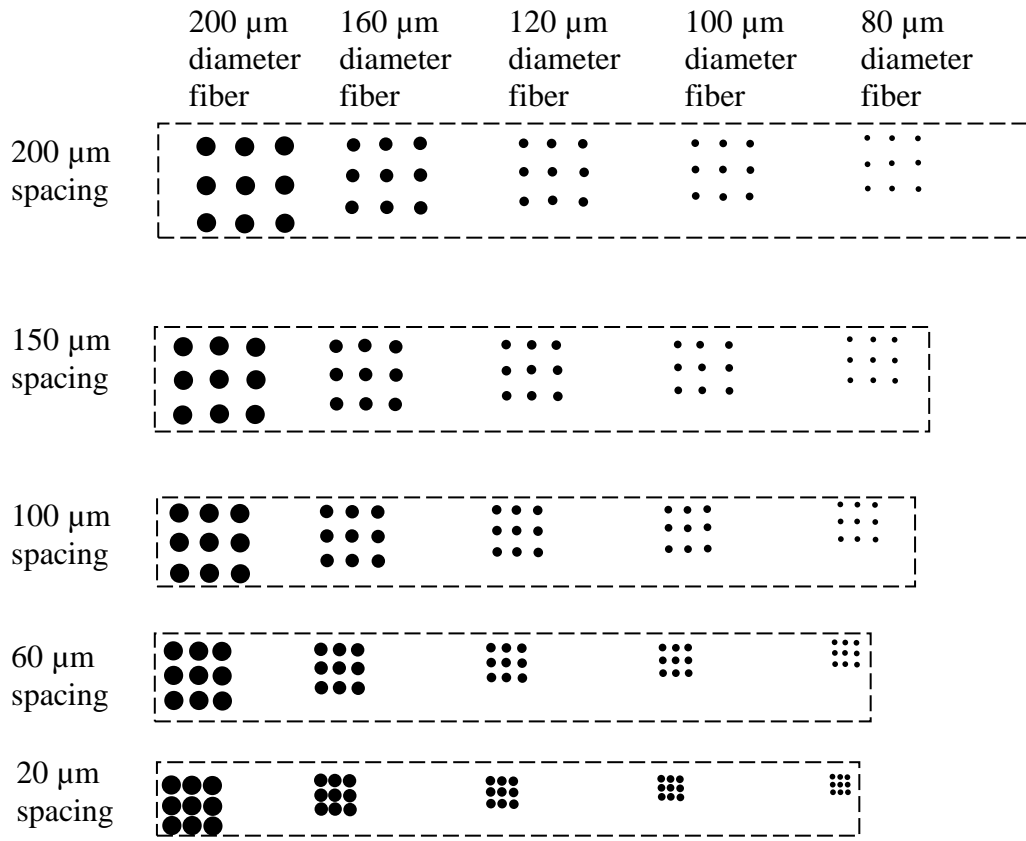


**Figure 4.3: Fiber proximity effect study section of single fiber mask design.**

#### 4.3 Clean-room Master Mold Fabrication

Clean room fabrication was based on methods previously described in [7,81]. As fabrication process development was not an aspect of this thesis, only a description of the materials and parameters used will be given. Detailed characterizations of the fabrication steps can be found in [7]. Two fabrication steps were employed; one to make overhanging cap, hourglass shaped fibers, and one to make straight cylinder fibers. Both processes are described in the following sections.

#### 4.3.1 Substrates Used

Master molds (positive structures) were fabricated using 5" x 5" square polymethylmethacrylate (PMMA) substrates for overhanging cap shapes and 4" round Test Grade silicon wafers for straight cylinder posts. The PMMA used was commercially available as OPTIX® manufactured by Plaskolite [82] at Home Depot in large sheets and cut into 5" x 5" square substrates with a commercial laser engraver (Versa Engraver VLS3.50).

#### 4.3.2 Spin Coating

The first step in the fabrication process for each mold was to spin coat a layer of SU-8 2005 on PMMA and SU-8 2075 on silicon. SU-8 is a negative epoxy based photoresist [83] which will define the caps for the undercut fibers or (in the case of SU-8 2075) becomes the full structure in the straight cylinder post. This process was completed in the University of Alberta class 1000 NanoFab facility. Conditions during fabrication were 19.5°C and 48.8% relative humidity (RH).

Previous work [19] used 2-3µm thick SU-8 for ~20-40 µm diameter cap undercut fibers. As this work will focus on ~100-200 µm diameter fibers, thicker caps were required. SU-8 was spun onto the substrates using a Headway Resist Spinner. The spin recipes used to make three different resist thicknesses on PMMA (labeled SFM1, SFM2, and SFM3 with SU-8 2005) and on silicon (labeled SFM-Si with SU-8 2075), based on the suppliers specifications describe

in Table 4-2. Film thicknesses were measured by scratching a small area of the substrate with tweezers and measured with an Alpha Step IQ surface topography profiler. To assist with SU-8 adhesion to the silicon substrate, the SFM-Si sample was coated with a thin layer of SU-8 2005 and blanket exposed for 30 seconds to crosslink the entire surface. Consecutive SU-8 coats would now have a much improved adhesion to the already crosslinked SU-8.

**Table 4-2: Summary of SU-8 spin recipes for substrates prepared.**

Substrate	SFM1 (SU-8 2005)	SFM2 (SU-8 2005)	SFM3 (SU-8 2005)	SFM-Si (SU-8 2075)
<i>Ramp<sub>1</sub> (sec)</i>	1	1	1	5
<i>Speed<sub>1</sub> (RPM)</i>	500	500	500	500
<i>Time at speed<sub>1</sub></i>	5	5	5	20
<i>Ramp<sub>2</sub> (sec)</i>	1	1	1	5
<i>Speed<sub>2</sub> (RPM)</i>	3000	2000	1000	3000
<i>Time at speed<sub>2</sub></i>	40	40	40	30
<i>Measured thickness (μm)</i>	4.5	5.2	7.5	134

After spin coating, the PMMA substrates were soft baked in a Blue M convection oven at 90°C for 20 minutes. The silicon substrate was soft baked on a hotplate at 70°C for 5 minutes followed by 95°C for 20 minutes. Soft bake times have been previously experimentally determined in the lab for PMMA substrate processing [19].

#### 4.3.3 UV Photomask Exposure

The soft baked SU-8 was then exposed to 365 nm UV light with an ABM Inc. Mask Aligner. This process was also completed in the class 1000 clean room. Improved mask contact was achieved by clamping a metal plate to the opposite

side of the mask with an array of flat ended plastic screws as described in [19]. These screws were manually adjusted while observing Newton rings to achieve better contact. This correction had been previously developed as PMMA substrates often become slightly warped after laser cutting, causing areas of poor photomask contact resulting in light scattering during exposure.

An exposure dose of  $250 \text{ mJ cm}^{-2}$ , as recommended by the supplier [83] was used for the silicon substrate. Acrylic substrates were exposed with  $450 \text{ mJ cm}^{-2}$  (more than the recommended value by the supplier) as an overexposure for SU-8 will give improved adhesion to the substrate [7]. Exposing the SU-8 to UV light crosslinks the polymer in transparent areas of the mask, defining the fiber caps. A post exposure bake was then done in the Blue M oven for the resist at  $90^\circ\text{C}$  for 20 minutes for the PMMA substrate and 40 minutes for the silicon substrate.

The unexposed SU-8 on PMMA substrates was removed by developing by spinning the substrate on the Headway Spinner at 3000 RPM. A spray bottle of SU-8 developer and IPA was used in alternating cycles (4 times) by spraying across the radius of the spinning substrate. After this development, only circles of SU-8 remained which would become the top caps of the structures. The silicon substrate was developed in a SU-8 developer bath for 7 minutes giving the final vertical walled cylinder posts.

#### 4.3.4 Deep UV Exposure

A second exposure on the underlying PMMA was then done with the SU-8 structures defining a second photomask, opaque to DUV light. The substrates were exposed to a 254 nm DUV exposure source (Stratalinker 2400, normally used for DNA crosslinking) available in our lab. The molecular weight of PMMA decreases during the exposure, allowing subsequent development of areas which are exposed. The DUV source was previously characterized to have an intensity of  $4.4 \pm 0.2 \text{ mW cm}^{-2}$  [19]. The exposure can be partially collimated by adding a 1:1 plastic grid between the substrate and the DUV bulb [7], reducing the intensity to  $1.5 \pm 0.4 \text{ mW cm}^{-2}$ . Adding collimation produces higher aspect ratio structures and gives less undercut [19]. This work used a combination of collimated and uncollimated exposures to achieve various types of undercut angles, see Table 4-3.

**Table 4-3: Deep UV exposure recipe for PMMA substrates SFM1, SFM2, and SFM3. Note, exposure areas 1, 2 and 3 in Figure 4.1 illustrate areas of the mold with different exposure doses as listed below.**

Area of Mask	Exposure type	SFM1 (hours)	SFM2 (hours)	SFM3 (hours)
<b>Exposure Area 1</b>	<i>Uncollimated</i>	8	19	0
<b>Exposure Area 2</b>	<i>Collimated</i>	24	0	63
<b>Exposure Area 3</b>	<i>Uncollimated</i>	8	8	0
<b>Exposure Area 4</b>	<i>Collimated</i>	20	0	47
<b>Exposure Area 5</b>	<i>Uncollimated</i>	8	6.5	0
<b>Exposure Area 6</b>	<i>Collimated</i>	16	0	30
<b>Exposure Area 7</b>	<i>Uncollimated</i>	8	5	0
<b>Exposure Area 8</b>	<i>Collimated</i>	0	0	16

The exposure in each section was modified according to Table 4-3 by covering portions of the substrate with aluminum foil. During the DUV exposure, significant residual stresses developed in the PMMA substrate due to chemical changes occurring in the material. These residual stresses have been found to cause cracks in the top surface of the substrate, significantly deteriorating the performance of the final adhesive [19]. To negate this effect, all substrates were annealed at 80°C overnight immediately following DUV exposure.

#### 4.3.5 *Development*

The final fiber shapes are created by developing the substrate in SU-8 developer. The already crosslinked SU-8 has an extremely slow development rate while the DUV exposed PMMA develops rapidly. The areas under the SU-8 caps prevented DUV exposure to the PMMA and therefore are the only structures remaining. While the lower molecular weight PMMA develops much quicker than unexposed PMMA, the unexposed material will still develop at low rates. This unexposed development rate allows an undercut beneath the fiber cap, which did not receive any exposure, and was crucial in the final performance of the adhesive fiber.

Substrates were developed partially and observed under a microscope to determine when the appropriate neck thickness was reached without over developing. Substrate SFM1 was developed for 80 minutes in an SU-8 developer bath, SFM2 and SFM3 were developed for 50 minutes. The depths of PMMA

development for each substrate and exposure area were determined using a stylus profilometer and compiled in Table 4-4

**Table 4-4: PMMA exposure depth measured with stylus profilometer.**

Area of Mask	SFM1 depth ( $\mu\text{m}$ )	SFM2 depth ( $\mu\text{m}$ )	SFM3 depth ( $\mu\text{m}$ )
<i>Exposure Area 1</i>	118	126	94.6
<i>Exposure Area 2</i>	118	108	83.4
<i>Exposure Area 3</i>	117	98	62.5
<i>Exposure Area 4</i>	103	86	27.6

#### 4.3.6 *Fiber Proximity Effect Results*

As previously mentioned, the proximity difference in a square array caused square shaped fiber necks. The 3 x 3 fiber array section of the photomask was used to determine what critical separation distances caused square shaped fiber necks. Observation under an optical microscope provides a simple method to view the fiber cap undercut and the neck shape. Figure 4.4 shows four of these optical images of SFM1 after final development. The bright outside ring in Figure 4.4 a) represents the fiber cap undercut, while Figure 4.4 b), with a focal plane lower into the fiber, focused on the neck, shows a bright central area representing the fiber neck. As illustrated in Figure 4.4, molds SFM1, SFM2, and SFM3 all showed the first sign of non-circular undercut for spacing of 20  $\mu\text{m}$ . This effect was exposure and fiber diameter independent, with the critical separation distance being 20  $\mu\text{m}$ . As the separation step sizes fabricated were 40  $\mu\text{m}$  and 20  $\mu\text{m}$ , the actual critical distance will be somewhere between these two values.

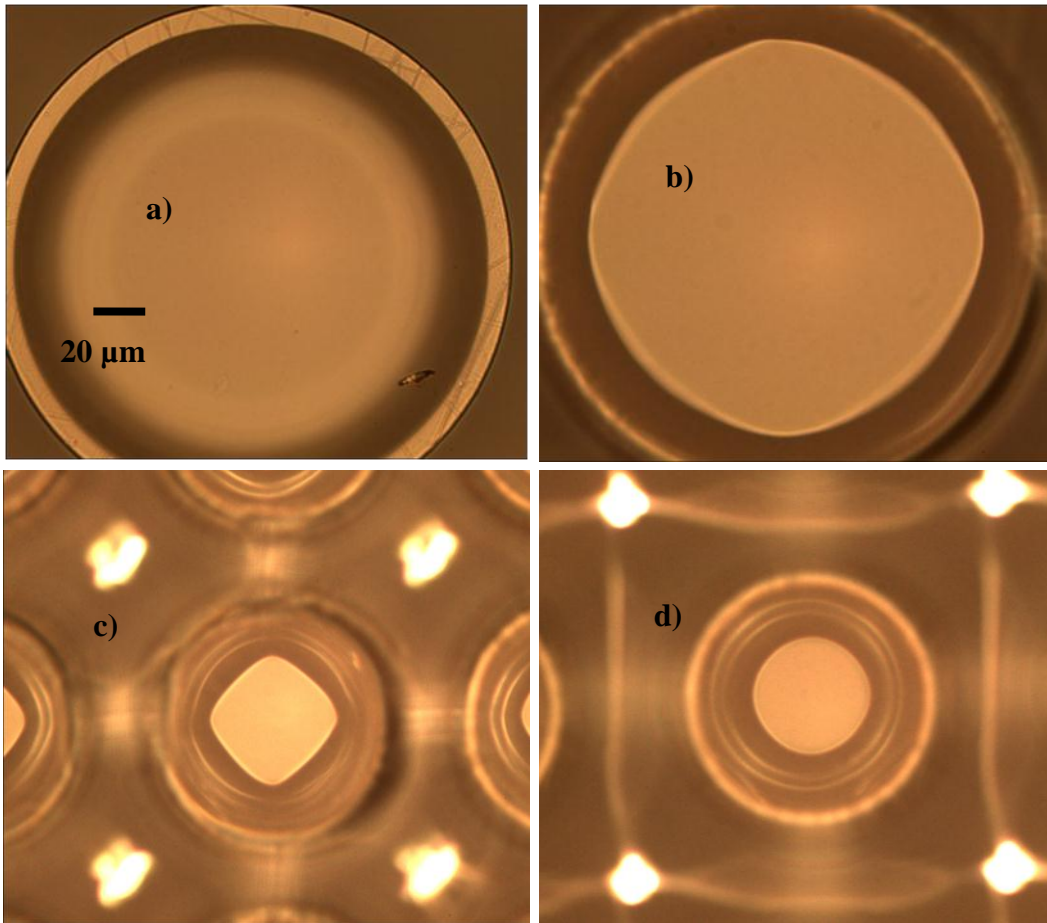


**Figure 4.4: Optical images of SFM1 master: a) shows circular cross sectional neck with 200 μm spacing for a 200 μm diameter fiber, b) shows a slightly square cross section developing for a 200 μm diameter fiber with 20 μm spacing, c) shows an extremely square shaped neck for 80 μm diameter fiber with 20 μm spacing (a was focused on the fiber cap while b and c are focused on the fiber neck to clarify effect, both image b and c will still show non-circular shape when focused on top cap), d) round cross section of 40 μm spacing.**

#### 4.3.7 *Mold Fabrication Results*

The initial step in examining the quality of the fabrication was optical microscope inspection of the substrate as explained in the previous section. Inspection was done frequently between developments until the desired neck thickness or cap overhang was achieved. Residue was then removed by placing the substrate on the spinner and spraying SU-8 developer on the rotating substrate followed by an air dry during continued spinning. Final inspection of the master mold was then done with an optical microscope. Due to the wide range of fiber sized on this photomask, this stage was critical in order to determine which fibers survived and which have appropriate undercuts for further replication work. Figure 4.5 gives sample optical microscope images of a range of fibers fabricated showing which features to look for to achieve good adhesives.

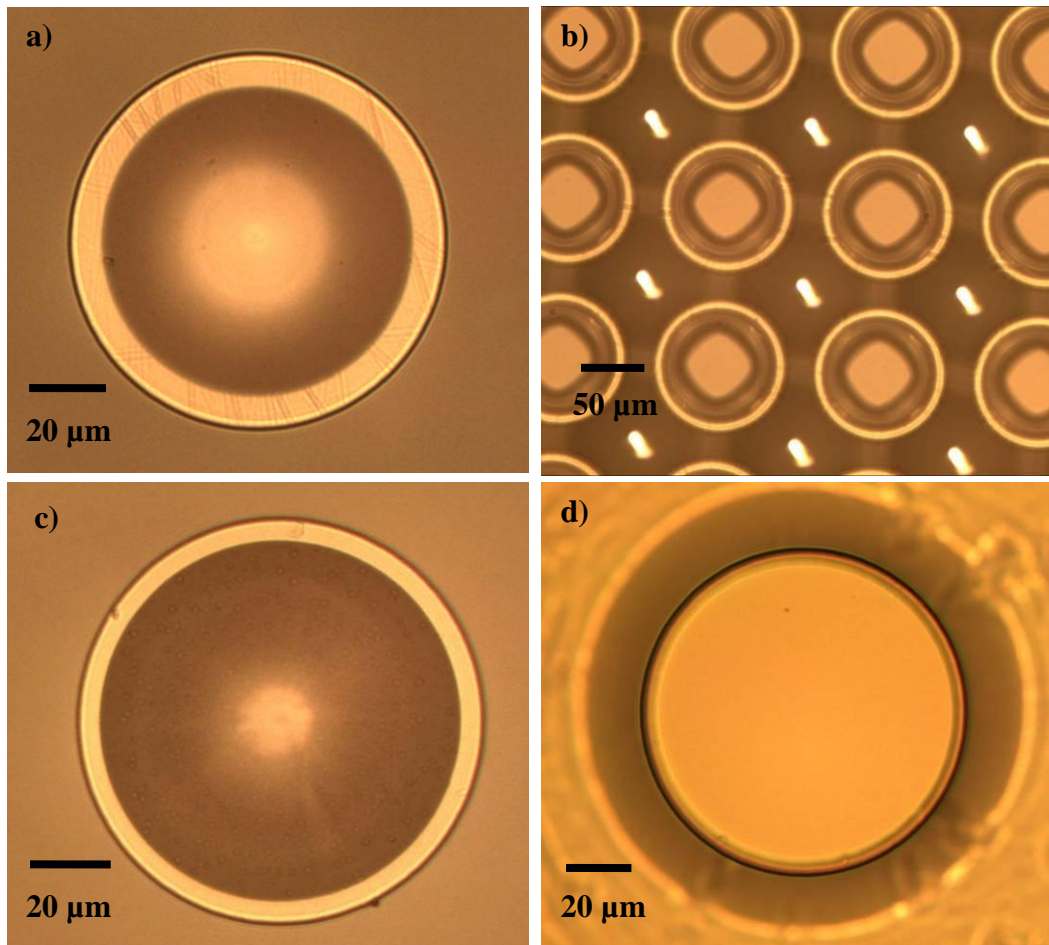


**Figure 4.5: Optical microscope images (all are 100  $\mu\text{m}$  fibers) on PMMA master molds, a) SFM1, exposure area 1 single fiber showing close to ideal undercut and cap overhang, b) SFM1 exposure area 1 fiber array with 20  $\mu\text{m}$  spacing showing slightly less undercut and a non-circular neck cross section due to proximity effect, c) SFM2, exposure area 1 single fiber showing an extremely narrow neck, resulting in an extremely delicate fiber which would not survive replication molding, d) SFM3, exposure area 4 single fiber showing almost no undercut or cap overhang, resulting in an almost straight cylinder fiber which would give poor adhesion results.**

To avoid attempts at further replication of fibers which did not survive, Table 4-5 gives a summary of the minimum feature size of the PMMA master molds which were fabricated.

**Table 4-5: Minimum surviving feature size on PMMA master molds, determined by optical microscopy. Note, feature size listed represents top cap diameter; actual neck dimensions where failure occurs was much smaller.**

Area of Mask	SFM1 min feature diameter ( $\mu\text{m}$ )	SFM2 min feature diameter ( $\mu\text{m}$ )	SFM3 min feature diameter ( $\mu\text{m}$ )
<i>Exposure Area 1</i>	80	100	60
<i>Exposure Area 2</i>	80	80	60
<i>Exposure Area 3</i>	80	60	60
<i>Exposure Area 4</i>	80	60	60

#### 4.4 Replication Molding Procedures

With four complete master molds, the remaining processing for final fiber fabrication was completed in our lab. A well documented polymer replication toolset termed Soft Lithography [27] has been used to fabricate micro devices for almost two decades. These processes are attractive as they can produce feature sizes in the tens of nanometers, smaller than the polymer molecules [84] with cycle times as low as several seconds. This work used the most common type of soft lithography, micro replication molding (REM). This method uses a negatively patterned mold [85], cast from the master mold fabricated in the clean room (described in the previous section) generally made from PDMS or other silicone rubbers. Work for this thesis used TC-5030 (BJB Enterprises) silicone rubber negative molds. The structural thermoset polymer from which the final adhesive

is made is generally cast onto the negative mold and cured through UV or heat exposure [84]. Incomplete filling of structures with high aspect ratios is minimized by vacuum degassing prior to curing. This work also incorporates a newer replication method, employing thermoplastic materials such as styrene-ethylene/butylene-styrene (SEBS) block copolymers, resulting in much quicker fabrication times, a wide range of available materials, and significantly reduced costs. Figure 4.6 illustrates the method used to fabricate single fibers and fiber arrays using thermoplastic materials. The three materials used for replication molding were the same as chosen for material property analysis in chapter 2 of this thesis.

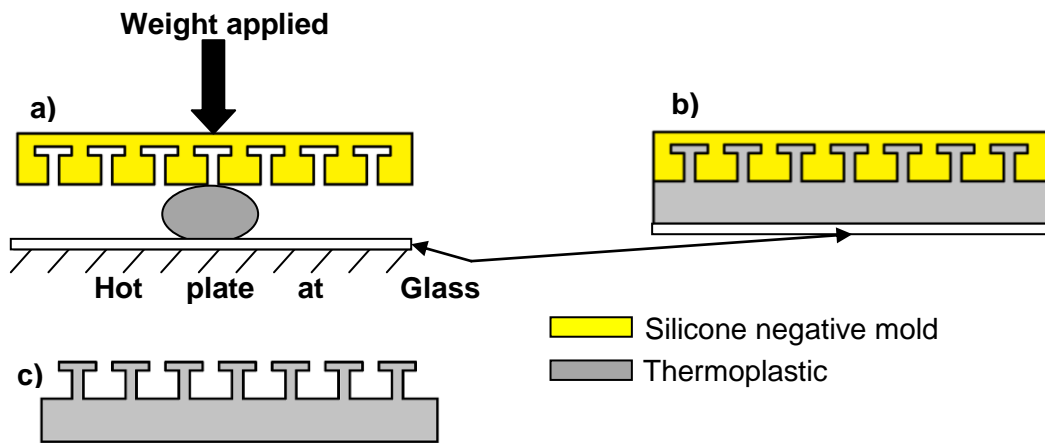


**Figure 4.6: Thermoplastic fiber casting process illustration, a) thermoplastic heated on hotplate with pressure on mold, b) negative mold/thermoplastic was allowed to cool, c) de-mold from silicone rubber then de-mold from glass for final thermoplastic micro structures. Starting with a polymer sample thickest in the center greatly reduces the trapped gasses in the mold and permits excellent reproduction without the need for applied vacuum.**

#### 4.4.1 Negative Mold Fabrication

The negative mold was cast from TC-5030 silicone rubber available from BJB Enterprises Inc. This material was chosen over the more frequently used Sylgard 184 PDMS mold materials due to its significantly superior durability and resistance to tearing. The properties of the two materials are compared in Table 4-6.

**Table 4-6: Negative mold material property: comparison between TC-5030 and Sylgard 184 [86,87]**

Property	TC-5030	Sylgard 184
<i>Color</i>	Colorless	Colorless
<i>Mixed viscosity (cP)</i>	45,000	3500
<i>Working time</i>	25 min	1.5 hours
<i>Cure time at 25°C</i>	24 hours	48 hours
<i>Hardness (Shore A)</i>	30	43
<i>Tensile Strength (MPa)</i>	4.8	6.7

The silicone was mixed according to the supplier recommendations [87], measured by weight, 100 parts component A and 10 parts component B. Approximately 8 grams of mixed silicone were required to make one cast from a master mold substrate. The prepolymer was cast onto the substrate (no silanization was required for de-molding) and vacuum degassed for approximately 10 minutes. To accelerate the process, the mold was put in an oven at 80°C for 3 hours for complete curing. The silicone was then carefully demolded from the substrate and stored in a Ziplock bag to prevent dust contamination. The substrate was also stored for future negative mold fabrication.

#### 4.4.2 Thermoset Fiber replication

Significant characterization on replication fidelity, polymer durability, and negative mold compatibility was completed early in this project (presented at the 24<sup>th</sup> Canadian Congress of Applied Mechanics in Saskatoon SK. [80]). From these results, ST-1060 and ST-1087 polyurethane elastomers were chosen to be the best thermoset materials available in our lab to examine for this thesis.

Both materials were mixed according to supplier specifications [59,60]. The prepolymer was vacuum degassed in a small container for approximately 5 minutes. The liquid was then poured onto the negative silicone mold and vacuum degassed again for approximately 10 minutes. The mold was then room temperature cured at 24 hours followed by 16 hours at 80°C. After cooling, the polyurethane was carefully de-molded from the silicone mold and was ready for use.

While the above method replicates fiber casts very well and was a good method for producing fiber arrays, this work required very flat, thin backing layers for testing single fibers. The process was slightly modified by only placing a single drop of prepolymer on the area of the mold with the single fiber to be replicated. The mold was vacuum degassed for approximately 10 minutes and then covered with a thin, rigid Topas Advanced Polymers cyclic olefin copolymer (COC) sheet [61] (available in the lab) for curing.

Cutting samples from cured polyurethane sheets into single fiber tests samples required extra processing to prevent contamination. When cutting the polymer significant debris would be scattered around the area within several millimeters of the knife. As the test sample was required to only be a few millimeters square, this would always result in particle debris on the fiber cap, resulting in almost negligible adhesion. To prevent contamination of the fiber, the sample was cut into the test size prior to de-molding from the silicone negative mold and the silicone sheet on the back side of the polyurethane, see Figure 4.7. After the sample was cut to size, it was de-molded and removed from the backing sheet. This method allowed the polymer to be cut to any desired size without contamination of the surface.

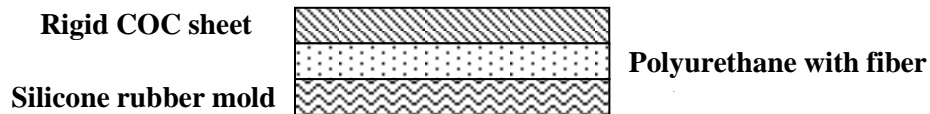


**Figure 4.7: Illustration of polyurethane single fiber test sample preparation. Sample was cut while contained within the mold and rigid silicone sheet to prevent fiber contamination.**

#### 4.4.3 Thermoplastic Fiber replication

Thermoplastic replication was extremely attractive for the field of gecko inspired adhesives as it significantly reduces the cost and fabrication time. The process described in Figure 4.6 can also be extended to a roll-to-roll fabrication process in which large sheets of adhesive could be manufactured.

Important parameters in thermoplastic replication are the resulting surface quality and replication fidelity. Many polymers were purchased for the lab, some of which provide extremely precise nano-scale replication fidelity, while others produce rough surfaces (see Figure 4.8) or do not properly fill the mold cavities. Table 4-7 gives a summary of the materials tested and their general performance.

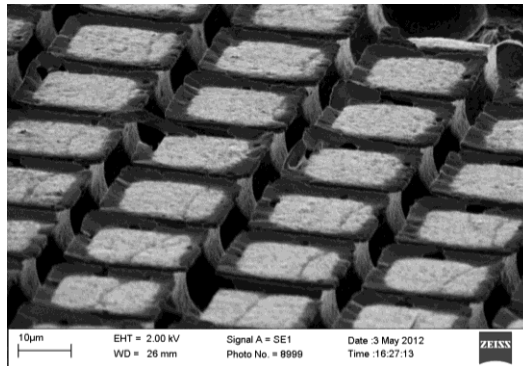


**Figure 4.8:** Array of square micro posts, cast from Dryflex thermoplastic elastomer showing poor replication fidelity with very rough top surfaces.

**Table 4-7:** Qualitative measure of replication success for thermoplastic materials tested (properties taken from data sheets [58,88-94]).

<i>Thermoplastic</i>	<i>Hardness</i>	<i>Replication fidelity</i>	<i>Surface quality</i>	<i>Temperature tolerance (°C)</i>	<i>Supplied as:</i>
<i>Kraton G1651</i>	60 Shore A	*Did not flow at 200°C	*NA	NA	Powder crumb
<i>Kraton G1657</i>	47 Shore A	Good	Excellent	NA	Dusted pellets
<i>Kraton G1660</i>	NA	*Did not flow at 200°C	*NA	NA	Powder crumb
<i>Polystyrene</i>	Rockwell M 70	Excellent	Excellent	95	Petri dish
<i>Tygon tubing</i>	56 Shore A	Excellent	Excellent	74	Tube
<i>Dryflex® T509</i>	50 Shore A	Poor	Poor	~100	Pellets
<i>Dryflex® T909</i>	65 Shore A	Poor	Poor	~100	Pellets
<i>Dryflex® C3 6068</i>	68 Shore A	Very poor	Very poor	~100	Pellets

Polystyrene (PS) was also able to produce excellent nano-scale replication. While this material was not useful as an adhesive material, it was used in this work for some SEM imaging as it was much more durable during the gold-coat deposition required to view the casts without charging effects. Figure 4.9 shows the versatility of replication molding with PS by replicating a common grass (*Agropyron repens*) found in the river valley close to the University of Alberta. The PS was melted on a hot plate at 200°C into a TC-5030 negative mold cast directly from the grass. As structures fabricated in this thesis were relatively large (as compared to high fidelity shown possible in Figure 4.9), casts of PS were used in some cases to determine fiber geometries used later for computer simulations.

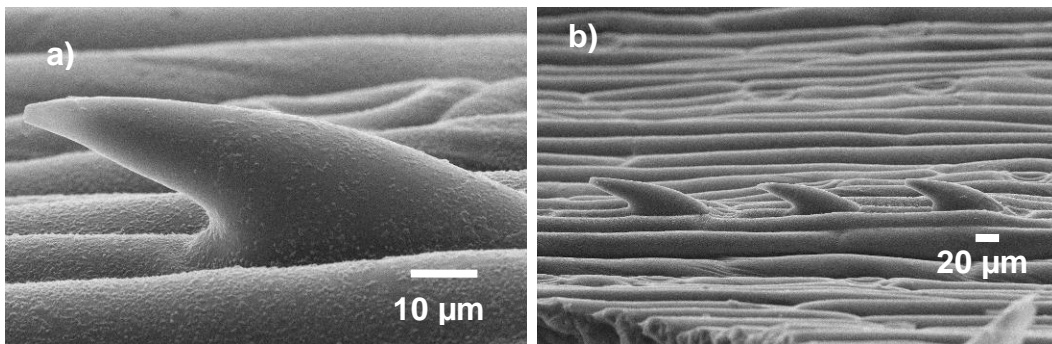


**Figure 4.9:** gold coated polystyrene close up of a replica of *Agropyron repens* (grass); a) micro thorns thorn showing nanoscale fidelity b) array of three thorns.

As discussed in chapter 2, Kraton G1657 was chosen as a thermoplastic material as it gave good replication fidelity and adhesion results. Single fiber fabrication was performed (similar to test sample preparation in chapter 2) by

placing a glass slide onto a hot plate at 200°C and placing a single Kraton pellet onto the glass. The single fiber desired for replication was located visually by inspecting the mold and choosing the label corresponding to various fiber sizes (fibers are large enough to be visually seen on the mold). Once the desired fiber was located, it was carefully placed onto the preheated Kraton pellet and a glass slide was placed on top of the silicone mold. A small 50 gram circular weight was balanced on top of the glass slide, above the Kraton pellet and held for 10-15 seconds. This step gave improved results as the polymer was slowly heating and allowed to flow into the micro cavity. The initial high center point of the pellet causing increased pressure at the cavity location and the relatively high gas permeability of the silicone allows this process to be done without vacuum degassing. A 5 kg weight was then slowly released onto the 50 gram weight over a 10 second period. Once the weight was fully resting on the hotplate, it was carefully kept in place for approximately 30 seconds. Both weights are then removed and the glass slides with the silicone mold and Kraton in between are removed from the hotplate to cool. The top glass slide was then removed (without de-molding the polymer), followed by careful de-molding by peeling the silicone mold from the bottom glass slide (leaving the Kraton sample on the slide). Figure 4.10 shows the results of selected fabricated fibers demonstrating the wide range of geometries possible with this method.

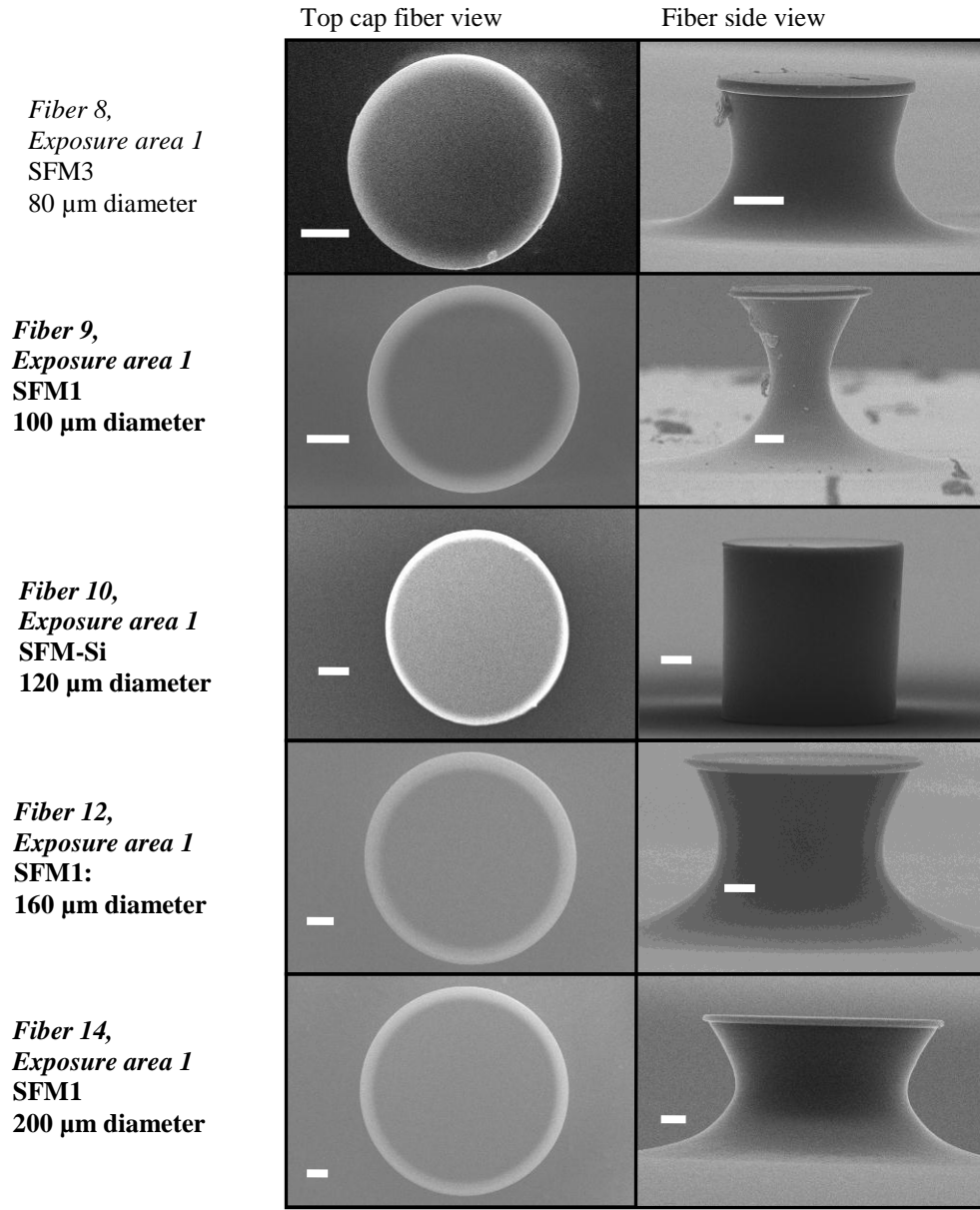


**Figure 4.10: SEM images of Kraton replications of five different fibers, chosen as a wide range of geometric shapes. All fibers were gold coated to allow viewing without charging effects. 100 $\mu\text{m}$ , 120  $\mu\text{m}$  cylinder,  $\mu\text{m}$ , 160  $\mu\text{m}$ , and 200  $\mu\text{m}$  diameter fibers (description in bold above) were tested in chapter 5. Scale bars represent 20  $\mu\text{m}$ .**

## 5 ADHESION TESTING

### 5.1 Introduction

Dry adhesive materials are commonly tested using a hemispherical indenter to avoid alignment issues with flat surfaces [11,50]. While this method provides a good estimate of the overall strength of the adhesive, it cannot provide accurate force vs. displacement information and as the curved indenter will reflect light, the adhesion surface cannot be viewed in real time without distortion. To verify results obtained from FEA simulations and better understand the adhesion surface boundary conditions, a single fiber test was required. By testing large, individual fibers, alignment was less crucial than with an array of fibers, allowing the use of a flat adhesion surface to view the fiber cap during the test. Using individual fibers also makes it possible to directly compare results from this chapter with FEA results<sup>4</sup>.

This chapter describes the single fiber test system developed for this work, provides guide as a user manual for future work with this system in the lab, and compares results obtained for pure axial elongation, shear loading, and time dependent loading with FEA results from the model in chapter 3. The frictional interface is also analyzed by testing adhesion on different substrates. The

---

<sup>4</sup> An adaption of sections from this chapter was presented at the 2014 Adhesion Society Annual Meeting in San Diego California [95].

LabView VI code used to run the system was a modification of the version developed previously by Brendan Ferguson [19].

## 5.2 Single Fiber Test System

The goal of this section was to develop a method to accurately measure force vs. displacement characteristics of different single adhesive fibers fabricated in chapter 4. As previously our lab only had a hemispherical probe indenter fiber array tests system, a new system had to be designed. Figure 5.1 illustrates the final design of the test system components. The following sections describe each component in more detail. The test system was operated on a vibration isolation air table to minimize noise in the results.

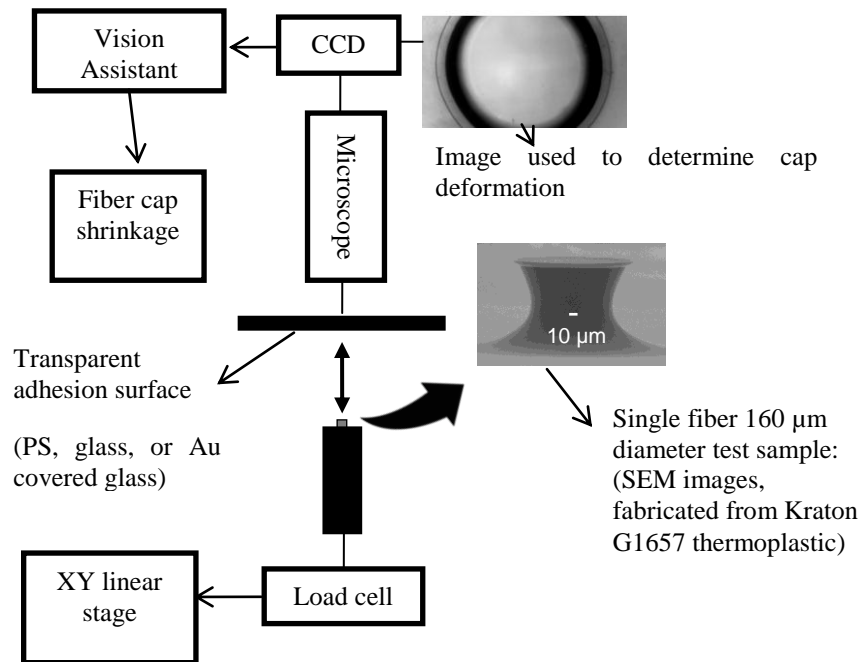


**Figure 5.1: Single fiber test system design layout illustration.**

### 5.2.1 Linear Stage Mount Bracket Design

The first stage of developing the test system was designing a bracket to support the XY linear stages which control the position of the load cell measuring forces on the fiber. A simple design which could support the weight of two linear stages (Newport MFA-CC) and the load cell (Transducer Techniques GSO-25) without any vibration was needed. Taking height measurements from the microscope objective and the linear stages, a three component bracket was designed in Solidworks, see assembly drawing in Figure 5.2. The main constraint was to have a top support level with the table it was attached to. The bottom plate contains four slots which bolt to the air table while allowing slight adjustments to position under the microscope. The top plate has threaded holes to fasten the linear stage. A full Solidworks drawing package submitted to the University of Alberta machine shop for fabrication is included in Appendix D.

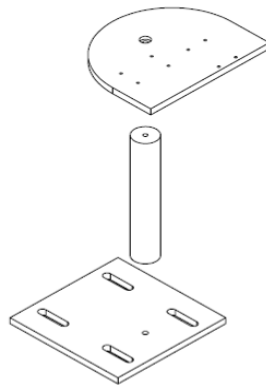


**Figure 5.2: Solidworks assembly drawing of linear stage mount bracket.**

Figure 5.3 shows the final mount bracket fastened to the air table and supporting the linear stages. This design was very stable and caused no noticeable vibrations.

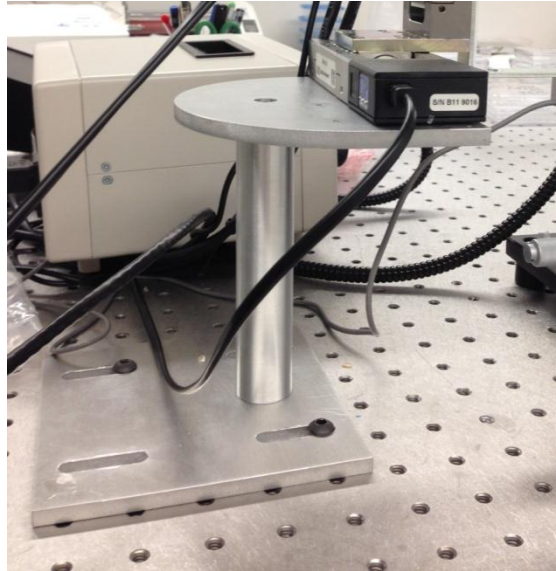


**Figure 5.3: Linear stage mount bracket, final implemented design.**

### 5.2.2 Microscope and Camera Assembly

A MEMS test station microscope provided by Canadian Microelectronics Corporation (CMC) was used for the single fiber test system due to its narrow depth of focus allowing inspection of the fiber cap adhesion interface. The system came with a microscope tube mounted on a plate and a sample inspection block mounted on a three axis, manually controlled stage. The versatile stage design allowed a re-assembly with the three axis stage underneath the microscope tube (Figure 5.4), giving fine control in three dimensions of the microscope objective. This was extremely important as finding the single fiber while physically moving the entire microscope proved almost impossible.

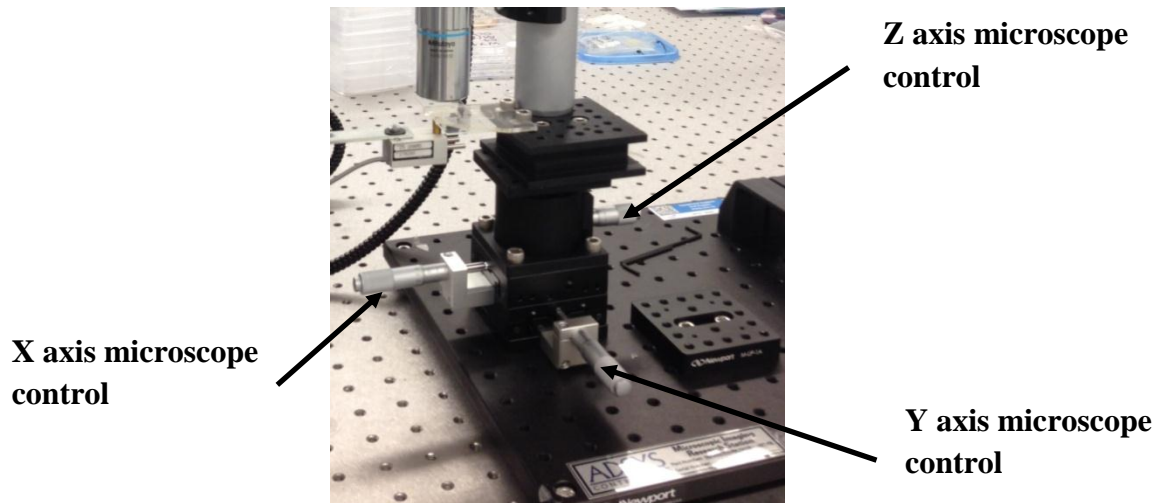


**Figure 5.4: Single fiber test system: microscope three axis position control.**

A 50x objective was used with the microscope as well as a 12x digital zoom. The focus and digital zoom was adjusted with computer software by two servo motors on the microscope, connected to a motor controller. As the servo motors were directly connected to the microscope tube, operating the servos during testing caused significant vibration. The fiber was recorded during testing using a Basler (acA2000-50gc) CCD camera at 25 frames per second.

### 5.2.3 *Adhesion Surface*

The single fiber tests system allowed for adhesion trials with multiple adhesion surfaces. This was attractive for investigating the effect of surface roughness and chemical differences in substrates on the adhesion and adhesion interface behavior, previously not examined. To allow for an exchangeable substrate, a piece of piece of acrylic with a cut out was attached to the microscope

base support. By attaching substrates on top of the acrylic with double sided tape, the fiber probe the fiber contacts only the exchangeable surface, see Figure 5.5.

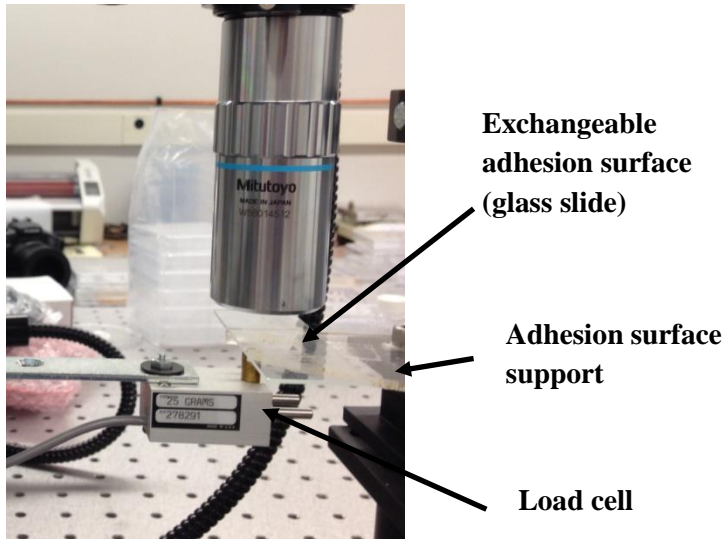


**Figure 5.5: Close up of single fiber test system adhesion surface.**

Surfaces tested included glass microscope slides, Piranha cleaned glass slides, polystyrene (Petri dish), and gold covered glass slides. The roughness of these surfaces were measured with a Zygo optical profilometer (sample surface profile shown in Figure 5.6).

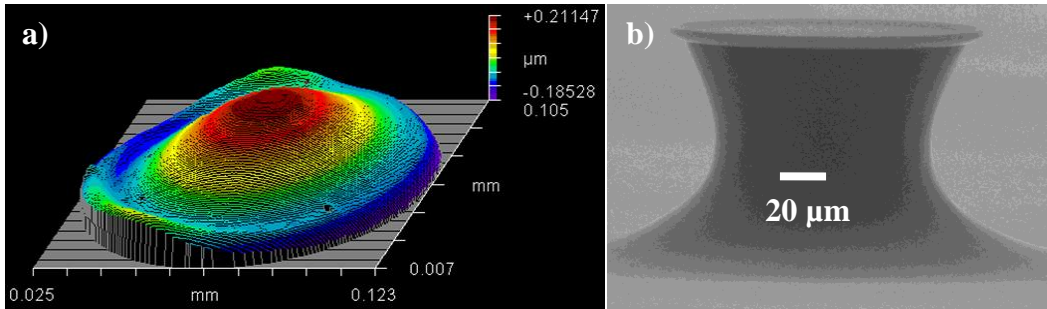


**Figure 5.6:** a) Zygo optical profilometer measurement of Kraton G1657 micro molded dry adhesive pillar cast against TC-5030 silicone, imaged after adhesion testing was performed. Center bulge (~300 nm height) likely due to plastic deformation from pillar elongations. Short distance line scans show  $R_a$  roughness of ~4 nm, b) SEM side view of fiber.

To maintain a transparent surface, the gold sample was prepared by coating a microscope slide with approximately 10 nm of gold using a Denton Sputtering system. This coating allows imaging during adhesion testing but as van der Waals forces become negligible after several nm [4], effectively behaves as a gold surface chemically but should not significantly affect the roughness. Table 5-1 shows the polystyrene surface was an order of magnitude rougher than the other two materials and confirms that the gold coating did not change the glass roughness much.

**Table 5-1:** Contact surface measured roughness determined with a Zygo optical profilometer with ~15  $\mu\text{m}$  line averages.

<i>Material</i>	<i>Roughness, <math>R_a</math> (nm)</i>
Polystyrene	4.9
Glass	~0.4
Gold coated glass	~0.3

#### 5.2.4 Load Cell-Fiber-Probe Assembly

With the microscope and linear stage assembly complete, the load cell needed to be connected to the Y-axis stage and the fiber attached to the load cell such that it can be positioned underneath the microscope. A simple L-bracket from Home Depot was used for the connection as shown in Figure 5.7. The load cell has an attachment point on the top surface which was used to screw in a custom made 6 mm brass cylindrical probe.

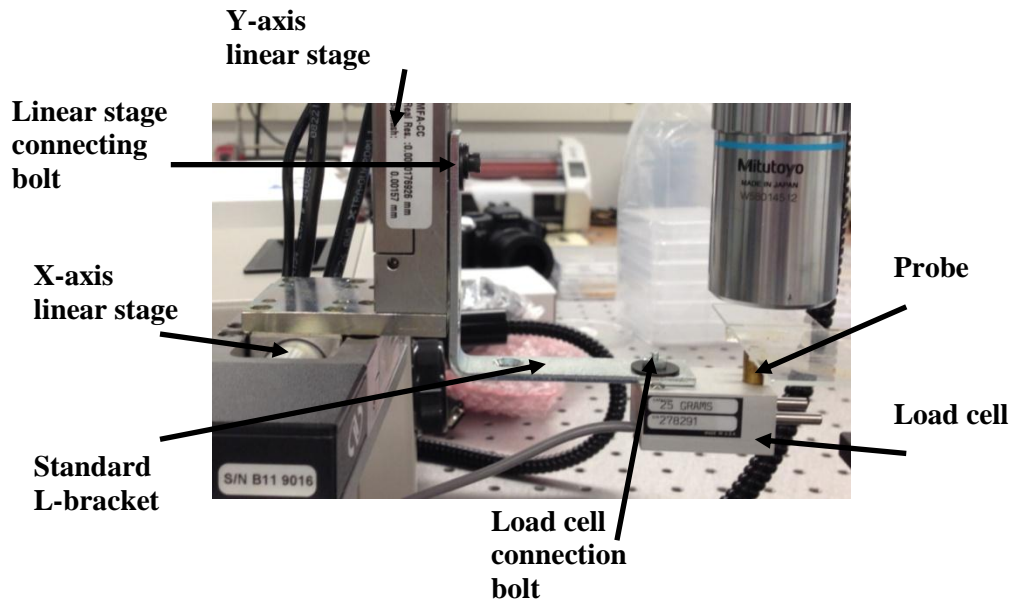


**Figure 5.7: Single fiber test system; load cell to linear stage and probe to load cell connection.**

Adhesive fibers fabricated in chapter 4 then needed to be connected to the probe on the load cell. Fiber casts, as discussed earlier were 5 mm apart, and large enough to view without a microscope. An individual fiber was cut from the cast using a knife. Areas as small as possible, without damaging the fiber, were cut to

limit the risk of the backing layer polymer contacting the adhesion surface before the fiber. A piece of double sided tape was then cut with a knife, smaller than the polymer sample, and placed on top of the brass probe. Using the knife blade, the fiber sample was then carefully attached on the probe, making sure the polymer sample completely covered the double sided tape. Figure 5.8 illustrates the fiber attachment process.

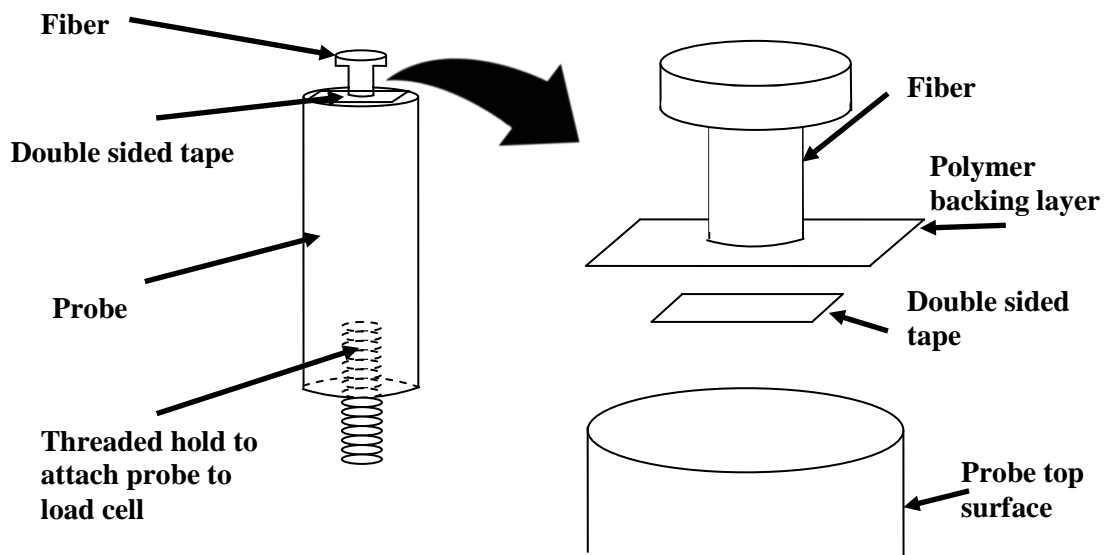


**Figure 5.8: Single fiber test probe and fiber assembly illustration.**

It was found that, as Kraton G1657 samples were softer with thinner backing layers than the polyurethane samples the forces from the fiber were not evenly distributed throughout the fiber base. This caused more localized stress directly underneath the fiber pillar and at times caused this area to come detached from the probe. These fiber detachment failures can be diagnosed by a small reduction in adhesion during the fiber pull-off test. Once this effect was observed,

the camera plane of focus was lowered to the double sided tape and distinct separation of the central polymer sample from the probe while maintaining contact over the rest of the surface was observed.

To prevent the cavitation failure between the fiber backing and the probe, the stress concentration on the surface attached to the double sided tape needed to be reduced. To achieve this improved stress distribution, a simple method was developed using a composite polymer fabrication. The ability of Kraton G1657 to bond with polystyrene was used to fabricate a two part fiber adhesive: a stiffer polystyrene backing layer underneath a thin Kraton backing layer with the adhesive fiber. Polystyrene used was from a petri dish broken into small pieces (~3 mm x 3 mm). Fabrication was done similarly as with original Kraton fibers except the casting was completed upside down. The mold was placed directly onto the hotplate (with mold cavities on the top surface) and the Kraton pellet positioned on top of the fiber which was to be fabricated. The Kraton pellet was slightly flattened with a glass slide but not melted. A small piece of polystyrene was then placed on top of the flattened Kraton pellet, covered with a glass slide, followed by weights. Using this method, no further detachment failures were observed.

#### 5.2.5 Single Fiber Test System Data Analysis

Following a test, two forms of data needed to be analyzed; load cell information, and video images. The adhesion data from the load cell was

automatically recorded during the test at 0.1 second intervals. Video recordings from the CCD camera were taken using a free version of a NCH software, ‘Virtual VCR’. As the camera records in high resolution, files were often in the tens of GB after short recordings. To save data on the hard drive space available, these files had to be compressed.

When analyzing the load cell data, it was required to determine the axial forces on the fiber and the position of the fiber base. While the linear stage output was not set up to record the position, it could be determined based on the input velocity and elapsed time. However, this position represents the linear stage, not the fiber base. To get an estimate of the fiber base position, we have to consider two displacements occurring in series during the test: load cell cantilever deflection (inside the load cell), and actual fiber elongation. Two springs in series will have the same force but different displacements, as described in equation 38:

$$X_{total} = X_{fiber} + X_{cantilever} = \frac{F_{measured}}{k_{fiber}} + \frac{F_{measured}}{k_{cantilever}} \quad (38)$$

Where  $X_{total}$  is the displacement determined from the linear stage controller and  $F_{measured}$  is the load cell output. From this equation, the fiber displacement was found by equation 39:

$$X_{fiber} = X_{total} - \frac{F_{measured}}{k_{cantilever}} \quad (39)$$

The cantilever stiffness ( $k_{cantilever}$ ) was determined by indenting the probe (without a fiber attached) into a hard glass surface 10  $\mu\text{m}$  and measuring the

resulting force, see Figure 5.9. For this test, it was assumed the glass is an infinitely rigid surface that will not contribute to any displacement. This is a valid assumption when comparing the compliance of the load cell with glass stiffness. The result gave a linear force-displacement curve, as expected from a calibrated load cell, from which the stiffness,  $k_{cantilever}$  was determined by measuring the slope. Using the average of three trials, a stiffness of  $k_{cantilever} = 2.54 \text{ N/mm}$  was found. For all results displaced in this work, fiber displacements are calculated using this method.

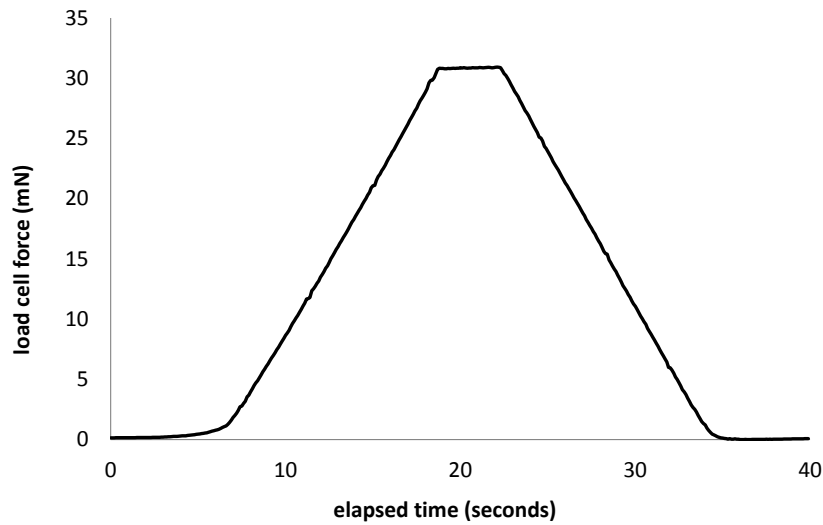


**Figure 5.9: Load cell cantilever stiffness test. x-axis represents elapsed time and, as linear stage was displaced at  $1 \mu\text{m/s}$ , also equal to load cell deflection (direction of motion changes at peak).**

The microscope was always focused on the top cap fiber interface during tests. This allowed viewing of the adhesion interface, useful for determining the FEA boundary condition required. Future work could have the plane of focus on the fiber neck to compare fiber deformations with FEA results. Once recorded, the

videos were analyzed to determine fiber cap shrinkage vs. elongation (using the known video frame rate and the linear stage velocity). Tests with high cap shrinkage were analyzed using a custom pattern matching code developed in Matlab, however, many tests resulted in extremely small displacements in which only sparsely selected images were measured manually.

#### *5.2.6 Operating the Single Fiber Test System*

This section provides an overview of operating the single fiber test system for future users. Figure 5.10 shows the complete test system with all components. To set up a test, the microscope was moved slightly away from the linear stage mount to prevent the load cell from being damaged during handling. Note, when not testing, two pins should always be inserted in the load cell to help prevent damage if accidentally contacted. The probe is removed from the load cell and a small piece of double sided tape is secured on the top surface. After fabricating a desired test sample and cutting to size, the fiber is attached to the load cell. Care must be taken that the polymer sample is as level as possible. When holding the sample against a light, the fiber should be visible and clearly the highest point on the probe. The probe is then screwed back into the load cell without touching the polymer sample. The microscope is re-positioned with the probe in between the cut-out on the substrate mount. At this point the substrate can be replaced with any desired transparent surface. The manual height dial on the microscope is then used to find the top surface of the polymer (several millimeters beneath the adhesion surface to prevent unintended contact). Note, the light source includes a

cooling fan which causes significant vibration and noise in the load cell data. While the light source is shown on the air table in Figure 5.10, during testing it should be placed on a separate table. Using the three axis microscope position control, the fiber is then located (while viewing the image through the *Virtual VCR* software). The rest of the test is then controlled from a computer through the *SingleFiberTest.vi* LabView program, the *Virtual VCR*, and the motor controller software.

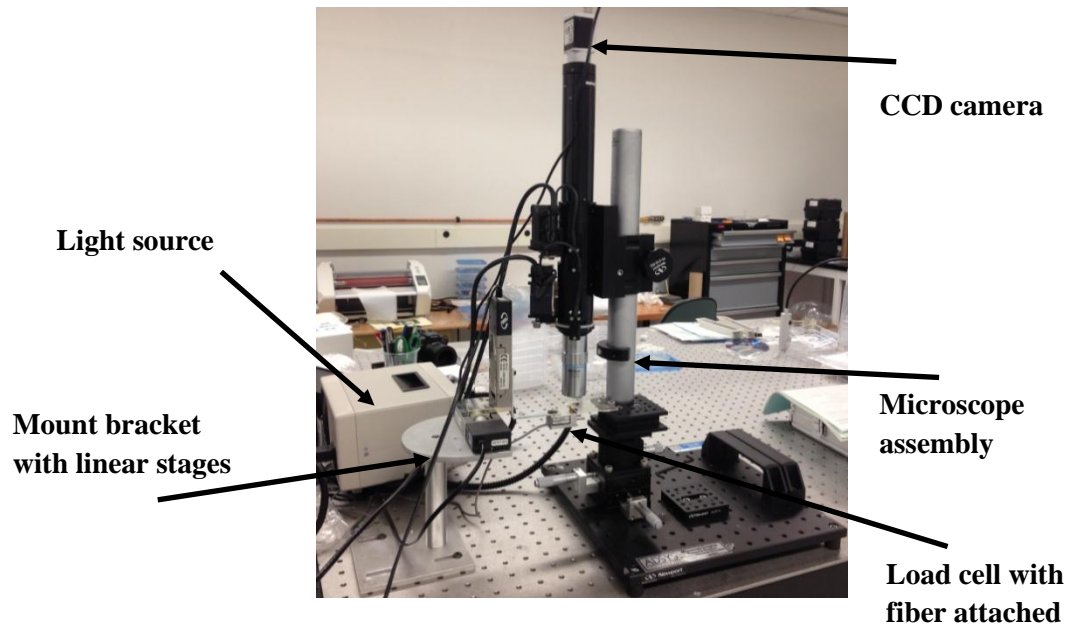


**Figure 5.10: Complete single fiber test system.**

### 5.3 Adhesion Results

The method described in the previous section of this chapter were used to test multiple fiber shapes and the three polymer materials discussed in chapter 2 (Kraton G1657, ST-1060, and ST-1087). Fibers with 100  $\mu\text{m}$ , 160  $\mu\text{m}$ , and 200

$\mu\text{m}$  diameter with overhanging cap (*cast from SFM1 exposure area 1*), as well as a  $120\ \mu\text{m}$  diameter straight cylinder shape SU-8 structures cast from the silicon substrate (exposure area 1) were tested. In addition to testing different fibers, three different adhesion surfaces were also examined. This section summarizes results achieved for these single fiber adhesion tests and provides comparisons with the FEA model developed in chapter 3.

Unlike a hemispherical indenter array test (for which as preload magnitude increases, more fibers will come in contact with the indenter), the single fiber test system would ideally be insensitive to preload. However, due to small imperfections in the fiber and adhesion material, higher preload gives slightly improved adhesion consistency due to an improved contact with the fiber cap. Figure 5.11 shows how between 0.1 mN and 2 mN preload, the adhesion remains constant at about 2.7 mN.

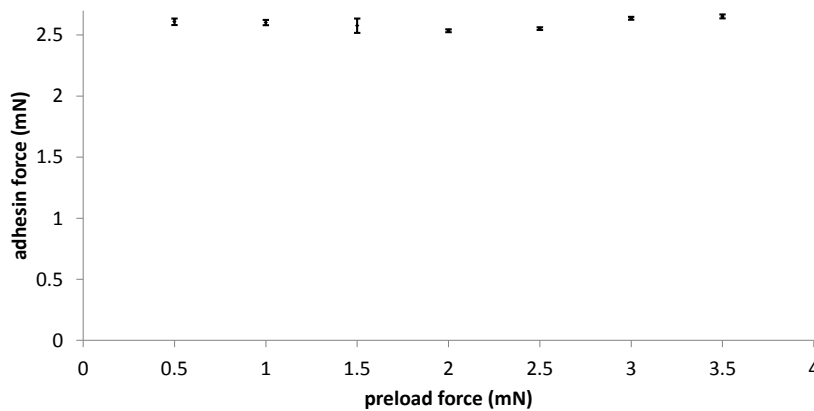


**Figure 5.11: Single fiber ( $100\ \mu\text{m}$  Kraton G1657 on polystyrene adhesion surface) preload test.**

Based on the preload vs. adhesion test, a preload of 1 mN was chosen for the rest of the experiments to give more consistent results without compressing the fiber extensively, potentially causing damage.

Another parameter affecting the adhesion results was the time at which the fiber was held at the preload force before withdrawing. Keeping the fiber pressurized against the adhesion surface allows the polymer to achieve more intimate contact, increasing the van der Waals attraction force. To determine the increase in adhesion which could be achieved by longer contact periods, multiple trials were run while varying the contact time from 1 second to 8 minutes. Each data point was repeated three times to get an average and standard deviation. Figure 5.12 shows a consistent increase in adhesion from 2.77 mN at 1 second to 3.97 mN at 8 minutes contact time. The increase in adhesion seems to be most significant during the first 60 seconds, likely due to the viscoelasticity of the fiber; as from chapter 2, the slowest measured time constant was on the order of ~60 seconds for Kraton G1657. The viscoelasticity of the material allows the fiber to relax and achieve more conformal contact by keeping the preload pressure applied for the first 60 seconds. Past 60 seconds, viscoelastic effects are not expected to be significant from results in chapter 2, therefore further conformal relaxation occurs, at a slightly slower rate.

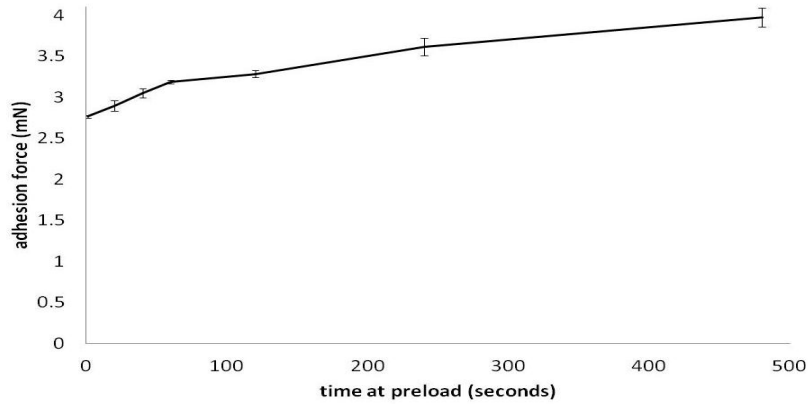


**Figure 5.12: Time at preload vs. adhesion force results (for 100  $\mu\text{m}$  Kraton G1657 on polystyrene adhesion surface).**

For further tests performed, a standard preload relaxation time of 5 seconds was chosen. This phenomenon should be considered with any adhesion data, as results could be improved by longer preload wait periods, or diminished by reducing the time. Adhesion results will be focused on 100  $\mu\text{m}$ , 160  $\mu\text{m}$  and 200  $\mu\text{m}$  diameter overhanging cap fibers and a 120  $\mu\text{m}$  straight cylinder post. Each graph shows a small SEM image of the fiber from which the results were obtained. The focus on the results shown was on the stress-elongation profile, not the total adhesion force. Due to extreme sensitivity to dust particles or small defects on the fiber cap, maximum adhesion forces show significant variation between experiments.

### 5.3.1 *Normal Loading*

Examining the stress-elongation properties of the fibers during axial elongation allows the comparison of different shapes for the following properties:

general adhesion strength, material yield due plasticity, and fit to the COMSOL model developed in chapter 3. Results for each graph a reported from a single fiber sample tested multiple times (one test extends from preload to adhesion failure). However, multiple fibers were cast showing good repeatability of the force-strain response for new samples. All tests shown were performed at 5  $\mu\text{m/s}$  probe velocity. The results for normal loading using the three polymers and four fiber shapes are given in Figure 5.13-Figure 5.20. Note, maximum adhesion was inconsistent due to defects in a fiber cap or dust contamination. These results should mainly be used to analyze the force-elongation curves.

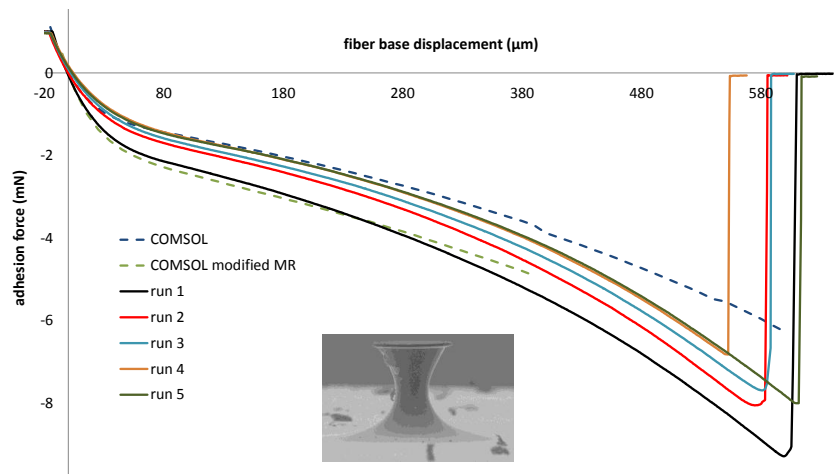


**Figure 5.13: 100  $\mu\text{m}$  diameter Kraton G1657 single fiber adhesion (run 1-5) compared to two FEA model results with fixed cap boundary condition.**

As the COMSOL model underestimated the stiffness of the fiber, the Mooney Rivlin constants were modified to give a better fit (COMSOL modified MR model), see Table 5-2 for modified constants used.

**Table 5-2: Modified Mooney Rivlin constants used to account for polymer chain alignment and biaxial loading. Negative values required for fit but may cause instabilities for some loading conditions.**

Material	$C_1$ (kPa)	$C_2$ (kPa)	$C_3$ (kPa)	$C_4$ (kPa)	$C_5$ (kPa)
<b>Kraton G1657</b>	-19.5	732	2.80	58.8	-17.5
<b>ST-1060</b>	650	250	0	0	0
<b>ST-1087</b>	500	1000	0	0	0

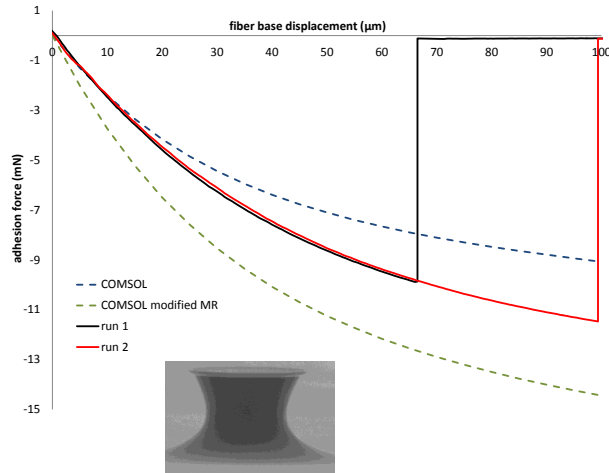


**Figure 5.14: Kraton G1657 160 μm diameter fiber single fiber adhesion (run 1-3) compared to FEA model result with fixed cap boundary condition.**

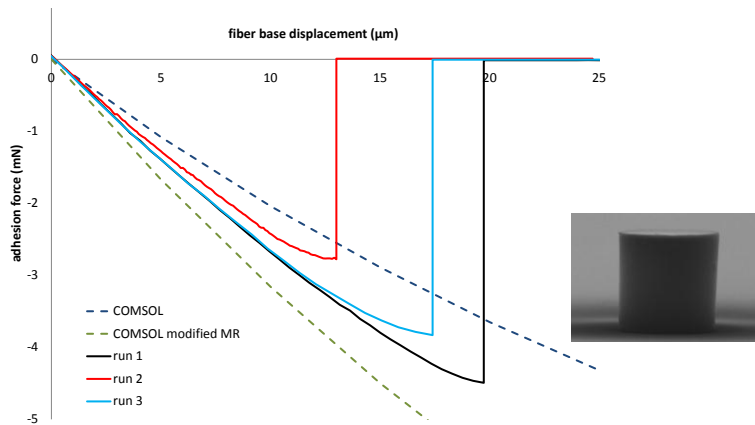


**Figure 5.15: Kraton G1657, 120 μm diameter straight cylinder post fiber single fiber adhesion (run 1-3) compared to FEA model result with fixed cap boundary condition.**

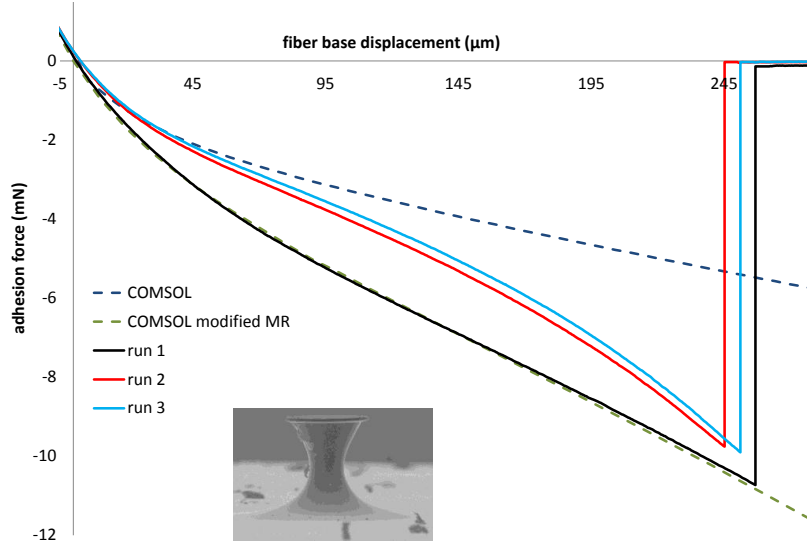


**Figure 5.16: ST-1060, 100 μm diameter fiber single fiber adhesion (run 1-3) compared to FEA model result with fixed cap boundary condition.**

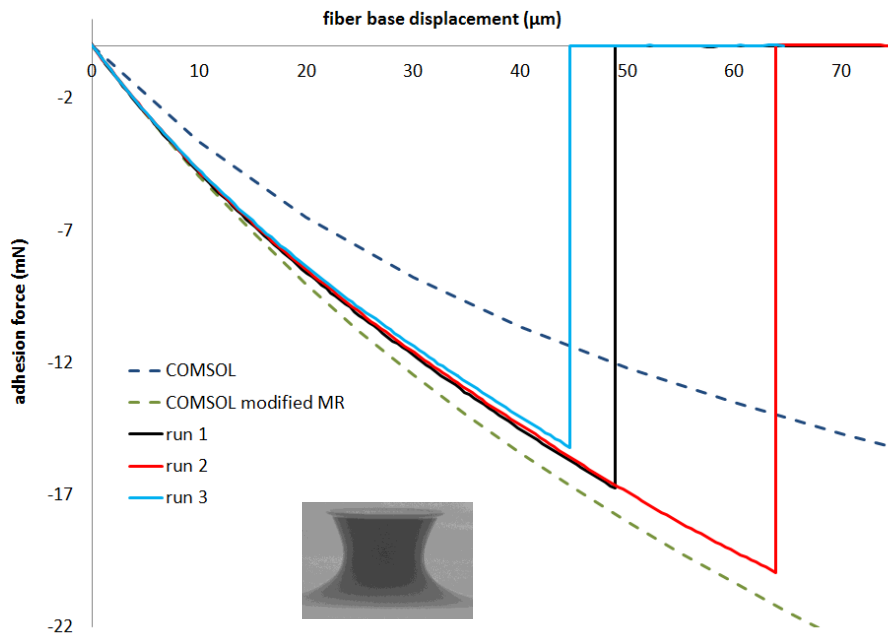


**Figure 5.17: ST-1060, 160 μm diameter fiber diameter fiber single fiber adhesion (run 1-3) compared to FEA model result with fixed cap boundary condition.**

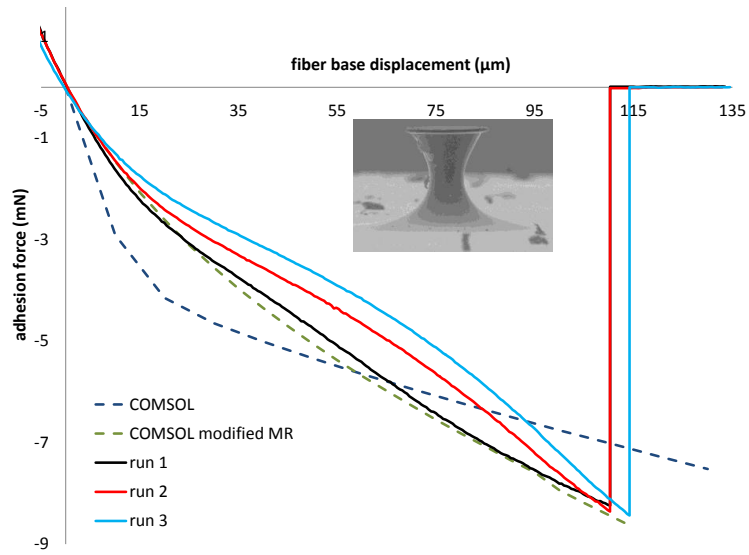


**Figure 5.18: ST-1087, 100  $\mu\text{m}$  diameter single fiber adhesion (run 1-3) compared to FEA model result with fixed cap boundary condition.**

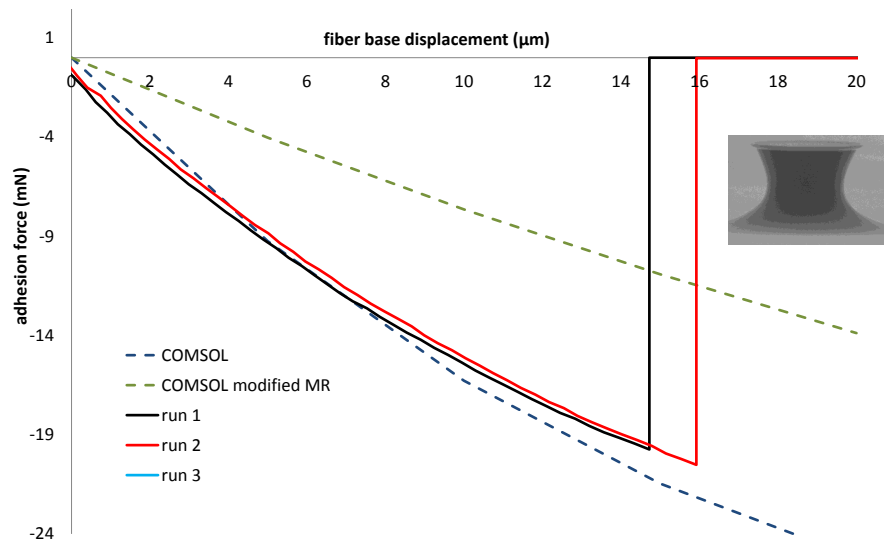


**Figure 5.19: ST-1087, 160  $\mu\text{m}$  diameter fiber diameter fiber single fiber adhesion (run 1-3) compared to FEA model result with fixed cap boundary condition.**

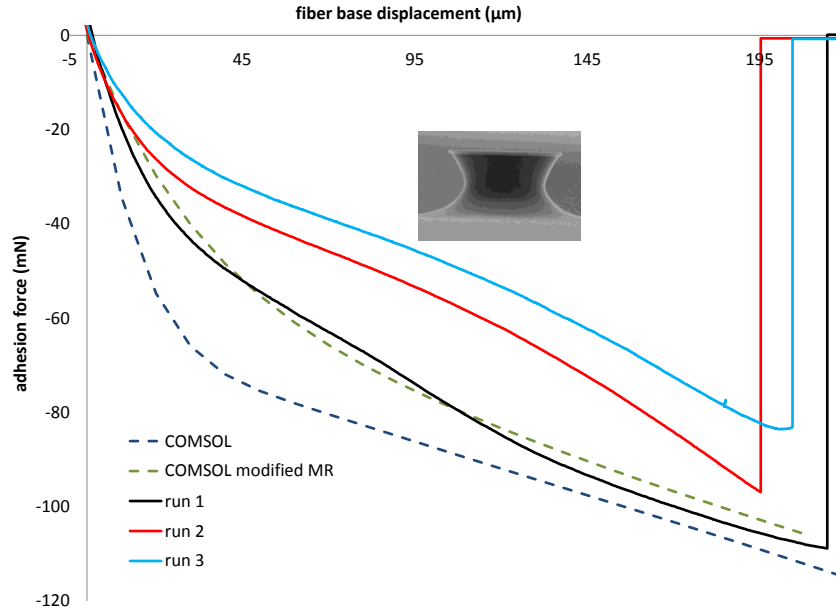


**Figure 5.20: ST-1087, 200  $\mu\text{m}$  diameter fiber diameter fiber single fiber adhesion (run 1-3) compared to FEA model result with fixed cap boundary condition.**

For Kraton G1657, the 100  $\mu\text{m}$  (Figure 5.13), 120  $\mu\text{m}$  (Figure 5.14), and 160  $\mu\text{m}$  fiber (Figure 5.15) were tested. All results show the COMSOL model with a Mooney Rivlin data fit from Instron bulk material experiments giving a consistently softer result than experimental values. For the Kraton G1657 thermoplastic material, this discrepancy may be due to flow induced polymer chain alignment during molding into the micro cavities [96,97]. However, thermoset material in this work also show the same trend, suggesting another factor in the stiffer than expected fibers. The Mooney Rivlin model developed in chapter 2 shows excellent fit with the COMSOL simulation of the bulk test samples, however, these (rectangular) samples undergo mainly uniaxial

deformations, in agreement with the assumptions made in the model development. The complex 3-dimensional shaped fiber would on the other hand show significant shear as well as axial deformations even for pure axial fiber base elongations. Uniaxial tests have been shown to underestimate the material stiffness, especially in cases where biaxial loading exists [98], suggesting this may be the cause of the model disagreement. Options to achieve more accurate material data would include using a biaxial test to obtain stress-strain data, or use the micro-fiber tests and the COMSOL model to iteratively determine the constants which would provide an accurate fit. Kroner [53] suggested a similar approach, using a single micro fiber test to determine material properties of PDMS. Figure 5.13 shows runs 1 – 5 for the Kraton 100  $\mu\text{m}$  fiber, with significant yield (softening) in the force curve until a converged material force-displacement curve after 4 cycles. Two COMSOL models are also displayed, one showing softer results than experiment data (using Mooney Rivlin parameters from the bulk material testing), and one obtained by iteratively determining Mooney Rivlin parameters using COMSOL to closely match the run 1 trial. The values of the modified Mooney Rivlin constants for all materials used in the following results are given in Table 5-2.

Results for the 160  $\mu\text{m}$  Kraton G1657 fiber in Figure 5.14 show almost negligible material yield due to less elongation with the lower aspect ratio fiber. The FEA simulation was again slightly softer than experimental results while the modified Mooney Rivlin simulation (fit to the 100  $\mu\text{m}$  fiber) now overestimates

the stiffness. This may be due to the larger fiber causing less chain alignment and giving a softer material.

The straight cylinder fiber was tested to show the improvement an overhanging cap makes on adhesion of microfibers, showing much lower adhesion forces than the smaller 100  $\mu\text{m}$  undercut fiber. The straight pillar causes stress concentrations at the edges of the pillar and makes it extremely vulnerable to peel failure. Results for this fiber, in Figure 5.14, are quite variable due to the tilt alignment dependency of the adhesion [54], difficult to control with the single fiber test system. The modified model again slightly overestimates the stiffness as in the 160  $\mu\text{m}$  case, possibly due to different amount of chain alignment for different fiber sizes.

Results for ST-1060 fibers (100  $\mu\text{m}$  and 160  $\mu\text{m}$  diameters, Figure 5.16 and Figure 5.17 respectively) showed similar results to the Kraton fiber, with significant yield in the first few cycles for the 100  $\mu\text{m}$  and more constant results with the 160  $\mu\text{m}$  fiber. Adhesion forces are slightly higher with less elongation due to the stiffer material properties of ST-1060. The 100  $\mu\text{m}$  diameter fiber in Figure 5.16 was used to fit a modified Mooney Rivlin model to better fit the experimental results.

By using the modified Mooney Rivlin constants in the 160  $\mu\text{m}$  diameter fiber, the displacement can be predicted relatively well. This suggests that for ST-

1060, the errors in simulation are due to lack of complete biaxial experimental data.

Results for three fibers with ST-1087 with fixed cap boundary conditions are shown (100  $\mu\text{m}$ , 160  $\mu\text{m}$ , and 200  $\mu\text{m}$  diameter in Figure 5.18, Figure 5.19, Figure 5.20 respectively). The 100  $\mu\text{m}$  fiber shows yield with no convergence within the five cycles completed while the 160  $\mu\text{m}$  fiber shows basically no plastic deformation. The 200  $\mu\text{m}$  fiber achieved extremely high adhesive forces, with a maximum of 3.5 MPa adhesion pressure. This result was likely due to the fiber containing less fabrication defects. The extremely high adhesion force for 200  $\mu\text{m}$  fiber caused large elongations (200 %) for a very low aspect ratio (1 : 0.6) shape. This high strain caused significant material yield, with each successive run giving softer results.

Unlike the other materials, ST-1087 fibers showed FEA results with closer agreement or even slightly stiffer results for portions of the elongation. A modified Mooney Rivlin constant was again fit to the 100  $\mu\text{m}$  fiber as show in Figure 5.18. Using the modified Mooney Rivlin fit found with the 100  $\mu\text{m}$  fiber for the 160  $\mu\text{m}$  fiber significantly underestimates forces (Figure 5.19), while for the 200  $\mu\text{m}$  fiber (Figure 5.20) fits quite well. The inconsistency for the 160  $\mu\text{m}$  fiber was likely due to the extremely short elongation before detachment in Figure 5.19. While the Mooney Rivlin fit was modified to match the 100  $\mu\text{m}$  fiber behavior, showing over 100  $\mu\text{m}$  elongation, the 160  $\mu\text{m}$  diameter fiber failed after only  $\sim 15$   $\mu\text{m}$  elongation. This data does not cover a long enough elongation range

to judge agreement to the general fit of over 100  $\mu\text{m}$  elongation. The 200  $\mu\text{m}$  diameter fiber fabricated happened to be extremely “clean” and defect free, resulting in extremely high adhesion forces and elongations.

The normal loading tests demonstrated several results, important in modeling and designing dry adhesive fibers. The higher aspect ratio fibers (100  $\mu\text{m}$  diameter and 118  $\mu\text{m}$  tall) showed significant softening for consecutive trials on the same fiber. Larger diameter fibers (same height) had less elongation before adhesion loss, minimizing the material yield. This should be accounted for when designing robust fibers. The COMSOL model developed in chapter 3 gave an underestimate of stiffness in most cases, possibly due to the assumption of uniaxial loading for relatively short fibers. The Mooney Rivlin constants found from bulk testing were modified to fit one size fiber (100  $\mu\text{m}$  diameter) and used to predict the other sizes. In both ST-1060 and ST-1087 the modified model was able to well predict forces in different fibers. For Kraton, the modified model still did not give accurate predictions, suggesting that in addition to a biaxial stress state, the thermoplastic fiber may have varying degrees of polymer chain alignment in the different sized fibers.

### 5.3.2 Relaxation Tests

Similar to bulk material stress relaxation tests performed in chapter 2, axial tests with rapid elongation (100  $\mu\text{m/s}$ ) until 60  $\mu\text{m}$  followed by observation of the reduction in stress was performed for single fibers. Figure 5.21 shows the

full force vs. elongation data for the Kraton G1657 160  $\mu\text{m}$  fiber. These results are compared to FEA simulation using the linear viscoelastic model developed. Using data obtained for 100% bulk material strain significantly overestimates the forces in the fiber. However, due to the smaller neck dimensions, the maximum strain expected from the COMSOL simulation was 1.56. Using the 150% elongation parameters for the Maxwell viscoelastic model provides a much better approximation.

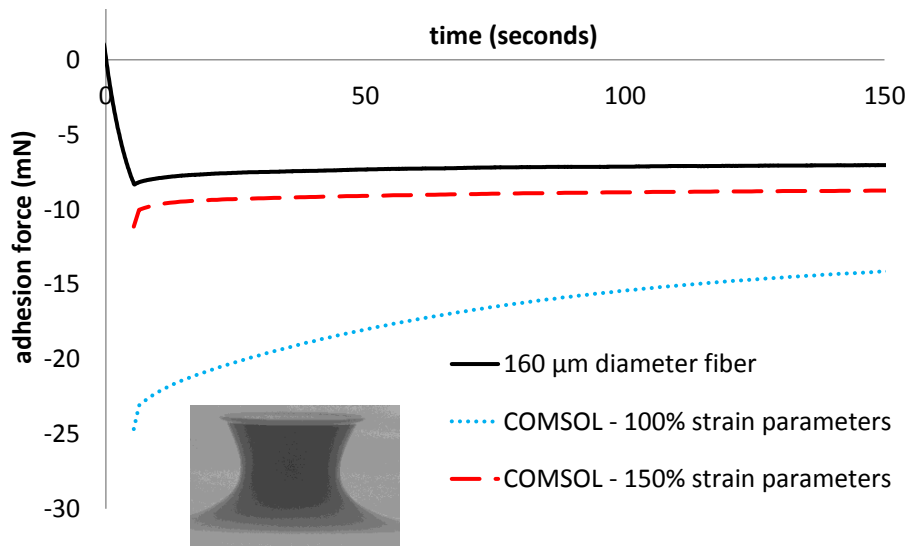


**Figure 5.21: Relaxation tests for Kraton G1657 160  $\mu\text{m}$  fiber, experimental vs. FEA.**

The relaxation section of the curve in Figure 5.21 was difficult to examine as the magnitude of total adhesion was much larger than the relaxation component. Figure 5.22 shows a close up of the relaxation portion, comparing the experimental single fiber tests with the Instron bulk sample tests described in chapter 2. Forces are normalized to give a comparison to the samples with

different dimensions. The results show that the single fiber test did not capture the first time constant with rapid stress relaxation, resulting in stiffer curve. This can be expected by comparing the strain rate between Instron and single fiber tests ( $83.3 \text{ min}^{-1}$  for bulk and  $50.8 \text{ min}^{-1}$  for micro scale tests). As the single fiber tests did not elongate quick enough, neglecting the first time constant, Figure 5.22 provides a good fit; demonstrating that viscoelastic properties remain the same at the bulk and micro scale for these materials.

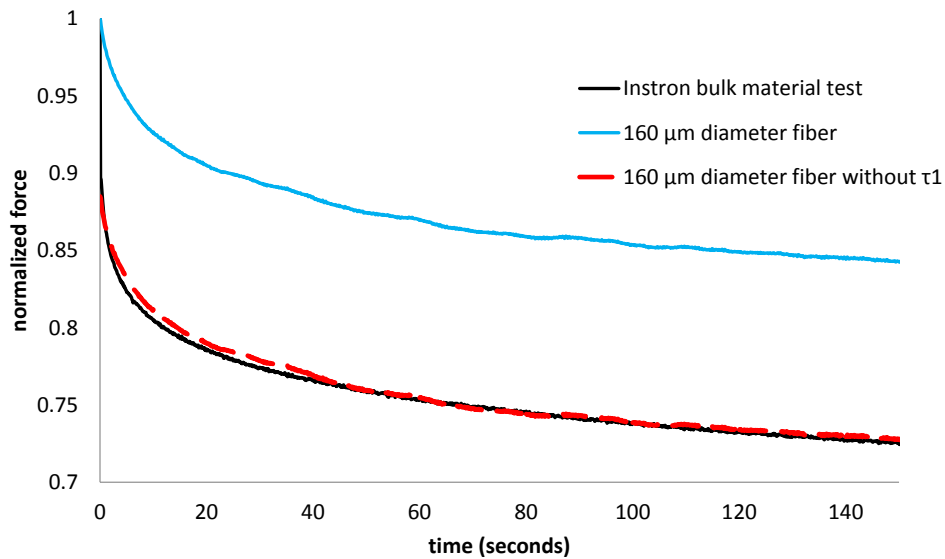


**Figure 5.22: Normalized force from relaxation tests, comparing single fiber adhesion tests to Instron bulk material tests.**

### 5.3.3 *Shear*

While the shear forces on a fiber could not be determined with the single load cell setup used, shear could be applied while recording the effect on the normal forces. See illustration in Figure 5.23 for the test method used for shear.

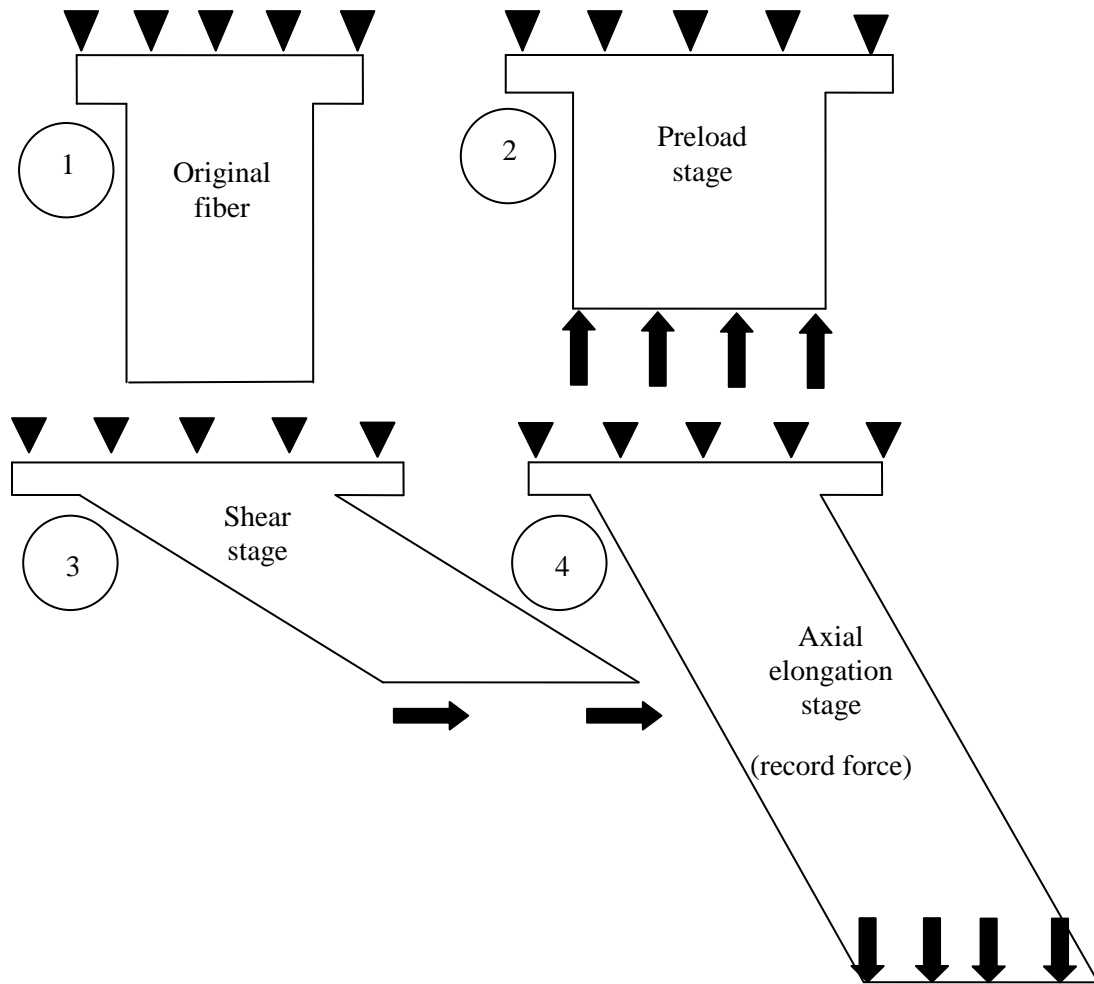


**Figure 5.23: Shear tests method illustration: (1) represents the original undeformed fiber, (2) shows the axial preload stage (1 mN), (3) shows the pure shear deformation, and (4) gives the final axial elongation until adhesion was lost (this was the stage from which load cell data is given in the next figures).**

Using the test method illustrated in Figure 5.23, 100  $\mu\text{m}$  and 160 $\mu\text{m}$  Kraton G1657 fibers, force vs. elongation data from pure axial elongation is compared to fibers which were first sheared. Both fibers were given the maximum shear displacement they could withstand before adhesion failure (460  $\mu\text{m}$  for the

100  $\mu\text{m}$  fiber and 90  $\mu\text{m}$  for the 160  $\mu\text{m}$  fiber, Figure 5.24 and Figure 5.25 respectively.

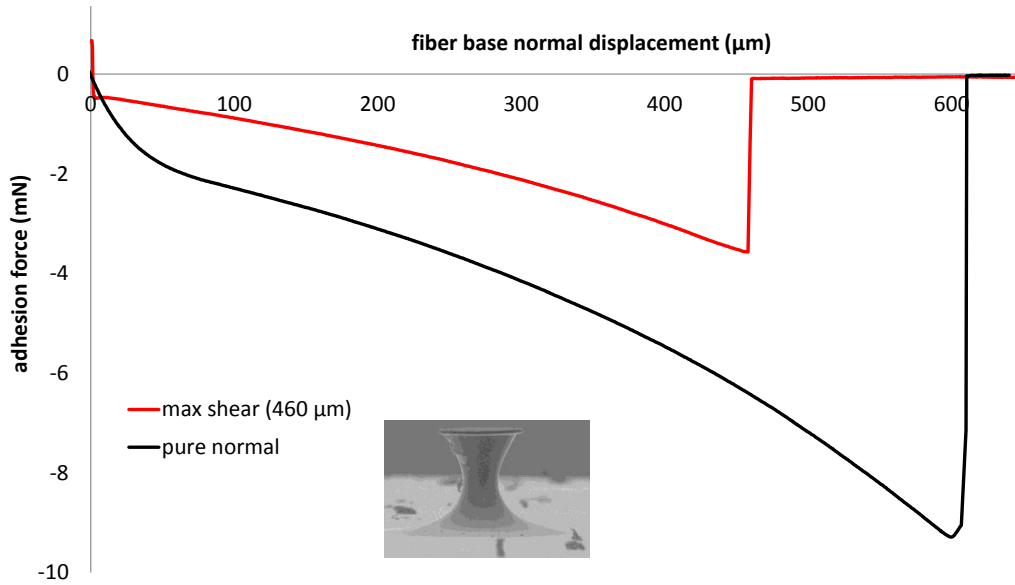


**Figure 5.24: Kraton G1657 100  $\mu\text{m}$  fiber showing axial load cell forces from a 460  $\mu\text{m}$  sheared fiber and pure axial pull back.**

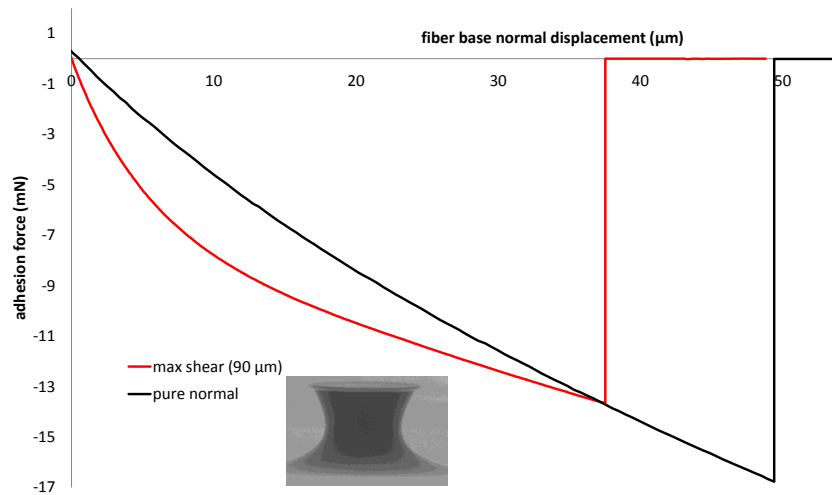


**Figure 5.25: Kraton G1657 160  $\mu\text{m}$  fiber showing axial load cell forces from a 90  $\mu\text{m}$  sheared fiber and pure axial pull back.**

The results for the 160  $\mu\text{m}$  fiber are as expected, showing higher forces vs. normal elongation for the shear case than pure normal loading (as the fiber was already sheared 90  $\mu\text{m}$ , giving a larger net displacement). The 100  $\mu\text{m}$  fiber however shows less force for the case with prior shear load than with only an axial elongation. This effect was due to the large amount of cap sliding (several hundreds of microns) which occurs at the adhesion interface for these high shear values.

#### 5.3.4 *Frictional Interface Analysis*

To gain a better understanding of the adhesion interface and frictional parameters which might be used for FEA simulation for the fibers manufactured the effect of different adhesion substrates was examined. Three materials were chosen: polystyrene, glass, and gold. Axial adhesion tests were shown for the three adhesion substrates with all three fiber materials using the 160  $\mu\text{m}$  diameter fiber. Tests were performed at 1  $\mu\text{m/s}$  second as cap shrinkage often was only observed with slow pull off speeds.

Kraton G1657, ST-1060, and ST-1087 (Figure 5.26, Figure 5.27, and Figure 5.28 respectively) all show that the normal forces vs. elongation are identical for each adhesion surface with slight variations in the maximum force attained. The maximum adhesion force was inconsistent among the three materials and was mostly dominated by surface contamination or dust. While the normal adhesion vs. displacement was identical, the friction properties for the

substrates was significantly different, with polystyrene and gold giving pinned conditions and glass permitting the cap to shrink for slow pull of speeds. This result was consistent with FEA simulations predicting that fixed and roller cap will have identical normal force vs. elongation behavior.

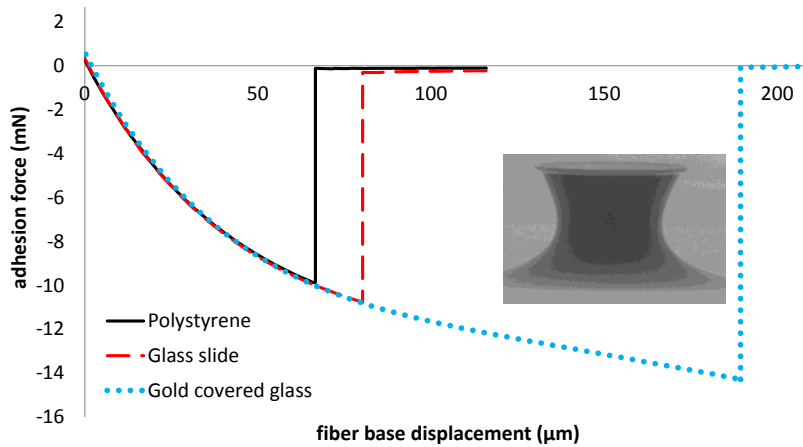


**Figure 5.26: Axial elongation results for Kraton G1657, 160  $\mu\text{m}$  fiber with three different adhesion surfaces.**

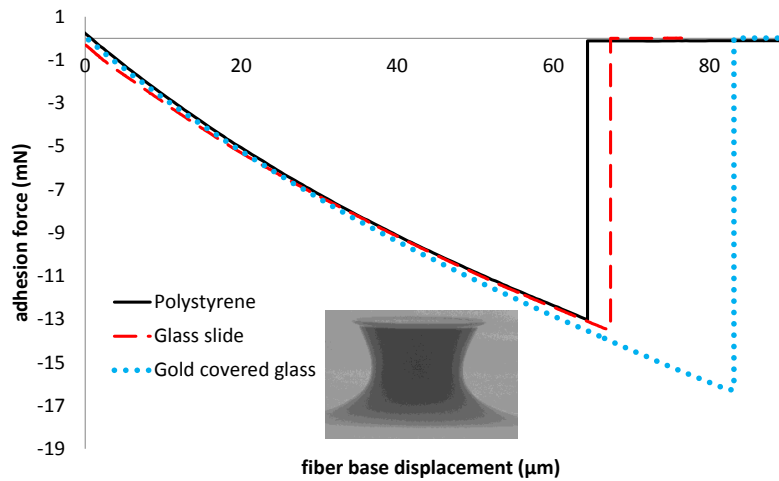


**Figure 5.27: Axial elongation results for ST-1060, 160  $\mu\text{m}$  fiber with three different adhesion surfaces.**

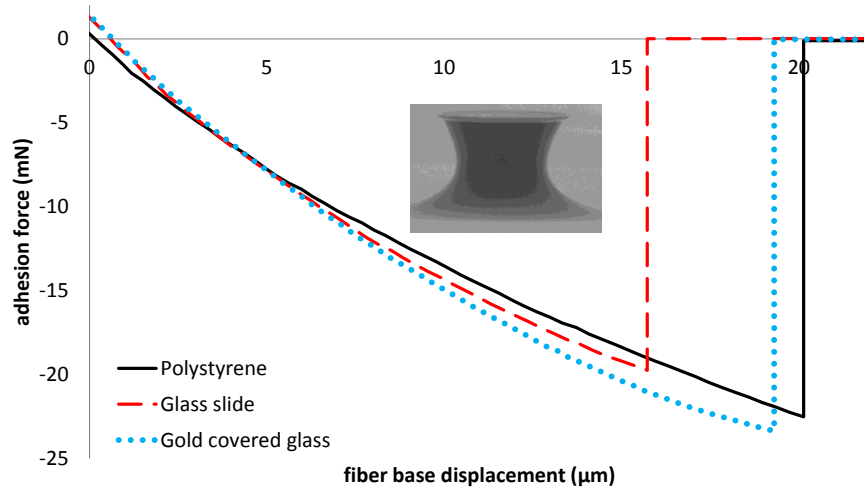


**Figure 5.28: Axial elongation results for ST-1087, 160  $\mu\text{m}$  fiber with three different adhesion surfaces.**

Sample results for fiber cap shrinkage for Kraton G1657 100  $\mu\text{m}$  and 160  $\mu\text{m}$  fibers (Figure 5.29 and Figure 5.30 respectively) are compared to examine the effect of shape on cap shrinkage. Tests were performed at 1  $\mu\text{m/s}$  pure axial elongation with a glass adhesion substrate. Results showed that the 100  $\mu\text{m}$  fiber only had  $\sim 2.5\%$  cap diameter shrinkage at the maximum fiber base elongation while the 160  $\mu\text{m}$  fiber displayed  $\sim 20\%$  cap diameter shrinkage. This can be explained by the lower aspect ratio of the 160  $\mu\text{m}$  fiber causing greater transverse contraction forces as a result of the elongation. These results were however not very reproducible with variables such as: dust particles, material defects, and pull back speed, effecting the total fiber base elongation which was attained and the cap shrinkage significantly.

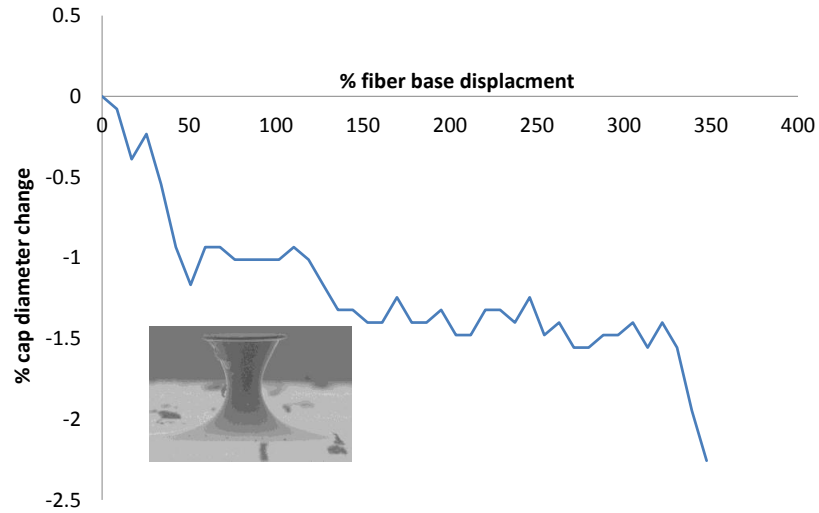


**Figure 5.29: Fiber cap shrinkage tests for Kraton G1657, 100  $\mu\text{m}$  diameter fiber on glass adhesion substrate.**

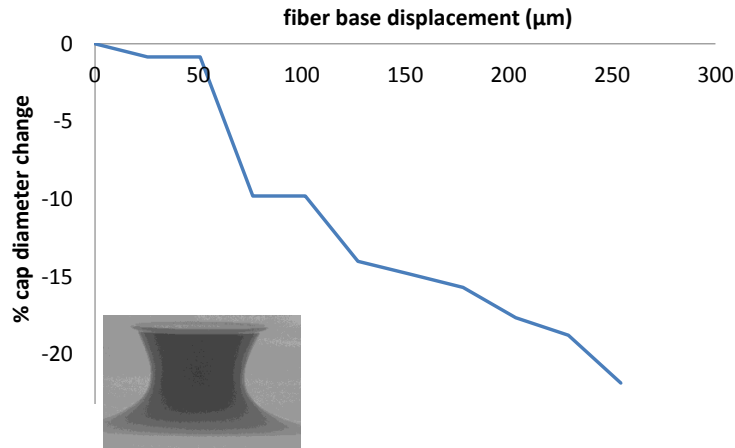


**Figure 5.30: Fiber cap shrinkage tests for Kraton G1657, 160  $\mu\text{m}$  diameter fiber on glass adhesion substrate.**

Cap shrinkage sometimes occurred in a non-stable behavior. Initially the fiber would be pinned until a threshold force was reached. The fiber cap edge then loses contact briefly at one point of the edge, this edge detachment continues in a spiral manner around the fiber perimeter. Once static friction was over come

around the perimeter, the whole cap shrinks steadily until adhesion was lost. Figure 5.31 a) shows the original cap, figure b) shows the shrunk fiber just prior to pull off, and figure c) shows the same fiber deformed unevenly while supporting a shear load.

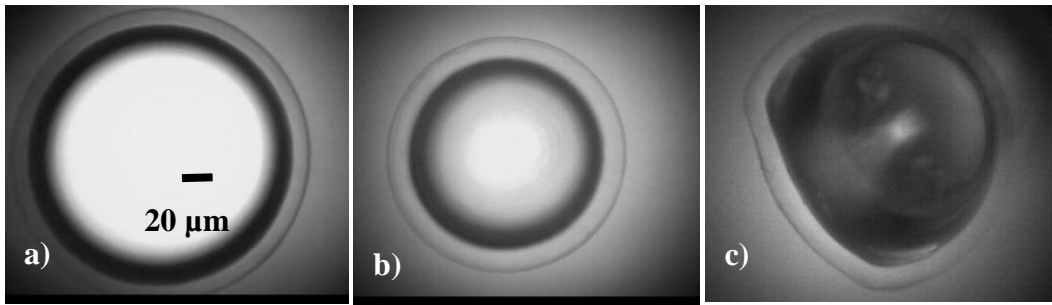


**Figure 5.31: Images a), b) and c) are of a 160 μm diameter Kraton G1657 fiber on glass with zero tensile load, maximum normal load, and maximum shear displacement before failure respectively.**

To implement the frictional boundary condition in the FEA model introduced in chapter 2, friction coefficients needed to be determined. Cap shrinkage was not an accurate measure for the friction forces as it provided very inconsistent results. As fibers were able to slide significantly on low friction surfaces (glass) during shear loading, a method was developed to extract friction information using shear loading.

The friction coefficient, modeled in equation 37 as:  $F_f = (F_{vdW} - F_{normal})\mu$ , was estimated using a combination of experimental results and the FEA simulation with a fixed boundary condition described in chapter 2. Shear slide experiments were performed in which the fiber was given

the maximum shear displacement it could withstand before adhesion loss and imaging the fiber during a relaxation stage to determine the distance it slides to reach an equilibrium. The shear forces created in the fiber with the total shear displacement of the base minus the shear slide distance of the cap represents the frictional force  $F_f$  which the substrate/fiber material can withstand. The van der Waals force was estimated as the maximum adhesion force which the fiber cap attained prior to detachment (for pure axial forces) while the normal force was measured by the load cell during the test (after shear slide occurred). From this, the friction coefficient was calculated using equation 37. As the frictional force,  $F_f$ , was determined using the FEA simulation, a comparison between axial forces for experimental and COMSOL fiber loaded in shear is given in Figure 5.32 to partially verify the accuracy of the model.

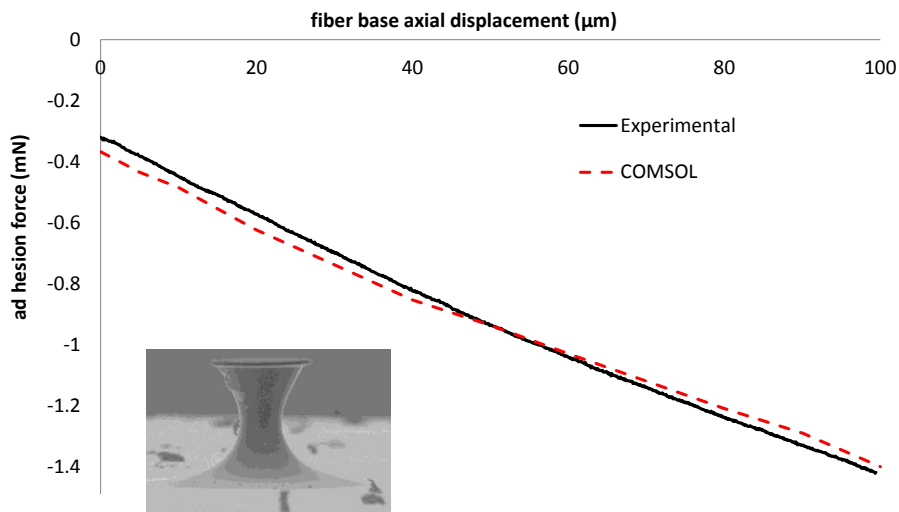


**Figure 5.32: Kraton G1657, 100 μm diameter fiber (experimental vs. FEA). Test consists of: preload with 1 mN pressure (~30 μm), shear 90 μm, followed by a pure normal elongation until loss of adhesion.**

Shear slide experiments were performed for Kraton G1657 and ST-1060 materials using the 100  $\mu\text{m}$  fiber. Figure 5.33 shows the cap slide for the Kraton fiber and the FEA simulation using a fixed cap boundary condition.

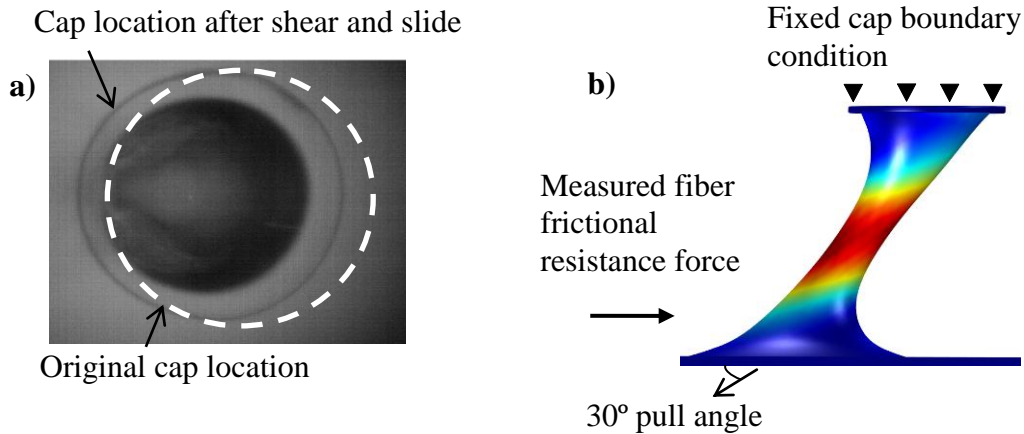


**Figure 5.33: Friction coefficient calculation: a) 100  $\mu\text{m}$  Kraton G1657 fiber: dotted line is first contact and image is the slide fiber after 150  $\mu\text{m}$  shear. b) FEA of fiber sheared 150  $\mu\text{m}$  and extended 86 $\mu\text{m}$  (30° pull angle).**

As higher friction coefficients seem to not affect normal adhesion but still provide stronger qualitative results, a simple 90° peel tests using an array of 100  $\mu\text{m}$  diameter fibers with 20  $\mu\text{m}$  spacing was performed. The adhesive was attached to a bull dog clip, held by a fish scale, and manually peeled at slow rate of approximately 250 mm/min (as defined in ASTM standard D1876-08: *Standard Test Method for Peel Resistance of Adhesives (T-Peel Test)* [99] while recording the fish scale force values. The test was performed for Kraton G1657, ST-1060 with all three adhesions substrates. Figure 5.34 shows the test method used for testing the Kraton fiber array on polystyrene.



**Figure 5.34: Fiber array peel test method using fish scale.**

Results for the slide distance tests, maximum normal adhesion, corresponding calculated friction coefficient, and array peel strength are summarized in Table 5-3. Peel test results demonstrate slightly improved adhesion with higher friction factors as expected.

**Table 5-3: Single fiber adhesion results, fiber array peel strength, and fitted friction factor (Kraton G1657 fiber sheared 150  $\mu\text{m}$ , ST-1060 sheared 90  $\mu\text{m}$  for these measurements).**

<i>Material</i>	<i>Factor</i>	<i>PS</i>	<i>Au</i>	<i>Glass</i>
Kraton G1657	<i>Normal Adhesion (MPa)</i>	1.4	1.25	1.0
	<i>Array peel (N/cm)</i>	0.29	0.25	0.16
	<i>Slide dist. (<math>\mu\text{m}</math>)</i>	0.5	0.3	14.0
	$\mu_f$	0.61	0.73	0.50
ST-1060	<i>Normal adhesion (MPa)</i>	2.3	1.75	2.05
	<i>Array peel (N/cm)</i>	0.31	0.29	0.22
	<i>Slide dist. (<math>\mu\text{m}</math>)</i>	~0.6	~0.8	3.0
	$\mu_f$	~0.62	~0.70	0.44

Calculation of these friction coefficients for gold and polystyrene was quite variable due to the almost negligible slide distance. While a coefficient is given, the fiber was very close to pinned and the actual value might be much higher. Because of the difficulty in attaining an estimate for the friction coefficient amount with high variability due to small fiber defects or pull off speed, it is recommended that in most cases, modeling friction does not justify the extra computational time required. Most cases encountered for these fibers (fast pull off speeds, higher friction adhesion substrates, and small interfacial defects) will be well simulated by the fixed boundary condition. Chapter 2 results show that quasi static situations where the load was applied and left for a long time can be modeled well with a roller boundary condition. High aspect ratio fibers (greater than 1:1 measured at the fiber undercut) also showed very little cap shrinkage. Only limited cases, as described in a flow chart in Figure 5.35, would require a frictional boundary condition.

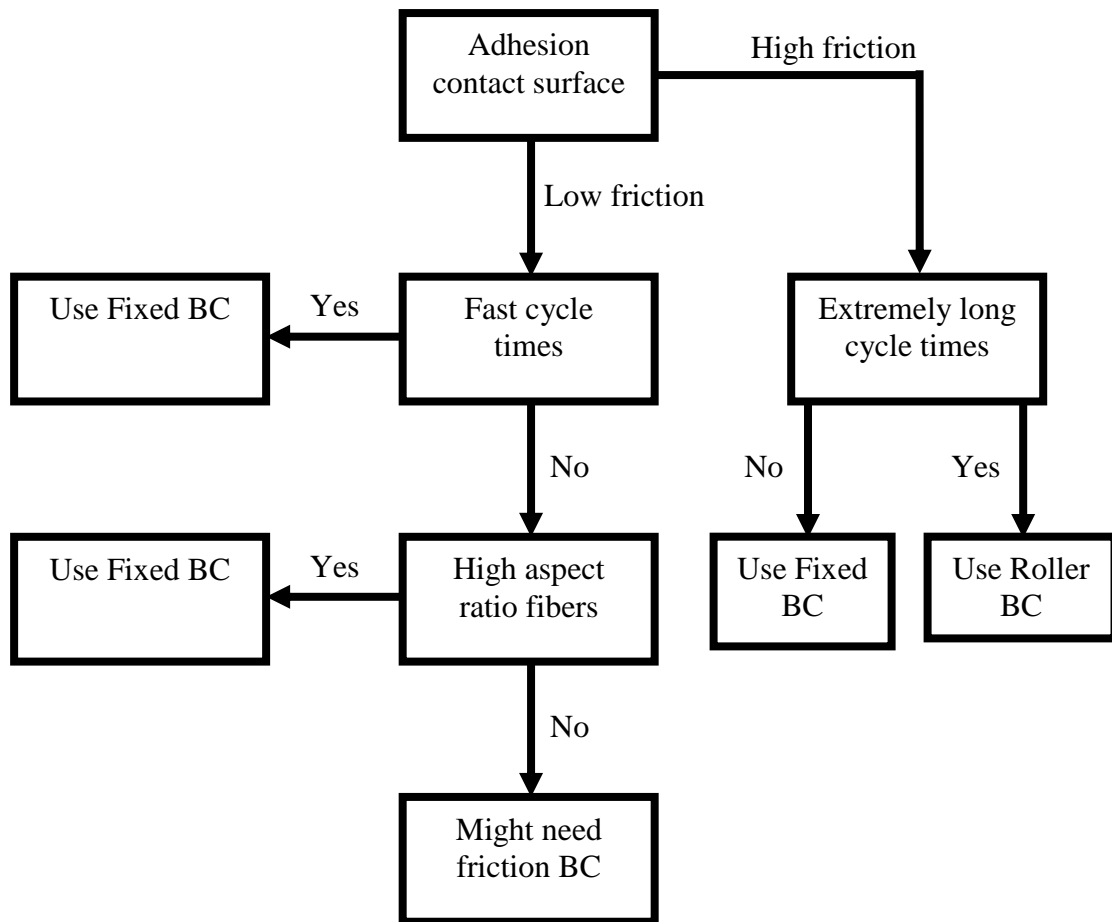


**Figure 5.35: Gecko adhesive top cap boundary selection flow chart.**

Single fiber adhesion tests confirmed that significant yield can occur in fibers after a single elongation. The FEA model developed in chapter 3 should be used in designing fiber geometries to limit the maximum strain in the fiber to values which will produce acceptable yield.

Future work should use the Instron equipment used in chapter 2 to repeat the peel tests to provide more correlation between single fiber shear tests and macro scale array peel tests. The single fiber test system could also be improved

by adding a second load cell in the x-axis to measure shear forces, which would allow more verification of the FEA model. By developing a biaxial bulk test system, improved Mooney Rivlin constants could be calculated and compared to modified constants in this chapter to determine if single fiber tests can be used to accurately find mechanical properties for future materials.

## 6 CONCLUSIONS

### 6.1 Summary

The goal of this project was to develop guidelines for designing and simulating gecko inspired dry adhesives. An improved simulation was developed by determining hyperelastic properties of polymers commonly used in dry adhesives. In addition to the non-linear behavior, the plasticity and viscoelastic of the bulk polymers was examined, demonstrating the implications of these properties on the durability and strength of dry adhesives. Gecko adhesive simulation capabilities were further improved by analyzing different boundary conditions for the fiber cap interface. The models developed were compared to experimental data by fabricating isolated single fibers tested on a custom built system. The modeling and material property data in this work are important for gecko adhesive commercialization efforts requiring designs which are durable, high strength, and low cost.

Significant challenges were overcome to attain data required for the full analysis of the single fiber designs. Examples of issues addressed were: uniaxial testing of bulk materials required extra processing of thermoplastic pellets using a hot glue gun, difficulty in making FEA models converge for the extremely high elongations of fibers, developing a frictional boundary condition at the fiber cap interface in the presence of a net tensile load, and manufacturing single fiber adhesives in a method which they could be attached to a testing probe without

contaminating the fiber. Overcoming these issues often resulted in an improved understanding of the phenomena and provided methods which can be used in future work to approach these problems.

Important findings were made in each section of this work which can provide useful guidelines for future adhesive design and simulation. From uniaxial bulk material testing, it was observed that all materials exhibit some degree of the Mullins effect (softening of the material for pre-strained elongations). This effect was also seen in single micro fiber tests, exemplifying that stress-strain material data recorded from pristine polymers may not be accurate for simulations after the adhesive has undergone one elongation cycle. Macro scale material tests also provided a function of the percent yield a material will undergo for a corresponding percent elongation. This information can be used in conjunction with the FEA simulation developed to determine appropriate fiber geometries which will result in a maximum strain within the fiber, causing an acceptable maximum yield for the design. The FEA simulation developed provides an excellent fit to bulk material data and viscoelasticity but underestimates the stiffness of the fiber slightly. This effect was likely due to either flow induced chain alignment of thermoplastic materials during molding into the micro cavities, or an incomplete hyperelastic Mooney Rivlin data fit due to only using the uniaxial bulk material tests. A modified Mooney Rivlin fit is also provided suggesting it might be possible to determine the material properties directly from the micro fibers. Future work could repeat bulk material tests with a

biaxial system to compare to these modified constants. Key simulation improvements were also made by examining three different fiber cap interface boundary conditions. Analysis of boundary conditions demonstrated that the axial force caused by normal elongations was identical for a fixed cap or roller cap simulation, but the resulting top cap stresses are greater if the cap was allowed to shrink. For the first time, a frictional boundary condition was also developed and implemented in COMSOL using friction coefficients estimated experimentally for several materials. Single fiber tests, however, demonstrated extremely variable results, mostly dominated by any interfacial defects (fiber cap surface or adhesion substrate). The results were also dependent of factors such as pull off speed, adhesion substrate material, and fiber aspect ratio. Due to the added complexity and computational time required for the frictional boundary condition, it was recommended that for most cases, a fixed or roller simulation will provide sufficiently accurate results.

When designing the geometry of a fiber using the fabrication process pioneered by our group, the proximity effect from DUV exposure should also be considered as it creates unexpected geometries such as square shaped necks on circular fibers. Fabricating fibers with different spacing determined that the critical distance for which fibers will have non-circular cross sections was approximately 20  $\mu\text{m}$  (for  $\sim 118 \mu\text{m}$  tall fibers in this work), independent of the fiber diameter and exposure dose.

The maximum recorded adhesion pressure for one “clean” fiber (very few defects) was 3.5 MPa. All mushroom shaped fibers observed during testing demonstrated a Mode 2 failure, with a void nucleation near the center of the fiber and rapid propagation throughout the cap once a critical pressure was reached. The adhesion of an array of fibers can be expected to be significantly lower as statistically a large number of fibers will have some defects reducing the total strength.

This work provides a useful foundation for future gecko adhesive modeling work. The Mooney Rivlin and Maxwell material model parameters presented can be directly implemented in commercially available FEA software. For materials not included in this thesis, the test and data fit method described can be replicated to obtain parameters. The simulation can be used for anisotropic adhesive design, requiring varying stress concentrations on the fiber cap, depending on peel direction. It can also be used to develop a full fiber adhesive array simulation to model the complex peeling phenomena.

## 6.2 Future Work

This thesis provides the framework for future simulation work in this field. The material parameters determined can be directly used and the COMSOL setup provides a basis for multiple boundary conditions and can easily be updated with different geometry fibers. Future work should:

- Use the bulk material experimental testing setup to characterize more polymers, especially shape memory polymers which could give controllable adhesion properties.
- Measure biaxial bulk material properties using by developing a custom pressurized membrane setup. These results could be compared to the modified Mooney Rivlin constants determined from single fibers. If these results match, material properties could be accurately extracted using only the single fiber test system.
- The finite element model developed could be used to study different fiber designs such as anisotropic adhesives and multi material fibers. The simulation could also be expanded to model multiple fibers and simulate the peeling phenomena.
- Different finite element packages could be used see if better convergence can be achieved with the frictional interface model. A custom finite element code may be required for this.
- The frictional interface of the single fibers should be further analyzed to determine why glass was the only substrate tested which gives a low friction surface. Single fiber friction could be tested using a Surface Force Apparatus (SFA) available in at the University of Alberta in Dr. Hongbo Zeng's lab. At the 2014 Adhesion conference, a world expert in friction from the Leibniz institute for New Materials in Germany (Dr. Roland Bennewitz) suggested

that the reduced friction on glass may be due to nanoscale roughness or cracks in the glass which initiate sliding. This should be further investigated by testing more surfaces and possibly measuring the glass surface roughness with AFM.

## 7 BIBLIOGRAPHY

- [1]Gottlieb Binder Fastener Systems Ltd. *Gecko-Nanoplast product description* 2011; Available at:Available at:  
<http://www.binderuk.com/en/products/gecko-r-nanoplast-r/>. Accessed 02/15/2014.
- [2]nanoGriptech, Inc. *Company Profile* 2009; Available  
at:<http://www.nanogriptech.com/about.html>. Accessed 02/15/2014.
- [3]Autumn K., M. Sitti, Y.A. Liang, A.M. Peattie, W.R. Hansen, S. Sponberg, T.W. Kenny, R. Fearing, J.N. Israelachvili and R.J. Full, Evidence for van der waals adhesion in gecko setae *Proceedings of the National Academy of Sciences* **99** 12252-12256. 2002.
- [4]Israelachvili J.N., *Intermolecular and surfaces forces*; revised third edition: Academic press; 2011: .
- [5]Arzt E., S. Gorb and R. Spolenak, From micro to nano contacts in biological attachment devices *Proceedings of the National Academy of Sciences* **100** 10603-10606. 2003.
- [6]Autumn K., A. Dittmore, D. Santos, M. Spenko and M. Cutkosky, Frictional adhesion: A new angle on gecko attachment *J Exp Biol* **209** 3569-3579. 2006.
- [7]Sameoto D. and C. Menon, Deep UV patterning of acrylic masters for molding biomimetic dry adhesives *J Micromech Microengineering* **20** 115037-10. 2010.
- [8]Kim S. and M. Sitti, Biologically inspired polymer microfibers with spatulate tips as repeatable fibrillar adhesives *Appl.Phys.Lett.* **89** 261911-1. 2006.
- [9]Menon,C., M. Murphy and M. Sitti, Gecko inspired surface climbing robots in *Proceedings - 2004 IEEE International Conference on Robotics and Biomimetics, IEEE ROBIO 2004, August 22, 2004 - August 26* 431-436, 2004.
- [10]Izadi H. and A. Penlidis, Polymeric bio-inspired dry adhesives: Van der waals or electrostatic interactions? *Macromolecular Reaction Engineering* **7** 588-608. 2013.
- [11]Aksak B., M.P. Murphy and M. Sitti, Adhesion of biologically inspired vertical and angled polymer microfiber arrays *Langmuir* **23** 3322-3332. 2007.

- [12]Murphy M. P., S. Kim and M. Sitti, Enhanced adhesion by gecko-inspired hierarchical fibrillar adhesives *ACS Applied Materials and Interfaces* **1** 849-855. 2009.
- [13]Spuskanyuk A. V., R.M. McMeeking, V.S. Deshpande and E. Arzt, The effect of shape on the adhesion of fibrillar surfaces *Acta Biomaterialia* **4** 1669-1676. 2008.
- [14]Henrey M., J.P. Diaz Tellez, K. Wormnes, L. Pambaguian and C. Menon, Towards the use of mushroom-capped dry adhesives in outer space: Effects of low pressure and temperature on adhesion strength *Aerospace Science and Technology* **29** 185-190. 2013.
- [15]Hoon E. J., Jin-Kwan Lee, N.K. Hong, H.M. Sang and K.Y. Suh, A nontransferring dry adhesive with hierarchical polymer nanohairs *Proc.Natl.Acad.Sci.U.S.A.* **106** 5639-44. 2009.
- [16]Wang Z., P. Gu and X. Wu, Gecko-inspired bidirectional double-sided adhesives *The Royal Society of Chemistry* DOI: **10.1039/C3SM52921E** 2014.
- [17]Autumn K., Properties, principles, and parameters of the gecko adhesive system *Biological Adhesives*225-256. 2006.
- [18]Heepe L., M. Varenberg, Y. Itovich and S.N. Gorb, Suction component in adhesion of mushroom-shaped microstructure *Journal of the Royal Society Interface* **8** 585-9. 2011.
- [19]Brendan James Ferguson. Improved Gecko Inspired Dry Adhesives Applied to the Packaging of MEMS MSc. Dissertation, University of Alberta 2013.
- [20]Kim S., A. Carlson, H. Cheng, S. Lee, J. Park, Y. Huang and J.A. Rogers, Enhanced adhesion with pedestal-shaped elastomeric stamps for transfer printing *Appl.Phys.Lett.* **100** 171909. 2012.
- [21]Hawkes,E.W., D.L. Christensen, E.V. Eason, M.A. Estrada, M. Heverly, E. Hilgemann, H. Jiang, M.T. Pope, A. Parness and M.R. Cutkosky, Dynamic surface grasping with directional adhesion in *2013 IEEE/RSJ International Conference on Intelligent Robots and Systems (IROS 2013)* 5487-93, 2013.
- [22]Bre L. P., Y. Zheng, A.P. Pego and W. Wang, Taking tissue adhesives to the future: From traditional synthetic to new biomimetic approaches *Biomaterials Science* **1** 239-253. 2013.

- [23]Kwak M. K., H. Jeong and K.Y. Suh, Rational design and enhanced biocompatibility of a dry adhesive medical skin patch *Adv Mater* **23** 3949-3953. 2011.
- [24]O. Rötting, W. Röpke, H. Becker and C. Gärtner, "Polymer microfabrication technologies," *Microsystem Technologies*, vol. 8, no. 1, pp. 32-36 2002.
- [25]Friend J. and L. Yeo, Fabrication of microfluidic devices using polydimethylsiloxane *Biomicrofluidics* **4** 026502-5. 2010.
- [26]Kim E., Y. Xia and G.M. Whitesides, Polymer microstructure formed by moulding in capillaries *Nature* **376** 581-584. 1995.
- [27]Xia Y. and G.M. Whitesides, Soft lithography *Angewandte Chemie International Edition* **37** 551-557. 1998.
- [28]Das S., S. Chary, J. Yu, J. Tamelier, K.L. Turner and J.N. Israelachvili, JKR theory for the stick-slip peeling and adhesion hysteresis of gecko mimetic patterned surfaces with a smooth glass surface *Langmuir* **29** 15006-15012. 2013.
- [29]Guo D., H. Zhang, J. Li, S. Fang, Z. Dai and W. Tan, Fabrication and adhesion of a bio-inspired microarray: Capillarity-induced casting using porous silicon mold *Journal of Materials Chemistry B* **1** 379-386. 2013.
- [30]Paretkar D. R., M.D. Bartlett, R. McMeeking, A.J. Crosby and E. Arzt, Buckling of an adhesive polymeric micropillar *J.Adhesion* **89** 140-158. 2013.
- [31]Murphy M. P., B. Aksak and M. Sitti, Adhesion and anisotropic friction enhancements of angled heterogeneous micro-fiber arrays with spherical and spatula tips *J.Adhes.Sci.Technol.* **21** 1281-96. 2007.
- [32]Krahn J. M., A.G. Pattantyus-Abraham and C. Menon, Polymeric electro-dry-adhesives for use on conducting surfaces *Institution of Mechanical Engineers* **0** 1-6. 2013.
- [33]Gillies A. G., J. Kwak and R.S. Fearing, Controllable particle adhesion with a magnetically actuated synthetic gecko adhesive *Advanced Functional Materials* **23** 3256-3261. 2013.
- [34]Borysiak M. D., E. Yuferova and J.D. Posner, Simple, low-cost styrene-ethylene/butylene-styrene microdevices for electrokinetic applications *Anal.Chem.* **85** 11700-11704. 2013.

- [35]Brassard D., L. Clime, K. Li, M. Geissler, C. Miville-Godin, E. Roy and T. Veres, 3D thermoplastic elastomer microfluidic devices for biological probe immobilization *Lab Chip* **11** 4099. 2011.
- [36]Didar T. F., K. Li, M. Tabrizian and T. Veres, High throughput multilayer microfluidic particle separation platform using embedded thermoplastic-based micropumping *Lab Chip* **13** 2615. 2013.
- [37]Roy E., M. Geissler, J. Galas and T. Veres, Prototyping of microfluidic systems using a commercial thermoplastic elastomer *Microfluid Nanofluid* **11** 235-244. 2011.
- [38]Heckele M. and W.K. Schomburg, Review on micro molding of thermoplastic polymers *J Micromech Microengineering* **14** R1-R14. 2004.
- [39]Schift,H., C. David, M. Gabriel, J. Gobrecht, L.J. Heyderman, W. Kaiser, S. Koppel and L. Scandelia, Nanoreplication in polymers using hot embossing and injection molding in *25th International Conference on Micro- and Nano-Engineering* 171-4, 2000.
- [40]Khaled W. and D. Sameoto, Manufacture of mushroom shaped dry adhesive fibers by thermo-compression molding of thermoplastic elastomers *Proc. Annu. Meeting of the Adhesion Society* 2014.
- [41]Castellanos G., E. Arzt and M. Kamperman, Effect of viscoelasticity on adhesion of bioinspired micropatterned epoxy surfaces *Langmuir* **27** 7752-7759. 2011.
- [42]Sauer R. A. and M. Holl, A detailed 3D finite element analysis of the peeling behaviour of a gecko spatula *Comput.Methods Biomech.Biomed.Engin.* **16** 577-591. 2013.
- [43]Carbone G., E. Pierro and S.N. Gorb, Origin of the superior adhesive performance of mushroom-shaped microstructured surfaces *Soft Matter* **7** 5545-5552. 2011.
- [44]Carbone G. and E. Pierro, Sticky bio-inspired micropillars: Finding the best shape *Small*n/a-n/a. 2012.
- [45]Long R., C. Hui, S. Kim and M. Sitti, Modeling the soft backing layer thickness effect on adhesion of elastic microfiber arrays *J.Appl.Phys.* **104** 044301. 2008.

- [46]Guidoni G. M., D. Schillo, U. Hangen, G. Castellanos and E. Arzt, Discrete contact mechanics of a fibrillar surface with backing layer interactions *J.Mech.Phys.Solids* **58** 1571. 2010.
- [47]Tang,M.M. and A.K. Soh, Simulation of a bio-adhesion system with viscoelasticity in *8th International Conference on Fracture and Strength of Solids 2010, FEOFS2010, June 7, 2010 - June 9* 780-784, 2011.
- [48]Huang R. C. and L. Anand, Non-linear mechanical behavior of the elastomer polydimethylsiloxane (PDMS) used in the manufacture of microfluidic devices *Innovations in Manufacturing Systems and Technology* 2005.
- [49]Zhou M., N. Pesika, H. Zeng, Y. Tian and J. Israelachvili, Recent advances in gecko adhesion and friction mechanisms and development of gecko-inspired dry adhesive surfaces *Friction* **1** 114-129. 2013.
- [50]Noderer W. L., L. Shen, S. Vajpayee, N.J. Glassmaker, A. Jagota and C.-. Hui, Enhanced adhesion and compliance of film-terminated fibrillar surfaces *Proceedings of the Royal Society A: Mathematical, Physical and Engineering Science* **463** 2631-2654. 2007.
- [51]Abusomwan U. and M. Sitti, Effect of retraction speed on adhesion of elastomer fibrillar structures *Appl.Phys.Lett.* **101** 211907 (4 pp.). 2012.
- [52]Heepe L., A.E. Kovalev, A.E. Filippov and S.N. Gorb, Adhesion failure at 180 000 frames per second: Direct observation of the detachment process of a mushroom-shaped adhesive *Phys.Rev.Lett.* **111** 2013.
- [53]Kroner E. and E. Arzt, Mechanistic analysis of force-displacement measurements on macroscopic single adhesive pillars *J.Mech.Phys.Solids* **61** 1295-304. 2013.
- [54]Kroner E. and E. Arzt, Single macropillars as model systems for tilt angle dependent adhesion measurements *Int J Adhes Adhes* **36** 32-38. 2012.
- [55]Bschaden B. and D. Sameoto, An alternative to PDMS: Mechanical properties of polyurethane and thermoplastic elastomers for microfabrication *Journal of Micromechanics and Microengineering* Submitted 2014.
- [56]Borysiak M. D., K.S. Bielawski, N.J. Sniadecki, C.F. Jenkel, B.D. Vogt and J.D. Posner, Simple replica micromolding of biocompatible styrenic elastomers *Lab Chip* **13** 2773. 2013.

- [57]ASTM International. ASTM D882-12 *Standard Test Method for Tensile Properties of Thin Plastic Sheeting* 2012; Available at:<http://enterprise1.astm.org/DOWNLOAD/D882.617045-1.pdf>. Accessed 06/11/2013.
- [58]Kraton Performance Polymers *Kraton G1657 Material Data Document* 2009; Available at:<http://docs.kraton.com/pdfDocuments/2009092514433985964815.PDF>. Accessed 01/28/2014.
- [59]BJB Enterprises Inc. *ST-1060 Polyurethane Elastomer Technical Data Sheet* 2013; Available at:<http://www.bjbenterprises.com/media/wysiwyg/pdfs/Shore-A-High-Performance/ST-1060.pdf>. Accessed: 06/02/2014.
- [60]BJB Enterprises Inc. *ST-1087 Polyurethane Elastomer Technical Data Sheet* 2011; Available at:[http://www.bjbenterprises.com/media/wysiwyg/pdfs/Shore-A-High-Performance/ST-1087\\_FR.pdf](http://www.bjbenterprises.com/media/wysiwyg/pdfs/Shore-A-High-Performance/ST-1087_FR.pdf). Accessed: 06/02/2014.
- [61]TOPAS Advanced Polymers *COC product overview* 2006; Available at:[http://www.topas.com/sites/default/files/files/topas\\_product-brochure\\_english.pdf](http://www.topas.com/sites/default/files/files/topas_product-brochure_english.pdf). Accessed 02/18/2014;.
- [62]Ogden R. W., G. Saccomandi and I. Sgura, Fitting hyperelastic models to experimental data *Comput.Mech.* **34** 484-502. 2004.
- [63]Yu Y. and Y. Zhao, Deformation of PDMS membrane and microcantilever by a water droplet: Comparison between mooney-rivlin and linear elastic constitutive models *J.Colloid Interface Sci.* **332** 467-476. 2009.
- [64]Ali A., M. Hosseini and B.B. Sahari, A review of constitutive models for rubber-like materials *Am. J. Eng. Applied Sci.* **3** 232-239. 2010.
- [65]Ibrahimbegovic A., *Nonlinear Solid Mechanics*: Springer; 2006.
- [66]Boyce M. C. and E.M. Arruda, Constitutive models of rubber elasticity: A review *Rubber Chemistry and Technology* **73** 504-523. 2000.
- [67]ASTM International. ASTM D7791-12 *Standard Test Method for Uniaxial Fatigue Properties of Plastics* 2012; Available at:<http://enterprise2.astm.org/DOWNLOAD/D7791.617045-1.pdf>. Accessed 06/11/2013.

- [68]Ciesielski A., Introduction to rubber technology *Rapra Technology Limited*125. 1999.
- [69]Diani J., B. Fayolle and P. Gilormini, A review on the mullins effect *European Polymer Journal* **45** 601-612. 2009.
- [70]Flügge W., Viscoelasticity: Springer-Verlag; 1975.
- [71]Ewoldt R. H., A.E. Hosoi and G.H. McKinley, New measures for characterizing nonlinear viscoelasticity in large amplitude oscillatory shear *J.Rheol.* **52** 1427-58. 2008.
- [72]Harley S. J., E.A. Glascoe and R.S. Maxwell, Thermodynamic study on dynamic water vapor sorption in sylgard-184 *The Journal of Physical Chemistry B* **116** 14183-14190. 2012.
- [73]Lin I., K. Ou, Y. Liao, Y. Liu, K. Chen and X. Zhang, Viscoelastic characterization and modeling of polymer transducers for biological applications *J Microelectromech Syst* **18** 1087-1099. 2009.
- [74]Mott P. H., J.R. Dorgan and C.M. Roland, The bulk modulus and poisson's ratio of “incompressible” materials *J.Sound Vibrat.* **312** 572-575. 2008.
- [75]ASTM International. ASTM D2990-09 . 2012*Standatd Test Method for Tensile, Compressive, and Fexural Creep and Creep-Rupture of Plastics* 2009; Available at:<http://enterprise2.astm.org/DOWNLOAD/D2990.617045-1.pdf>. Accessed 06/11/2013.
- [76]Ferguson,B., B. Bschaden, W.B. Khaled and D. Sameoto, Advances in Micromolding 3D Structures: New Materials, Methods, and Capabilities in *14th Hilton Head Solid-State Sensors, Actuators and Microsystems Workshop*, 2012.
- [77]Bschaden,B., B.J. Ferguson and D. Sameoto, Hyperelastic Simulation for Accurate Prediction of Gecko Inspired Dry Adhesive Deformed Shape and Stress Distripution Prior to Detachment in *36th Annual Meeting of the International Adhesion Society, Daytona Beach FL.*, 2013.
- [78]Khaled W. B. and D. Sameoto, Anisotropic dry adhesive via cap defects *Bioinspir Biomim.* **8** 2013.
- [79]Zaghloul,U., B. Bhushan, P. Pons, G. Papaioannou, F. Coccetti and R. Plana, Different stiction mechanisms in electrostatic MEMS devices: Nanoscale characterization based on adhesion and friction measurements in *Solid-State*

*Sensors, Actuators and Microsystems Conference (TRANSDUCERS), 2011  
16th International 2478-2481, 2011.*

- [80]Bschaden B., A. Baldelli, A. Amirfazli and D. Sameoto, Evaluation of polymer replication fidelity of micro surface topographies designed for superhydrophobicity *24th Canadian Congress of Applied Mechanics* 2013.
- [81]Sameoto D. and B. Ferguson, Robust large-area synthetic dry adhesives *J.Adhes.Sci.Technol.* 1-17. 2012.
- [82]Acrylic Sheet Education, Specs & Inspiration | Plaskolite. Available at:<http://www.plaskolite.com/>. Accessed: 02/17, 2014.;
- [83]MicroChem Corp. SU-8 Negative Epoxy Series Resists; Available at:[http://www.microchem.com/Prod-SU8\\_KMPR.htm](http://www.microchem.com/Prod-SU8_KMPR.htm). Assessed: 02/17/2014.
- [84]Hansen H. N., R.J. Hocken and G. Tosello, Replication of micro and nano surface geometries *CIRP Ann.Manuf.Technol.* **60** 695-714. 2011.
- [85]Desai S. P., D.M. Freeman and J. Voldman, Plastic masters - rigid templates for soft lithography *Lab on a Chip* **9** 1631-1637. 2009.
- [86]Dow Corning Corporation *Sylgard 184 Silicone Elastomer Product Information* 2013; Available at:<http://www.dowcorning.com/applications/search/default.aspx?r=131en>, Accessed: 02/06/2014.
- [87]BJB Enterprises Inc. *TC-5030 Translucent Silicone Rubber Technical Data Sheet* 2011; Available at:<http://www.bjbenterprises.com/media/wysiwyg/pdfs/Silicones/TC-5030.pdf>. Accessed: 06/02/2014.;
- [88]Kraton Performance Polymers *Kraton G1651 Material Data Document* 2007; Available at:[http://docs.kraton.com/tl\\_warehouse/pdf\\_data\\_docs/WG\\_2908\\_WGAD0.tmp.pdf](http://docs.kraton.com/tl_warehouse/pdf_data_docs/WG_2908_WGAD0.tmp.pdf). Accessed 01/28/2014.;
- [89]Kraton Performance Polymers *Kraton G1660 Material Data Document* 2009; Available at:<http://docs.kraton.com/pdfDocuments/2009081010402684362822.PDF>. Accessed 01/28/2014.;
- [90]Kutz M., *Handbook of Materials Selection*: John Wiley & Sons; 2002.

- [91]Professional Plastics, Tygon Medical/Surgical Tubing; Available at:<http://www.professionalplastics.com/professionalplastics/content/TygonS50HL.pdf>. Accessed 01/28/2014;.
- [92]Hongrun International Co. Ltd. Dryflex C3 6068 Material Properties; Available at:<http://plastics.ides.com/datasheet/e126098/dryflex-c3-6068>. Accessed 01/28/2014;.
- [93]Hongrun International Co. Ltd. Dryflex T509 Material Properties <br /><br />; Available at:<http://pp-resin.com/shop/supply/31847076.html>. Accessed 01/28/2014;.
- [94]Hongrun International Co. Ltd. Dryflex T909 Material Properties; Available at:<http://pp-resin.com/shop/supply/31850539.html>. Accessed 01/28/2014;.
- [95]Bschaden,B. and D. Sameoto, Frictional Interface Modeling for Gecko Inspired Dry Adhesives in *37th Annual Meeting of the International Adhesion Society, Inc. San Diego CA.*, 2014.
- [96]Nakatani A. I. and M.D. Dadmun, Flow-induced structure in polymers *ACS Symposium Series; American Chemical Society* **597** 1994.
- [97]Mackley M. R., Polymer processing: The physics of stretching chains *Phys. Technol.* **9** 13-19. 1978.
- [98]Meier P., M. Lang and S. Oberthur, Reiterated tension testing of silicone elastomer *Plastics, Rubber and Composites* **34** 372-377. 2005.
- [99]ASTM International. *ASTM D882-12 Standard Test Method for Peel Resistance of Adhesives (T-Peel Test)* 2008; Available at:<http://enterprise1.astm.org/DOWNLOAD/D1876.617045-1.pdf>. Accessed 06/11/2013.
- [100]Autumn K., Y.A. Liang, S.T. Hsieh, W. Zesch, P.C. Wai, T.W. Kenny, R. Fearing and R.J. Full, Adhesive force of a single gecko foot-hair *Nature* **405** 681-5. 2000.
- [101]Mohammad M. A., T. Fito, J. Chen, M. Aktary, M. Stepanova and S.K. Dew, Interdependence of optimum exposure dose regimes and the kinetics of resist dissolution for electron beam nanolithography of polymethylmethacrylate *Journal of Vacuum Science & Technology B (Microelectronics and Nanometer Structures)* **28** L1-L4. 2010.

- [102] Mohammad A.M., et al, Fundamentals of Electron Beam Exposure and Development: Springer; 2012.
- [103] MicroChem Corp. PMGI & LOR Lift-off Resists; Available at:[http://www.microchem.com/Prod-PMGI\\_LOR.htm](http://www.microchem.com/Prod-PMGI_LOR.htm). Assessed: 02/17/2014;.
- [104] MicroChem Corp. PMMA Positive Resists; Available at:<http://www.microchem.com/Prod-PMMA.htm>. Assessed: 02/17/2014;.

## 8 APPENDICES

### 8.1 Appendix A: Electron Beam Lithography Fabrication

Adhesion to rougher surfaces can be possible with smaller fibers, allowing more intimate contact with surface asperities, similar to the nanometer scale spatulae of a gecko foot pad [100]. Attempts were made in this work to fabricate nano-scale overhanging caps using electron beam lithography (EBL). This method proved to be extremely difficult to achieve with frequent tearing of polymer during de-molding, inconsistent fabrication results, and costly-time consuming exposure for any significant area fabrication. A summary of this work was given in the following.

Electron beam lithography exploits the significantly shorter waves in highly accelerated electrons as compared to UV or DUV waves in optical lithography. The shorter wavelengths allow smaller resolution patterning with features as small as 8 nm reported [101]. EBL operates similar to a SEM, with an electron gun generating electrons in a vacuum, accelerating the electrons to high voltages (5-30 kV), and focusing the electron beam by electric lenses. Unlike an SEM in which the sample to be imaged was moved allowing to image different areas, an EBL uses electrical deflections to control the beam and write patterns on a sample from computer generated files [102]. EBL resists, similar to optical lithography resists, can be positive or negative tone by either lowering the molecular weight through physicochemical changes or promoting cross-linking

reactions, increasing the molecular weight. The resist was then developed, creating positive or negative tone structures of the computer design mask layout.

This work used a bi-layer of two EBL resists, PMGI SF 9.5 and PMMA 495 A2 (MicroChem Corp.) to achieve an undercut structure. Silicon dies were prepared by piranha cleaning Test Grade silicon wafers, sputtering 50 nm of chrome followed by 50nm of gold as adhesion layers. Various combinations of PMMA/PMGI layers thickness were spun on the wafer according to supplier specifications [103,104]. PMMA was baked on a hotplate for 1 minute at 100 °C and for 2 minutes at 180°C to evaporate the solvent prior to spinning PMGI. A final bake was done for the PMGI for 1 minute at 100°C and 3 minutes at 180°C. The wafer was then manual cut into ~1 cm x 1 cm dies using a diamond scribe.

A computer designed pattern of circles and grids with ~100 nm to 4 μm features sizes was then exposed using a Raith 150-two electron beam system with a field emission electron source. While many combinations of exposure dose were attempted, a standard setup was; area dose: 600 μc/cm<sup>2</sup>, line dose: 800 pc/cm<sup>2</sup> and a dot exposure of 0.2 pc. Typically an accelerating voltage of 30 keV was used with a 10 μm aperture.

Following exposure, the dies were developed in a 1:3 mixture of MIBK:IPA (Methyl isobutyl ketone: Isopropyl alcohol) in a sonicator to improve development rates for 60 seconds. The die was then rinsed in IPA for 15 seconds to stop the PMGI development, followed by a 15 second DI water rinse and a N<sub>2</sub>

dry. The PMMA was then undercut with a 2 minute MF-319 developer and a 15 second DI water rinse. Figure 8.1 gives several images taken with an optical microscope after final development showing line and circular features fabricated.

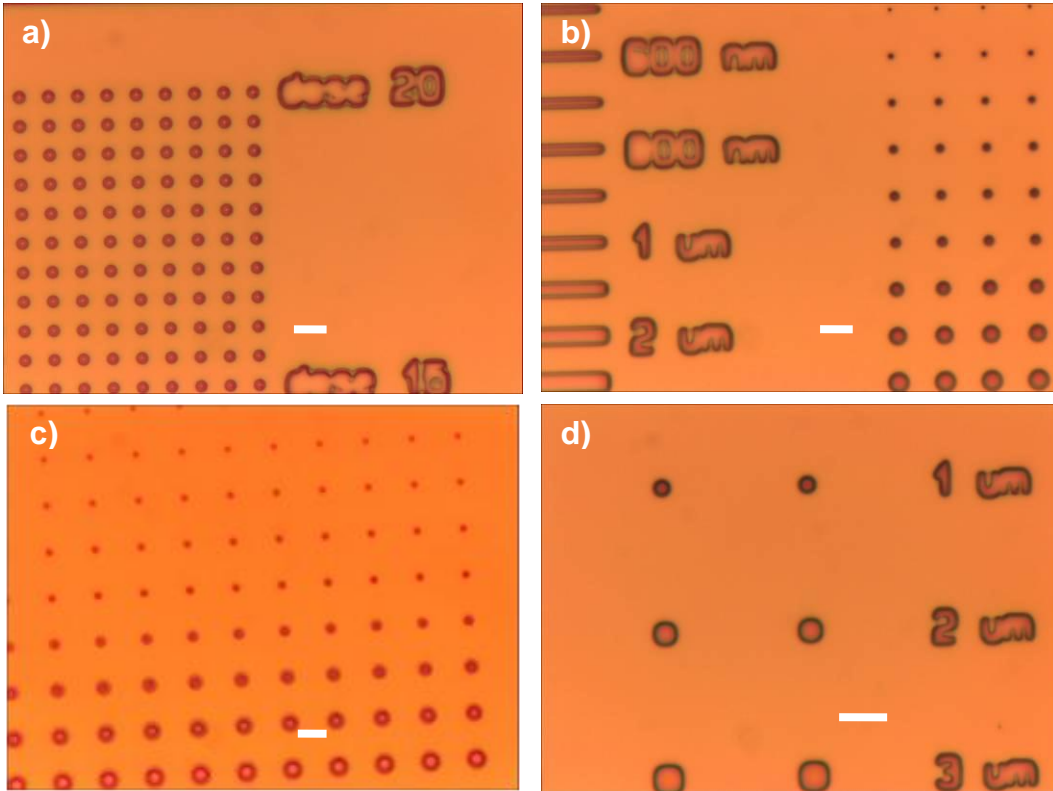


**Figure 8.1: Optical images of silicone die after EBL exposure and final development; a) 1  $\mu\text{m}$  diameter post array with dose variations showing over exposure or over development in the text, b) line and post array with sizes ranging from 600 nm to 2.5  $\mu\text{m}$ , c) post array with sizes ranging from 2  $\mu\text{m}$  to 500 nm with only largest features able to develop PMGI all the way through, d) 1, 2, and 3  $\mu\text{m}$  posts showing signs of some undercut from the dark perimeter of the circles. Scale bars represent 5  $\mu\text{m}$ .**

As the master mold fabricated with EBL was a negative version of the final desired feature, only one replication molding cast was required. PDMS was used for this process due to its low viscosity required to fill in the small features. PDMS was mixed in the recommended 10:1 part A with part B ratios, vacuum degassed for 45 minutes and cast onto the die. Only a single drop of prepolymer was required to cover the small features completely. The die was then vacuum degassed further for 20 minutes to fill in the cavities followed by a room temperature cure for 24 hours. The PDMS was then de-molded for optical microscope inspection as shown in Figure 8.2. In these images an overhang was clearly evident in the line features due to the bright blue areas. Post features in Figure 8.2 b) show fragments of torn of overhangs which did not survive the de-molding. This result demonstrates that an EBL bi-layer exposure can be used to create undercut features but a more durable polymer was needed to have sufficiently large overhangs survive.

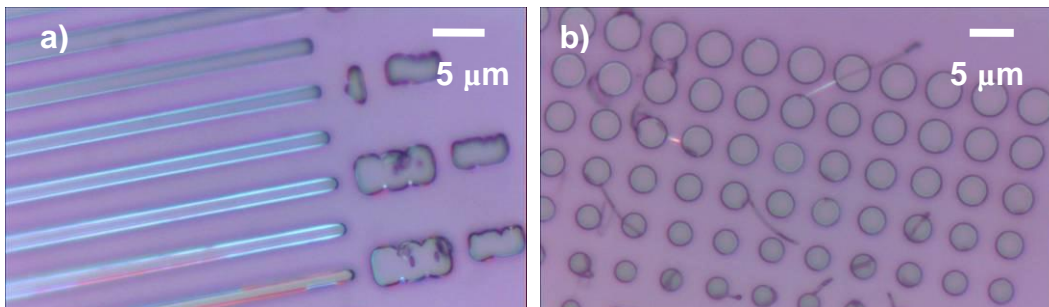


**Figure 8.2: Optical microscope images of PDMS cast from EBL patterned silicon die, a) line features with 400 nm – 1.5 μm widths, bright blue areas show overhanging cap, b) circular post features with 800 nm – 4 μm diameters. String like debris are torn off PDMS caps which did not survive de-molding.**

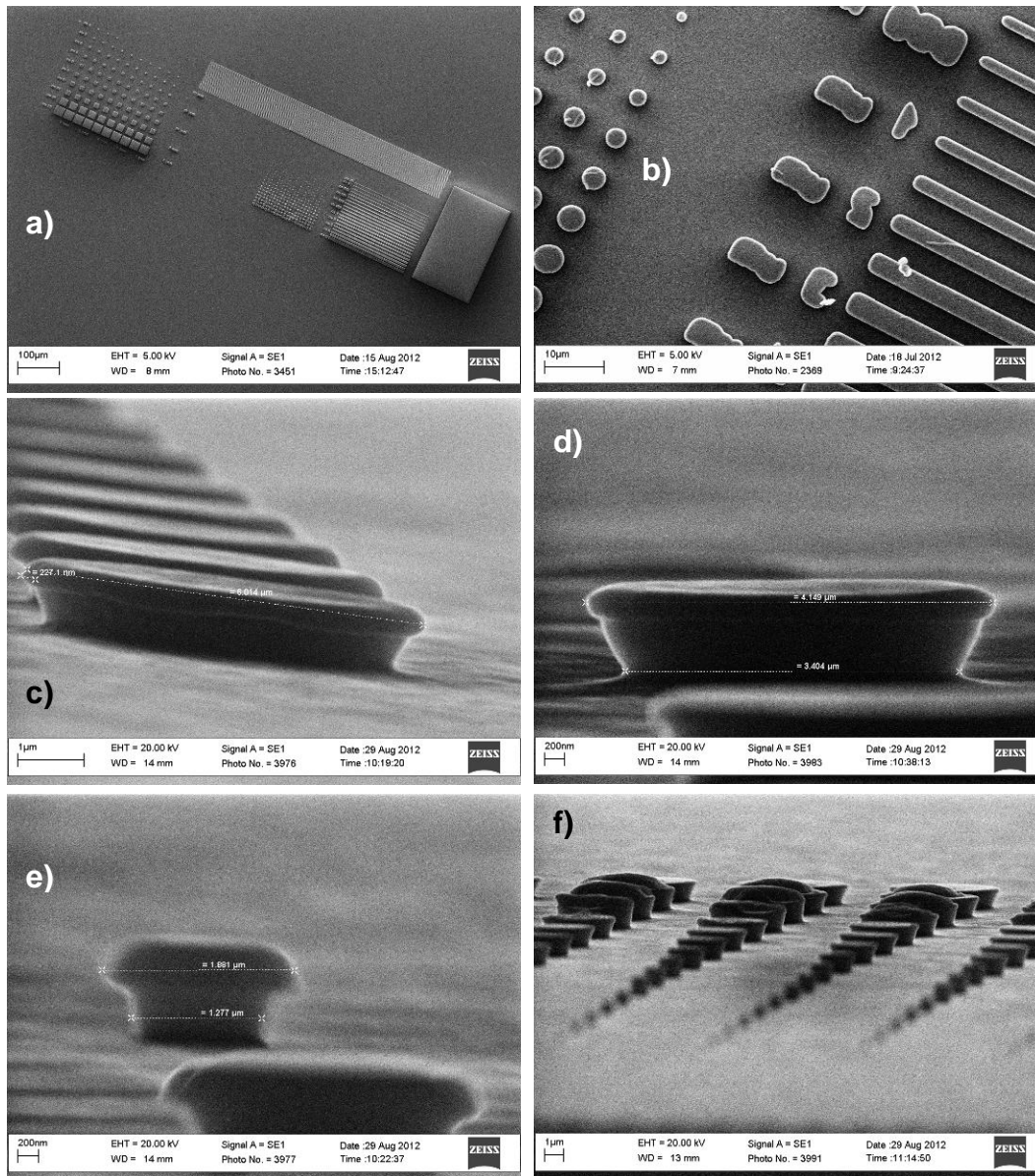


**Figure 8.3: SEM images of gold coated PDMS structures cast from EBL patterned die, a) full image of EBL mask, b) top view of 800 nm – 3 μm wide features showing bright perimeters where cap survived de-molding, c) 6 μm diameter fiber with slightly overhanging cap, d) 4 μm diameter fiber with overhang, e) 2 μm diameter fibers with rounded overhang, likely folded during gold deposition, f) array of various size fibers showing much shorter smaller features suggesting PMGI did not fully develop.**

While EBL fabrication might be incorporated for future designs with improved process parameters, it was not recommended based on work completed. Exposing an area of 1 cm x 1 cm would take over 10 hours requiring high clean room expenses. The method described using optical lithography was able to produce a wide range of fiber shapes and sizes. Several of these fibers were chosen, as shown in Figure 4.10, for adhesion testing described in the next chapter.

## 8.2 Appendix B: Matlab Code used for Non-Linear Data Fits

### Maxwell model Viscoelastic data fit

```
% Ben Bs Schaden
% University of Alberta
% Mechanical Engineering
% viscoelastic.m
% June 20, 2012
% Clear Variables
clc
close all
clear all

%%%%%%%%%%%%%%%%%%%%%%%%%%%%%%%%%%%%%%%%%%%%%%%%%%%%%%%%%%%%%%%%%%%%%%%%
% Import Experimental Data
path_original = mfilename('fullpath');
path_original = path_original(1:end-15);
path = uigetdir;
cd(path)
filename = 'Specimen_RawData_1.csv';

rng = [11 0 14 4];
M(:, :) = textread(filename, '%s', 'whitespace', ',', '');
modulus_check = M(2);
modulus_check = cell2mat(modulus_check);
modulus_check = modulus_check(2:end-1);
modulus_check = str2double(modulus_check);
if isnan(modulus_check) == 1;
    array_start_1 = 5;
else array_start_1 = 6;
end
zero_slope_check = M(21);
zero_slope_check = cell2mat(zero_slope_check);
zero_slope_check = str2num(zero_slope_check);
if size(zero_slope_check, 1) == 0
    array_start = 31;
else array_start = 32;
end
time_c = M(array_start:5:end);           % in seconds
ext_c = M(array_start+1:5:end);         % extension in mm
L_c = M(array_start+2:5:end);           % measured load in N
sigma_c = M(array_start+4:5:end);       % stress in MPa
t = M(array_start_1);                   % specimen thickness in mm
w = M(array_start_1+3);                 % specimen width in mm
gaugeL = M(array_start_1+6);            % gauge length in mm
gaugeL = cell2mat(gaugeL);
gaugeL = str2num(gaugeL(2:end-1));

cd(path_original)

s = size(ext_c, 1) - 1;
break_point = s;
```

```

for i = 1:s
ext_c(i) = ({ext_c{i}(2:end-1)});
ext(i) = str2num(ext_c{i});
time_c(i) = ({time_c{i}(2:end-1)});
time(i) = str2num(time_c{i});
L_c(i) = ({L_c{i}(2:end-1)});
L(i) = str2num(L_c{i});
sigma_c(i) = ({sigma_c{i}(2:end-1)});
sigma(i) = str2num(sigma_c{i});
end
ext = ext'; time = time'; L = L'; sigma = sigma';
%%% cut off extra data if sample broke %%%
for i = 1:s
    if time(i) > 30
        slope = (L(i) - L(i-1))/(time(i)-time(i-1));
        if slope < -20
            break_point = i-1;
            break
        end
    end
end
end

ext = ext(1:break_point); time = time(1:break_point); L =
L(1:break_point); sigma = sigma(1:break_point);

s = size(sigma,1);
[C,I] = max(sigma);
count=1;
sigma_save = sigma;
ext_save = ext;
time_save = time;
%%% find fit vlaues for viscoelasticity %%%
elastic_stress = sigma(end);
visco_stress = C-elastic_stress;
sigma = sigma - elastic_stress;
[aa,bb] = max(sigma);
sigma = sigma(bb:end);
time = time(bb:end);
start_experiment = time(1);
time = time - time(1); % subtract time to apply load
ext = ext(bb:end);
sigma = sigma*1e6;
ext = ext/1000;
% A starting guess value
%%%%%%%%%%%%%%%%%%%%%%%%%%%%%%%%%%%%%%%%%%%%%%%%%%%%%%%%%%%%%%%%%%%%%%%%
eo = max(ext);
fit0 = [0.1 1 10];
F2 = @(fit_val,time)F(fit_val,time,sigma);
[fit_val,resnorm2,~,exitflag,output2] =
lsqcurvefit(F2,fit0,time,sigma);
sigma_mw = F(fit_val,time,sigma);
A = zeros(length(time), length(fit_val));
for j = 1:length(fit_val)

```

```

    A(:,j) = exp(-1/fit_val(j)*time);
end
c = A\sigma;
E = c/(max(ext)/gaugeL*1000)/1000000;
E = E'
G = E/3*1000;
G = G'; % in Mpa
tau = fit_val % in seconds
Eo = elastic_stress/(max(ext)/gaugeL*1000)
sigma_mw = sigma_mw + elastic_stress*1000000;
time = time + start_experiment;
fig = figure(1);
set(fig, 'Position', [200,100,900,700])

plot(time_save,sigma_save,'b','LineWidth',2),hold on
plot(time,sigma_mw/1000000,'r--','LineWidth',2),hold on
t_1 = 'Model Fit';
%t_1 = strcat(['Model Fit (C1 = ',num2str(A1/1000),' kPa, C2 = ',num2str(A2/1000),' kPa)']);
h_leg= legend('Experimental Data',t_1,'Location','NorthEast');
set(h_leg,'box','off')
axis([0 150 elastic_stress-0.1 max(sigma_save)+0.05]);
xlabel('time (sec)','FontSize',35)
ylabel('tensile stress (MPa)','FontSize',35)
set(findall(fig,'type','text'),'FontSize',16,'fontWeight','normal')
set(gca,'LineWidth',1.5)
set(gca,'Xtick',0:15:150)
box off
cd(path)
% %%% Print files
% plotfile = 'Viscoelastic';
% print(fig,'-dpng','-r600',plotfile)

Function F:
function yEst = F(lam,xdata,ydata)

A = zeros(length(xdata), length(lam));
for j = 1:length(lam);
    A(:,j) = exp((-1/lam(j))*xdata);
end
c = A\ydata;
yEst = A*c;

```

### Mooney-Rivlin data fit

```
% Ben Bschaden
% University of Alberta
% Mechanical Engineering
% June 20, 2012

% Clear Variables
clc
close all
clear all

%%%%%%%%%%%%%%%%%%%%%%%%%%%%%%%%%%%%%%%%%%%%%%%%%%%%%%%%%%%%%%%%%%%%%%%%
% Import Experimental Data
driver_path = pwd;
path = uigetdir;
cd(path)
filename = 'Specimen_RawData_1.csv';
filename = 'MR1.csv';

M(:, :) = textread(filename, '%s', 'whitespace', ',', ',');
modulus_check = M(2);
modulus_check = cell2mat(modulus_check);
modulus_check = modulus_check(2:end-1);
modulus_check = str2double(modulus_check);
if size(modulus_check,1) == 0
    array_start_1 = 5;
else array_start_1 = 6;
end
zero_slope_check = M(21);
zero_slope_check = cell2mat(zero_slope_check);
zero_slope_check = str2num(zero_slope_check);
if size(zero_slope_check,1) == 0
    array_start = 31;
else array_start = 32;
end
time_c = M(array_start:5:end); % in seconds
ext_c = M(array_start+1:5:end); % extension in mm
L_c = M(array_start+2:5:end); % measured load in N
sigma_c = M(array_start+4:5:end); % stress in MPa
t = M(array_start_1); % specimen thickness in mm
w = M(array_start_1+3); % specimen width in mm
gaugeL = M(array_start_1+6); % gauge length in mm
gaugeL = cell2mat(gaugeL);
gaugeL = str2num(gaugeL(2:end-1));

s = size(ext_c,1)-1;
break_point = s;
for i = 1:s
    ext_c(i) = ({ext_c{i}(2:end-1)});
    ext(i) = str2num(ext_c{i});
    time_c(i) = ({time_c{i}(2:end-1)});
    time(i) = str2num(time_c{i});
    L_c(i) = ({L_c{i}(2:end-1)});
```

```

L(i) = str2num(L_c{i});
sigma_c(i) = ({sigma_c{i}(2:end-1)});
sigma(i) = str2num(sigma_c{i});
end
ext = ext'; time = time'; L = L'; sigma = sigma';

cd(driver_path)

%%% cut off extra data if sample broke %%%
if sigma(end) < 0.1
    for i = 0:s-2
        if sigma(end-i) > 0.1
            if abs((sigma(end-i)- sigma(end-i-1))) < 0.001
                break_point = s-i;
                break
            end
        end
    end
end
break_point = 1325;
ext = ext(1:break_point); time = time(1:break_point); L =
L(1:break_point); sigma = sigma(1:break_point);
s = break_point;

[pks,locs] = findpeaks(sigma);
count = 1;
for i = 1:size(pks,1)
    if pks(i) > 0.1
        peaks(count) = pks(i);
        peak_point(count) = locs(i);
        count = count+1;
    end
end
%%% Find Mooney-Rivlin Fit for final curve
MR_data_sigma = max(sigma,0);
MR_data_sigma(find(MR_data_sigma==0)) = [];
MR_data_ext = ext;
MR_data_ext = MR_data_ext(MR_data_ext(size(MR_data_ext)-
size(MR_data_sigma)+1:end));
MR_data_ext = MR_data_ext - min(MR_data_ext);
MR_data_ext = MR_data_ext/gaugeL;
MR_data_sigma = MR_data_sigma*1000000;

for i = 1:size(MR_data_ext,1)
    lambda(i) = 1+ MR_data_ext(i);
end
% A starting guess values
options = optimset('TolX',1e-8,'TolCon',1e-8,...
    'TolFun',1e-8,'MaxFunEvals',6000,'MaxIter',6000);
c_initial = 1000*rand(5);
c_initial = c_initial(1,:);
[C,resnorml,residual,exitflag]= lsqcurvefit(@(C,lambda)

```

```

MR_5(C,lambda),c_initial,lambda,MR_data_sigma,[],[],options);
exitflag
resnorml
yE = MR_5(C,lambda)
%%% Plot MR curve %%
fig = figure(1);
set(fig, 'Position', [200,100,900,700])

plot(MR_data_ext*100,MR_data_sigma/1000000, 'b', 'LineWidth', 2),hold
on
plot(MR_data_ext*100,yE/1000000, 'r--', 'LineWidth', 2),hold on
t_1 = 'Model Fit';
%t_1 = strcat(['Model Fit (C1 = ',num2str(A1/1000),' kPa, C2 =
',num2str(A2/1000), ' kPa)']);
h_leg= legend('Experimental Data',t_1,'Location','SouthEast');
set(h_leg, 'box', 'off')
xlabel('% elongation', 'FontSize', 16)
ylabel('tensile stress (MPa)', 'FontSize', 16)
set(findall(fig, 'type', 'text'), 'FontSize', 16, 'fontWeight', 'normal
')
set(gca, 'LineWidth', 1.5)
box off
%%% Print files
plotfile = 'MRbb';
print(fig, '-dpng', '-r600', plotfile)

```

## MR\_5 function

```

function yEst = Ogdon(C,lambda)

% Mooney Rivlin 5 term
yEst = ((2*C(1)*((lambda.^2) - (lambda.^-1)))...
+ (2*C(2)*(lambda - (lambda.^-2)))...
+ (4*C(3)*((lambda.^2) + (2*lambda.^-1) - 3) .* (lambda.^2 -
lambda.^-1))...
+ (4*C(4)*(2*(lambda) + (lambda.^-2) - 3) .* (lambda -
lambda.^-2))...
+ (2*C(5)*((2*lambda + lambda.^-2) - 3) .* (lambda.^2 -
lambda.^-1))...
+ ((lambda.^2 + 2*lambda.^-1 - 3) .* (lambda - lambda.^-
2)))) ./ lambda;
yEst = yEst';

```

### 8.3 Appendix C: COMSOL Simulation Reports

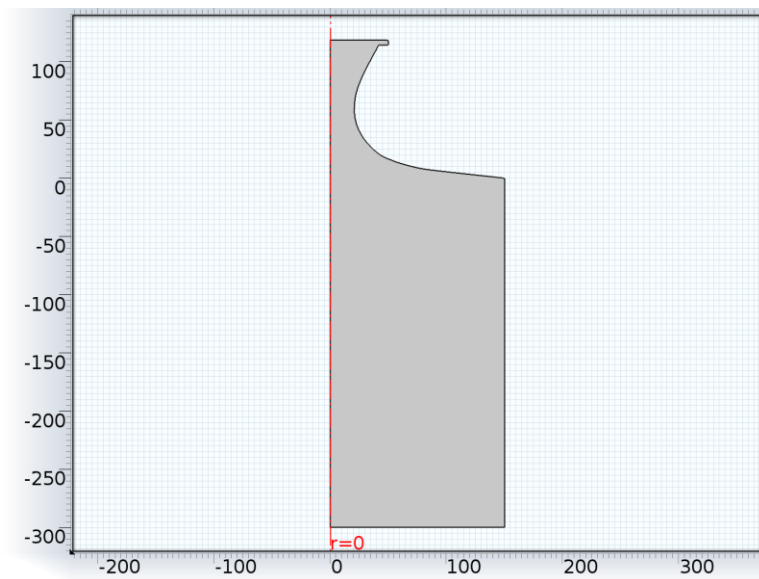
Normal Adhesion with Mooney Rivlin Hyperelastic Model.....	163-166
Viscoelastic Model with Maxwell Material.....	167-175
Frictional Boundary Condition Contact Model.....	176-182

## Normal Adhesion with Mooney Rivlin Hyperelastic Model

### Global Definitions: Parameters

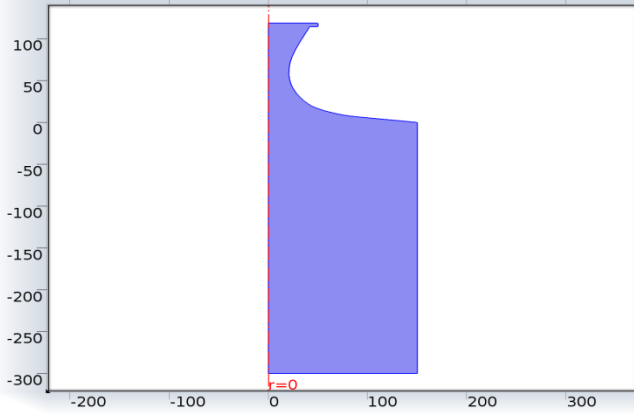
Name	Expression	Description
disp	10[um]	
k	1e10[Pa]	
M1	670000[Pa]	
M2	230000[Pa]	
M3	5500[Pa]	
M4	6000[Pa]	
M5	-15000[Pa]	

### Geometry 1



### Geometry 1

### Solid Mechanics (solid)

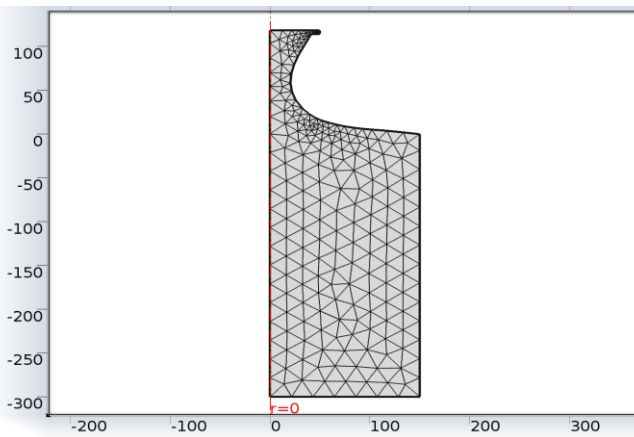


## Solid Mechanics

### Features

Linear Elastic Material 1
Axial Symmetry 1
Free 1
Initial Values 1
Hyperelastic Material 1
Fixed Constraint 1
Prescribed Displacement 1
Roller 1

### Mesh 1



### Study 1

Parametric Sweep: Parameter name: disp

Parameters: Stationary

### Study settings

Property	Value
Include geometric nonlinearity	On

### Physics selection

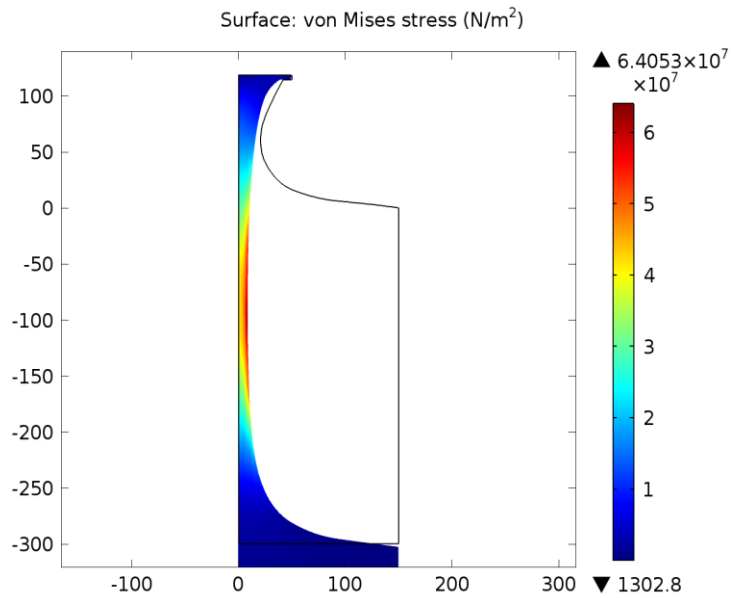
Physics	Discretization
Solid Mechanics (solid)	physics

### Derived Values : Line Integration 1

#### Expression

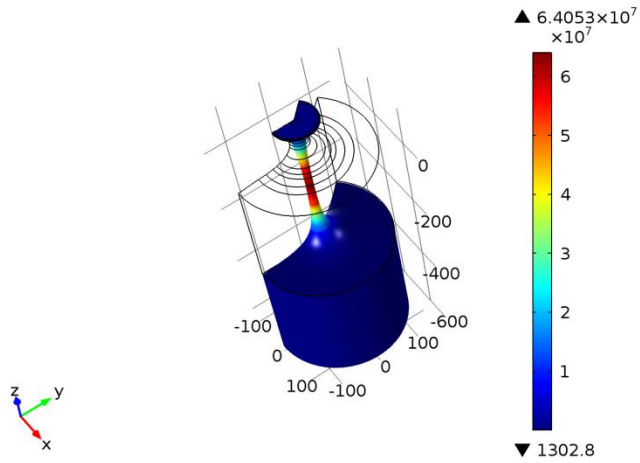
Name	Value
Expression	solid.RFz
Unit	N
Description	Reaction force, z component

### Plot Groups-Stress (solid)



### Surface: von Mises stress (N/m<sup>2</sup>)

Surface: von Mises stress (N/m<sup>2</sup>)



Surface: von Mises stress (N/m<sup>2</sup>)

# Viscoelastic Model with Maxwell Material

Global Definitions

Parameters 1

Parameters

Name	Expression	Description
disp	10[um]	
k	1e10[Pa]	
M1	630000[Pa]	
M2	250000[Pa]	
M3	0[Pa]	
M4	0[Pa]	
M5	0[Pa]	

Model 1 (mod1)

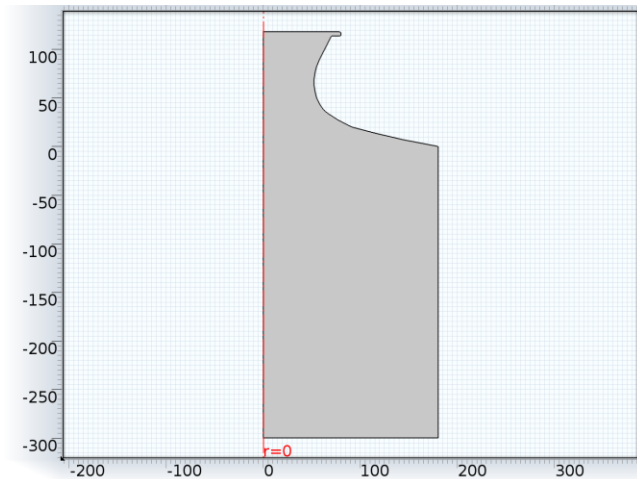
Definitions

Coordinate Systems

Boundary System 1

Coordinate system type	Boundary system
Identifier	sys1

Geometry 1



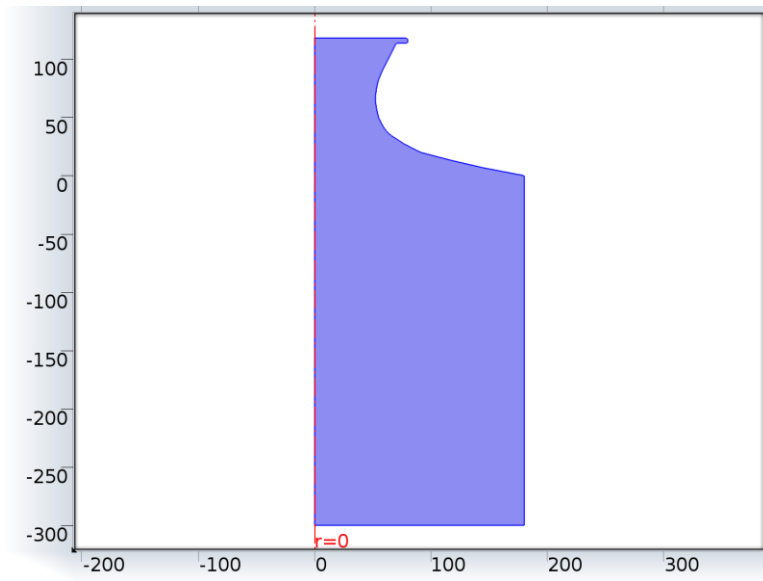
Geometry 1

## Units

Length unit	$\mu\text{m}$
Angular unit	deg

## Materials

### Material 1

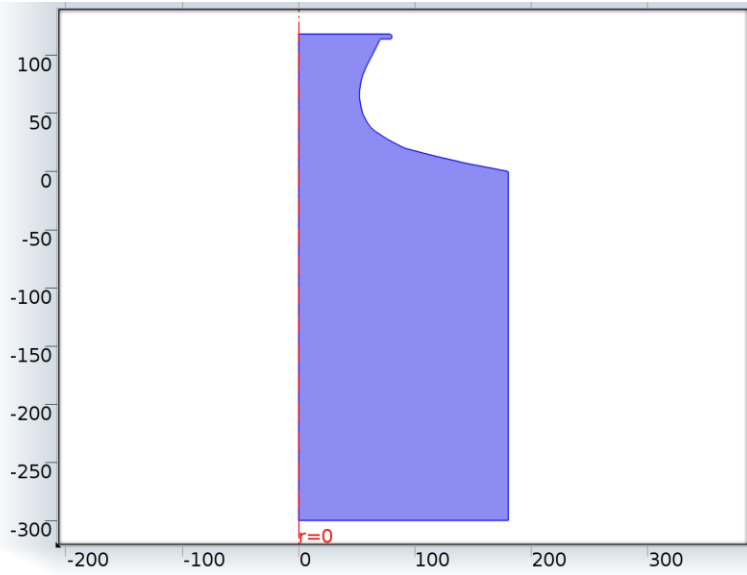


### Material 1

### Selection

Geometric entity level	Domain
Selection	Domain 1

### Solid Mechanics (solid)

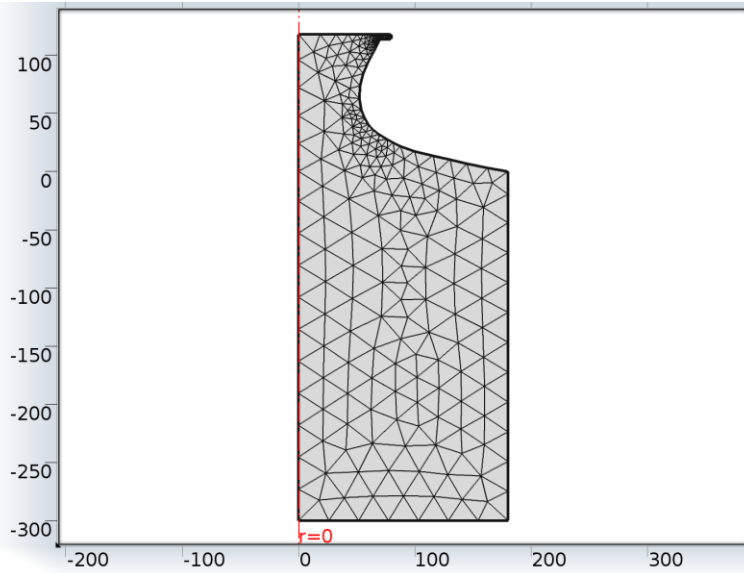


## Solid Mechanics

### Features

Linear Elastic Material 1
Axial Symmetry 1
Free 1
Initial Values 1
Hyperelastic Material 1
Fixed Constraint 1
Prescribed Displacement 1
Roller 1
Linear Viscoelastic Material 1

### Mesh 1



Mesh 1

Study 1

Parametric Sweep: Parameter name: disp

Parameters: Viscoelastic Transient Initialization

Study settings

Property	Value
Include geometric nonlinearity	On

Mesh selection

Geometry	Mesh
Geometry 1 (geom1)	mesh1

Physics selection

Physics	Discretization
Solid Mechanics (solid)	physics

Study 2

Time Dependent

Study settings

Property	Value
Include geometric nonlinearity	On

Times: range(0,1,150)

Mesh selection

Geometry	Mesh
Geometry 1 (geom1)	mesh1

Physics selection

Physics	Discretization
Solid Mechanics (solid)	physics

Results

Data Sets

Solution 1

Selection

Geometric entity level	Domain
Selection	Geometry geom1

Solution

Name	Value
Solution	Solver 1
Model	Save Point Geometry 1

Revolution 2D 1

Data

Name	Value
Data set	Solution 1

Revolution layers

Name	Value
Start angle	-90
Revolution angle	225

### Advanced

Name	Value
Define variables	On

### Settings

Name	Value
Space variables	{rev1x, rev1y, rev1z}

### Solution 2

#### Selection

Geometric entity level	Domain
Selection	Geometry geom1

#### Solution

Name	Value
Solution	Solver 2
Model	Save Point Geometry 1

### Revolution 2D 2

#### Data

Name	Value
Data set	Solution 2

### Revolution layers

Name	Value
Start angle	-90
Revolution angle	225

### Advanced

Name	Value
Define variables	On

### Settings

Name	Value
------	-------

Name	Value
Space variables	{rev2x, rev2y, rev2z}

Derived Values: Line Integration 1

Selection

Geometric entity level	Boundary
Selection	Boundary 2

Expression

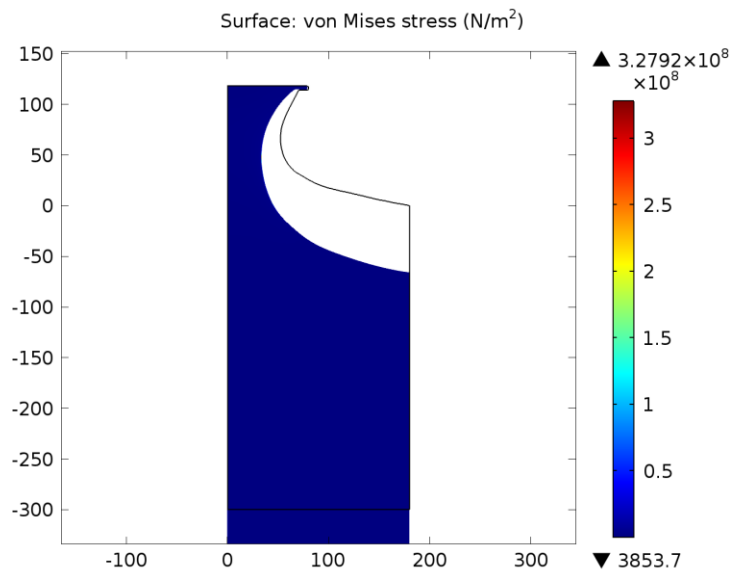
Name	Value
Expression	solid.RFz
Unit	N
Description	Reaction force, z component

Tables: Table 1

Line Integration 1 (solid.RFz)

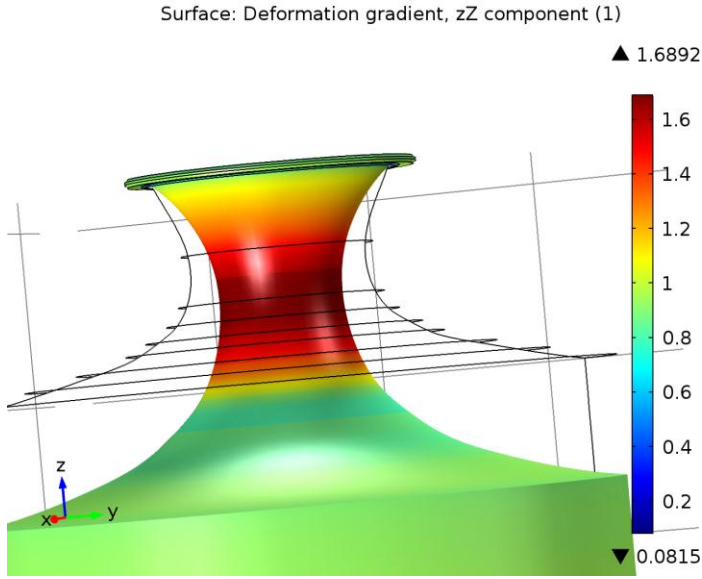
Plot Groups

Stress (solid)



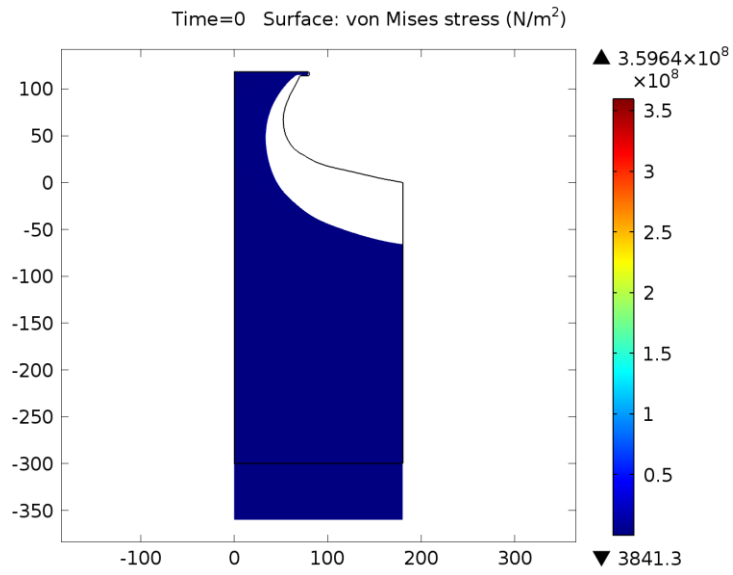
Surface: von Mises stress (N/m<sup>2</sup>)

Stress, 3D (solid)



Surface: Deformation gradient, zZ component (1)

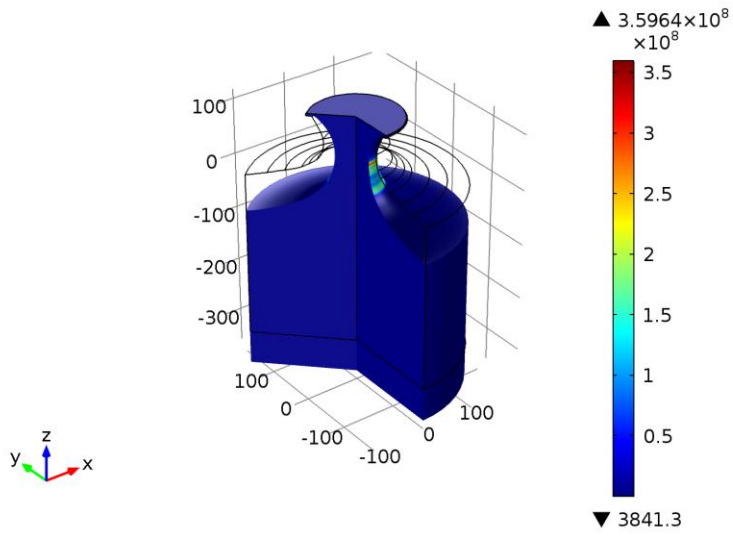
Stress (solid) 1



Time=0 Surface: von Mises stress (N/m<sup>2</sup>)

Stress, 3D (solid) 1

Time=0 Surface: von Mises stress (N/m<sup>2</sup>)



Time=0 Surface: von Mises stress (N/m<sup>2</sup>)

## Frictional Boundary Condition Contact Model

Global Definitions: Parameters 1

Parameters

Name	Expression	Description
k	1e10[Pa]	
K1	-69521[Pa]	
K2	532010[Pa]	
K3	3487.4[Pa]	
K4	58779[Pa]	
K5	-17524[Pa]	
S1	281620[Pa]	
S2	392650[Pa]	
T1	907810[Pa]	
T2	168850[Pa]	
disp	10[um]	

Model 1 (mod1)

Definitions: Variables

Variables 1

Selection

Geometric entity level	Entire model
------------------------	--------------

Name	Expression	Description
mu	8	
vdWforce	100000[Pa]	

Pairs

Contact Pair 1

Pair type	Identity pair
Pair name	ap1

Coordinate Systems: Boundary System 1

Coordinate system type	Boundary system
Identifier	sys1

Geometry 1



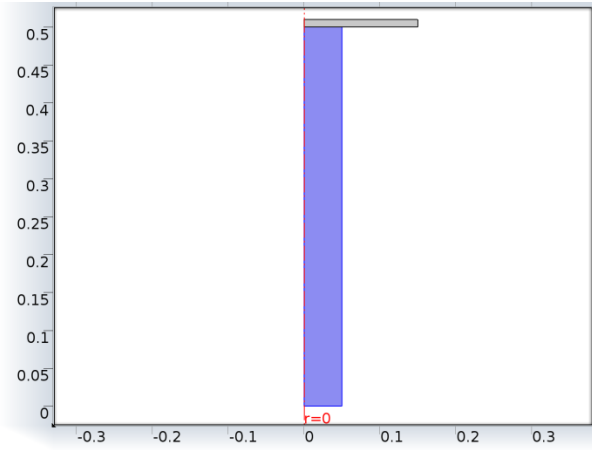
Geometry 1

Units

Length unit	mm
Angular unit	deg

Materials

Material 1

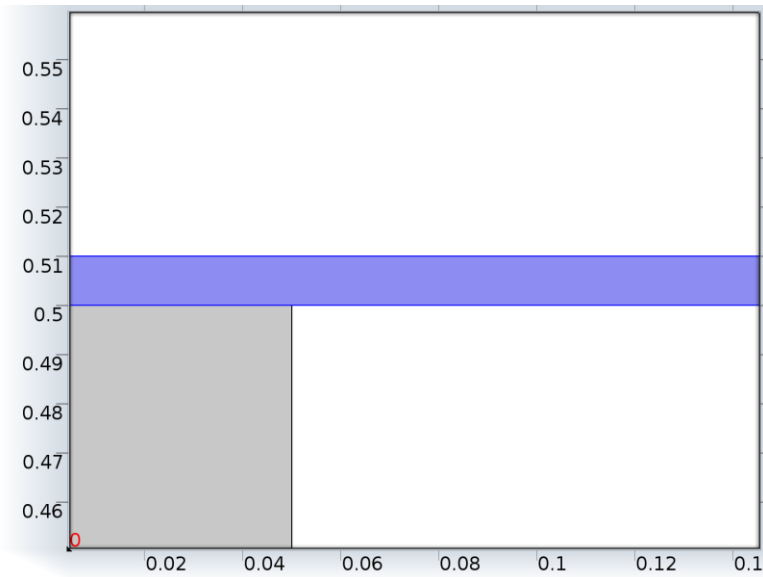


Material 1

Selection

Geometric entity level	Domain
Selection	Domain 1

Material 2

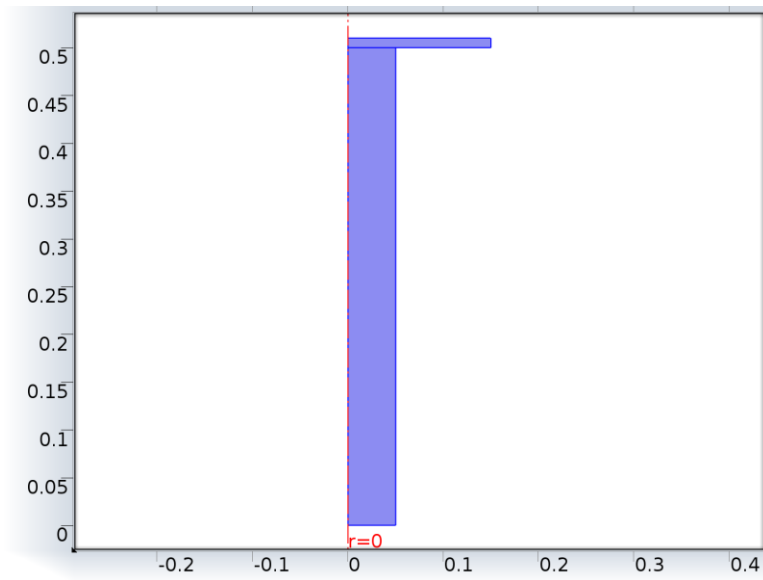


Material 2

Selection

Geometric entity level	Domain
Selection	Domain 2

## Solid Mechanics (solid)

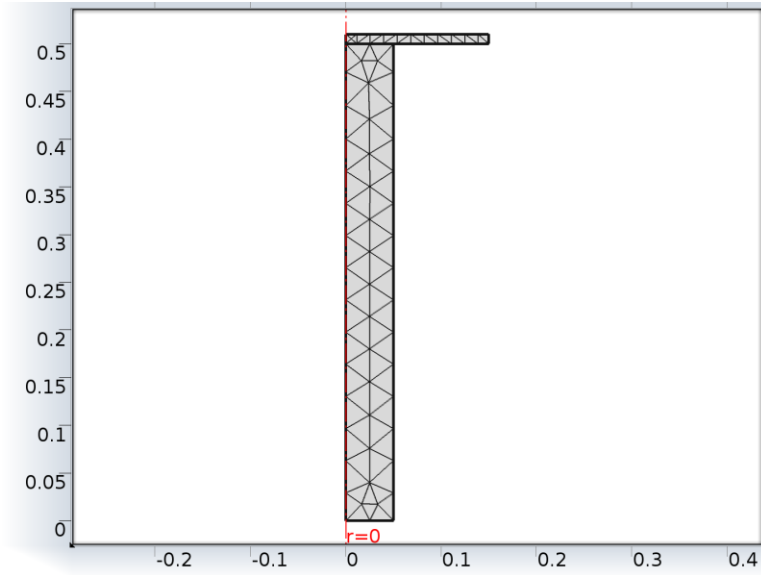


## Solid Mechanics

### Features

Linear Elastic Material 1
Axial Symmetry 1
Free 1
Initial Values 1
Hyperelastic Material 1
Fixed Constraint 1
Contact 1
Prescribed Displacement 1
Roller 1

### Mesh 1



Mesh 1

Study 1: Stationary

Study settings

Property	Value
Include geometric nonlinearity	On

Mesh selection

Geometry	Mesh
Geometry 1 (geom1)	mesh1

Physics selection

Physics	Discretization
Solid Mechanics (solid)	physics

Results

Data Sets:Solution 1

Selection

Geometric entity level	Domain
Selection	Geometry geom1

### Solution

Name	Value
Solution	Solver 1
Model	Save Point Geometry 1

### Revolution 2D 1

#### Data

Name	Value
Data set	Solution 1

#### Revolution layers

Name	Value
Start angle	-90
Revolution angle	225

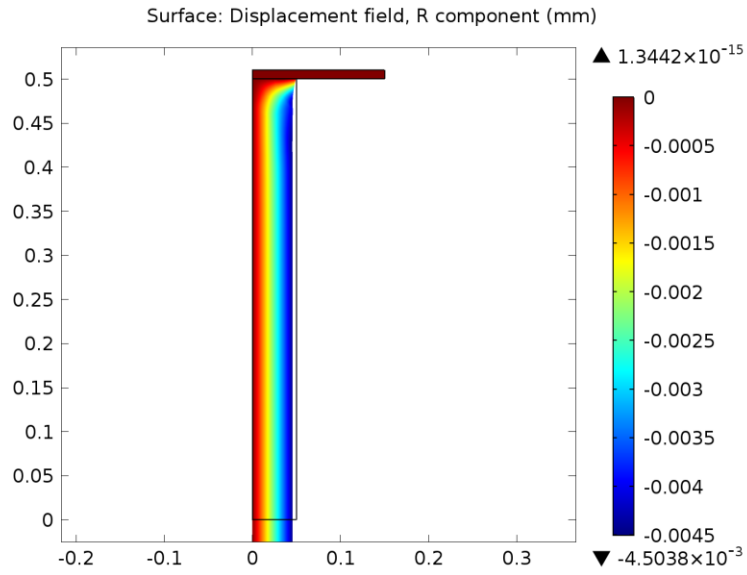
#### Advanced

Name	Value
Define variables	On

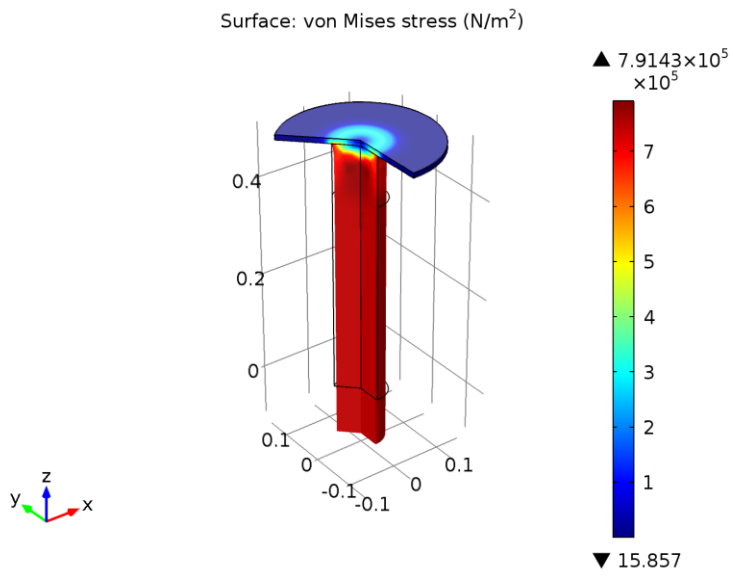
#### Settings

Name	Value
Space variables	{rev1x, rev1y, rev1z}

#### Plot Groups: Stress (solid)

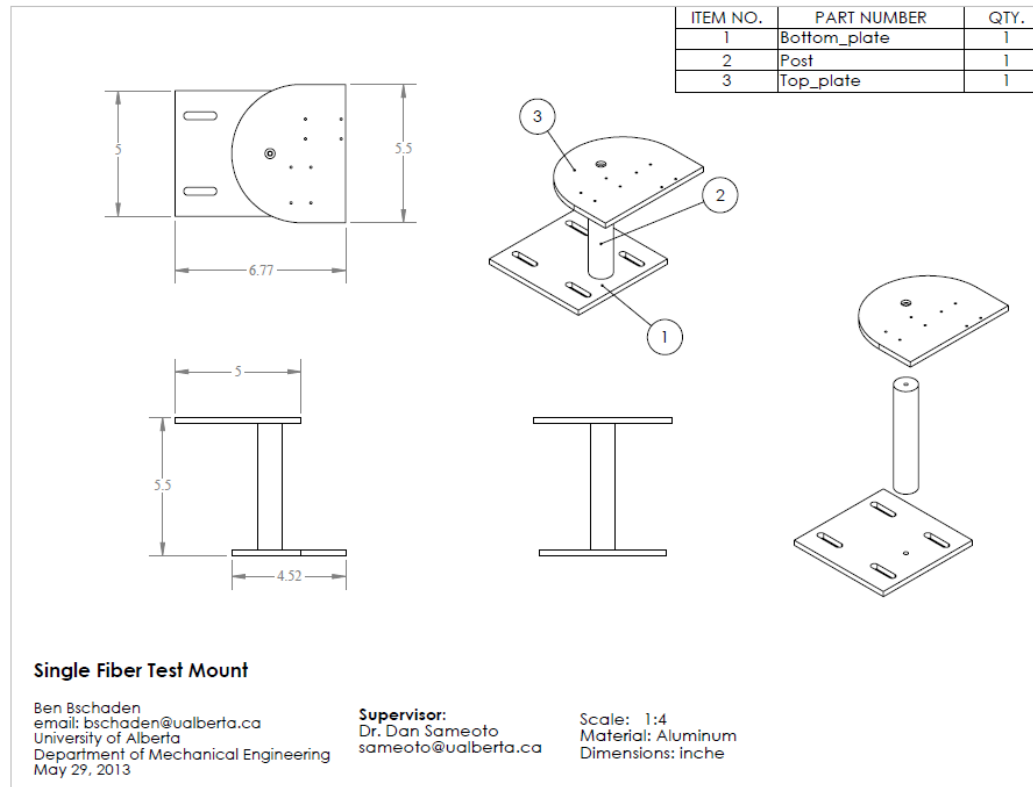


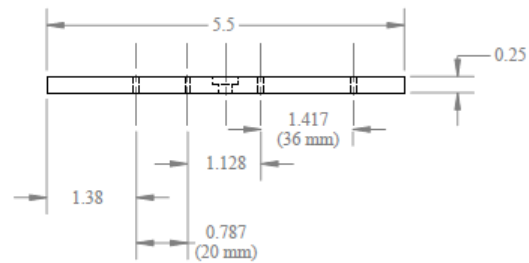
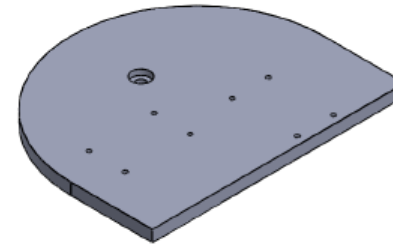
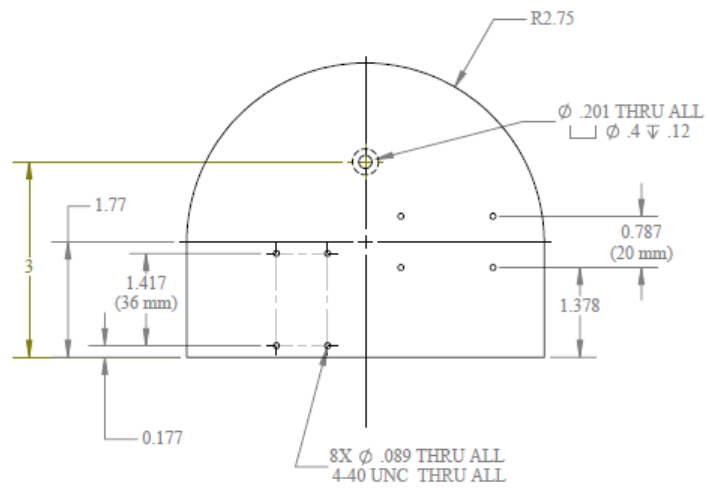
Surface: Displacement field, R component (mm): Stress, 3D (solid)



Surface: von Mises stress (N/m<sup>2</sup>)

## 8.4 Appendix D: Single Fiber Test Mount Bracket Drawing Package



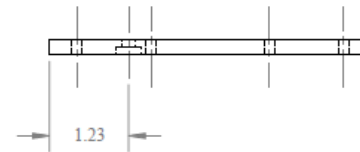
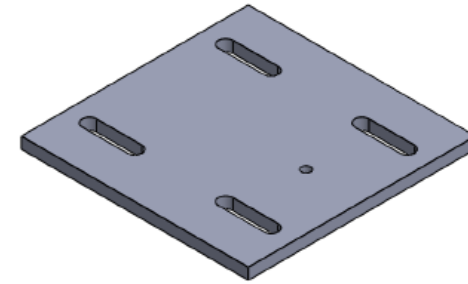
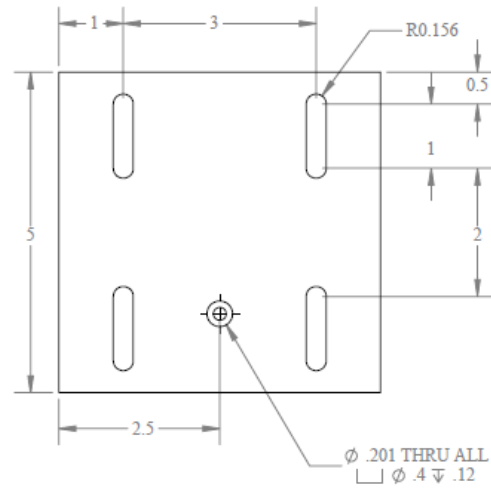


### Top Plate

Ben Bschaten  
 email: bschaten@ualberta.ca  
 University of Alberta  
 Department of Mechanical Engineering  
 May 29, 2013

**Supervisor:**  
 Dr. Dan Sameoto  
 sameoto@ualberta.ca

Scale: 1:2  
 Material: 1/4" Aluminum  
 Dimensions: inch

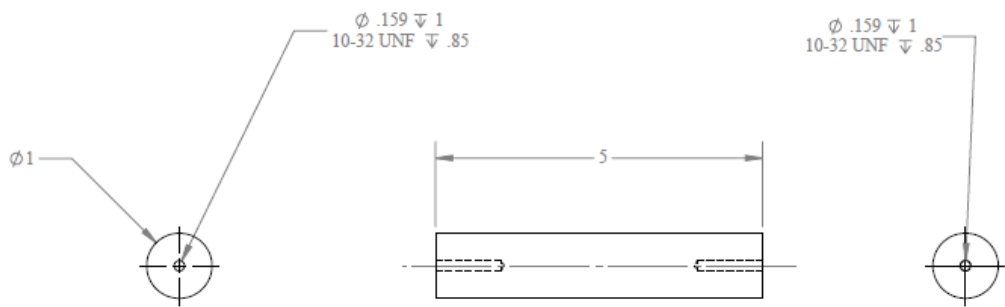


### Bottom Plate

Ben Bschaden  
 email: bschaden@ualberta.ca  
 University of Alberta  
 Department of Mechanical Engineering  
 May 29, 2013

**Supervisor:**  
 Dr. Dan Sameoto  
 sameoto@ualberta.ca

Scale: 1:2  
 Material: 1/4" Aluminum  
 Dimensions: inch



**Post**

Ben Bscharn  
 email: bschaden@ualberta.ca  
 University of Alberta  
 Department of Mechanical Engineering  
 May 28, 2013

**Supervisor:**  
 Dr. Dan Sameoto  
 sameoto@ualberta.ca

Scale: 1:2  
 Material: 1" Dia. Aluminum  
 Dimensions: inch